Department of Environment Systems
Graduate School of Frontier Science
The University of Tokyo

2018

Master's Thesis

Supercritical Water Gasification of Vegetable Oil Using Nickel Catalyst

「ニッケル触媒を用いた植物油の超臨界水ガス化に関する研究」

Submitted February 20, 2019

Adviser: Associate Professor Teppei Nunoura
Co-adviser: Associate Professor Shigeru Tabeta

ダイアン　バレンズエラ　グバタンガ
Diane Valenzuela Gubatanga

AKNOWLEDGMENTS

It is my pleasure to acknowledge the roles of the following individuals who had made a significant impact on my growth as a researcher and who, in one way or another had helped me accomplish this Master thesis.

First, to my research supervisor, Professor Teppei Nunoura, for patiently guiding me as I explore the SCWG topic deeper, for giving me useful advices when I am faced with bigger problems and for always reminding not just me, but everyone else in the lab, that while getting good lab results is good, making mistakes and learning from them is better. He's an admirable example to everybody and serves as an embodiment of what a truly dedicated and honest researcher is supposed to be and because of this, I aspire to be like him in the future.

Next, I would like to give my sincere gratitude to our lab's Assistant Professor, Dr. Osamu Sawai for sharing his invaluable knowledge and years as an experienced researcher in the field of catalysis. Many times, I would find myself trapped in a box, but he will always find me with generous hints, and mostly tons of constructive criticisms. This trained me to think independently and find ways on how to solve a problem in the most 'scientific' and 'professional' way; the way a Sawai-sensei would handle it.

I would also like to extend my deepest thanks to all the professors and academic researchers who, in one way or another, helped me in the completion of this research. To Professor Shigeru Tabeta, my research co-adviser, for his invaluable insights and opinions shared during consultation times. Thank you very much for letting me see my research in a whole new perspective. Your advices gave me the opportunity to improve my research discussion. To Assistant Professor Makoto Akizuki, for generously lending us the TOC analyzer in Oshima Lab. To the people in Otomo lab, mainly to Professor Junichiro Otomo for allowing me to use the NovaWin Gas sorption system, to Dr. Fumihiko Kosaka for teaching me how to do the BET analysis and to Dr. Martin Keller for supervising me during the analysis.

Next, to my family, especially my parents, Mr. and Mrs. Romeo P. Gubatanga, thank you for being my rock and foundation when things get too shaky, for cheering me on as I reach for my goal and for always reminding me that wherever I go and no matter what I do, I always make you proud. To my Filipino friends here in Japan, thank you for making me feel closer to home. To Ms. Ruth Anne Gonocruz and Mr. Caidric Gupit, I thank God for

letting me meet such true and honest friends. They were there through my ups and downs, and I couldn't imagine surviving these past years without their support and encouragement.

To my laboratory colleagues, especially Mr. Takuya Ogawa and Mr. Zhou Yiming who are also M2 students in Nunoura Lab thanks for all the lessons and research techniques you've shared with me. To my senpai, Ms. Haruna Hirai, who have taught me so much especially during my Research and M1 student days, many thanks. Much of what you have taught me has been applied in my current research and I couldn't thank you enough for being a good senpai. Also, to my senpais, Ms. Disni Sanjeewani Gamlath, whose smile is as bright as a sunshine, clearly, you've made my days brighter and cheerier. To Mr. Retsu Miyoshi and Mr. Yuuki Iida, for setting as a good example when doing research, my sincere gratitude goes to you. My heartfelt thanks also goes to Ms. Jennifer Chia, for being not just a research colleague, but also as a close friend who's sharing so many life passions with me, I'm looking forward to more fruitful lab days together. To my kouhais, Ms. Xiaoyun Zhou, Mr. Tsuyoshi Kayamura, Mr. Shiming Qin, and Ms. Jiongmei Yang, I wish you good luck as you embark to the same journey ahead!

And above all, to the Almighty God, I lift up everything to Him.

To God be the Glory!

DIANE VALENZUELA GUBATANGA

ABSTRACT

The research of supercritical water gasification of vegetable oil using nickel catalyst has been carried out using a lab-scale, flow type reactor with operating conditions kept constant at 400 °C and 25 MPa. First, it aims to study the applicability of SCWG in vegetable oil treatment. Second, it aims to observe the behavior of nickel catalyst during supercritical water gasification of vegetable oil. The first part of the study was carried out by evaluating the effect of biomass concentration using four (4) different oil concentrations, herein denoted as SCWG 0.02, SCWG 0.03, SCWG 0.04, and SCWG 0.05, representing 2%, 3%, 4% and 5% oil concentration in water respectively. The efficiency of the process was evaluated according to gas yields and efficiencies. During the initial phase of the reaction, high gas yields and efficiencies could be observed; followed by a steep decline in both gas yields and efficiencies. This trend is observed in all experimental case. This proves that the catalytic behavior can be observed with the system's ability to convert the biomass into desired gaseous products. High H_2 production was observed at all experiments suggesting that SCWG could be a viable method to treat vegetable oil. The unspent catalyst was characterized using gas sorption techniques and it was found out to have a surface area of 58.2 m^2/g. However, after the gasification experiments conducted for 300 minutes, this surface area value decreased by 4 – 6 times. This suggests the loss of active surface area which may have caused the catalyst' decline in activity. Further observation of the nickel catalyst behavior in SCWG of oil led to an assumption that the loss of catalytic activity may have been caused by carbon deposition and surface sintering.

TABLE OF CONTENTS

LIST OF FIGURES

LIST OF TABLES

Chapter I
INTRODUCTION

1.1 Background

The rapid depletion of fossil fuel reserves[1] along with global trend for increasing energy demand and threat of irreversible climate change requires the need for a transition to a low carbon economy and efficient environment-friendly energy system[2]. Due to its non-renewability, fossil fuel reserves cannot be restored easily. This identifies the risk of energy shortage a pressing problem that we have to deal immediately. Among the alternatives, considerable effort has been given to hydrogen that has attracted extensive attention among research groups[3–5] and environmental organizations worldwide[6 –10]. Hydrogen does not release carbon when combusted or when used in a fuel cell thereby making it a high quality, valuable fuel. At present, the bulk of hydrogen is generated by steam reforming which is the most common and least expensive method for its production[11]. However, steam reforming and such related technologies mainly use fossil raw materials such as natural gas and coal that has a negative impact on the environment[3]. Therefore, it is crucial to look for alternative renewable resources.

Renewable energy sources such as biomass, hydropower, geothermal, wind and solar play vital roles in solving many of the current sustainability issues concerning environmental pollution and global warming. From the viewpoint of food sustainability, the utilization of non-food biomass such as waste vegetable oil is recommended. In Japan, an estimated 100 – 140 kt of waste vegetable oil is contributed by the household sector and 310 kt of trap grease from the industrial sector are being discarded every year[12]. Waste vegetable oil is also considered as a low-cost biomass feedstock and is usually utilized for the production of biodiesel with an energetic content comparable to that of a diesel fuel. However, such feedstock contains high water content; therefore, a pretreatment process is a must to reduce its water content (< 0.1 wt. %) making it suitable for biodiesel conversion[13].

Recently, biomass gasification using supercritical water (SCW) has been receiving much attention from the research community. Supercritical water gasification (SCWG) is an innovative biomass conversion process which utilizes the unique properties of

supercritical water (temperature above 374 °C and pressure above 22.1 MPa) that enables the transformation of biomass into hydrogen-rich gaseous products[14,15]. Since water is used as a reaction medium, a drying step is not required making waste vegetable oil a suitable feedstock for the reaction.

Current research on SCWG focuses on how to reduce the operating cost and equipment investment. Gasification using supercritical water requires high temperature and pressure to meet its required minimum reaction condition. One available option to meet these requirements is to reduce the activation energy by adding suitable hydrothermal catalyst[16]. The use of catalysts for SCWG can reduce the required reaction temperature but the efficiency of this process is currently limited by catalyst deactivation[17]. There are two types of catalysis approach. Homogeneous catalysis method uses alkali hydroxides and carbonates while heterogeneous catalysis requires the use of metal catalyst such as nickel and ruthenium. Among the studies involving the use of different metal catalysts in SCWG, several researchers pointed out the desirable catalytic activity and stability of nickel catalyst during SCWG of lignocellulosic[18–21] and proteinaceous[22–24] biomass. While catalyst deactivation is inevitable, most of its consequences may be slowed down or avoided. Enhancing the catalyst lifetime could increase the efficiency of the overall process. Therefore, further research on catalysis is of vital importance to the further development of SCWG process.

1.2 Objectives

The objectives of this research are:

- to study the supercritical water gasification process for hydrogen production
- to investigate the mechanism of nickel catalyst deactivation in supercritical water gasification of waste vegetable oil

Specifically, it aimed:

1. to see the effects of process parameters on the process
2. to determine the main cause of nickel catalyst deactivation in SCWG

1.3 Significance of the study

With the increasing prices of crude oil in the international market and the resulting concern over energy security, developing nations need to explore alternative and cheap sources of energy to meet the growing energy demand. Water is an abundant, non-toxic, safe and cheap solvent for many biochemical and chemical reactions. Gasifying wet streams of biomass in supercritical water is an economical and viable approach to dispose and convert them into energy source[25]. Since water is the reaction medium for this process, high moisture content material could be fed without the need for drying pretreatment methods. Conventional gasification methods require the moisture content of feedstocks to be as low as 10 – 20 % which involves high energy and operational cost. This results to overall system inefficiency and potentially reduces the combustion temperature way below its optimum[26]. SCWG does not necessitate drying procedures as water coming from the wet feedstock is used as a solvent as well as a reactant. Therefore, hydrogen from the biomass feedstock as well as hydrogen from water is gained.

Previous studies found out that high hydrogen yield can be obtained only if the operating conditions are higher than 600 °C and 30 MPa[16][27]. Therefore, its economic efficiency has become the greatest challenge to the further development of SCWG. Using hydrothermal catalyst can reduce the operating temperature but catalyst stability is sometimes not high enough. Oftentimes, exposure to severe operating condition leads to catalyst deactivation. Therefore, the research on catalysis concerning biomass SCWG is of vital importance to this technique. Knowing the mechanism of catalyst deactivation could develop ways on how to enhance its catalytic lifetime.

The real biomass to be used in this study is canola oil which is a representative biomass of waste vegetable oil. Using this biomass as feedstock for SCWG process is a practical option since its disposal and bioenergy conversion are attained at the same time. The heterogeneous metal catalyst to be used in this study will be nickel catalyst, which is known for its stability and longer catalytic lifetime. Determining the mechanism of nickel catalyst deactivation in SCWG could help develop ways on how to lengthen its catalytic lifetime. Consequently, this could avoid the consequences brought about by its deactivation and may contribute to SCWG's development and economic efficiency.

1.4 Structure of the thesis

CHAPTER 1: INTRODUCTION – discusses the background, objectives, and significance of the study. The structure of the thesis is also presented.

CHAPTER 2: REVIEW OF RELATED LITERATURE – covers the discussion about supercritical fluid gasification technology along with its fundamentals, latest scientific trends and areas for improvement. It also tackled the field of catalysis, one of the fundamental aspects in the development of SCWG technology.

CHAPTER 3: METHODOLOGY – includes the description of the feedstock and catalyst used in the study. It also describes the experimental design and procedure along with the analytical methods used in the study.

CHAPTER 4: RESULTS AND DISCUSSION: Decomposition of oil in supercritical water gasification – discusses the results obtained from experimental and analytical methods. It includes the discussion of oil conversion into gaseous products as evaluated by varying the biomass concentration.

CHAPTER 5: RESULTS AND DISCUSSION: nickel catalyst deactivation – tackles the issue of catalyst deactivation in SCWG of oil. The loss of catalyst efficiency was determined by adding supplementary experiments and analysis. This chapter mainly focuses on the results of catalyst characterization conducted before and after the reaction. A conclusion was drawn after observing the chemical and physical changes of the catalyst in line with its deactivation behavior.

CHAPTER 6: CONCLUSION AND RECOMMENDATION – summarizes the major findings of this research, points for improvement, and recommendations for future work.

1.5 Scope and limitations of the study

This study aimed to determine the major cause of nickel catalyst deactivation in supercritical water gasification of waste oil.

This study was designed on a bench scale, flow type setup. Two types of pumps were used to deliver the reactants to the system. A slurry pump was used to deliver water while a plunger pump was used to deliver oil.

This study was limited to the use of canola oil as a representative biomass of the study. A single brand (AJINOMOTO) of canola oil was used in all experiments. Furthermore, this study only used a single type of nickel catalyst (granulated) from one supplier (Nikko Rika, Japan).

The operating parameters evaluated in the study were biomass concentration, catalyst amount and gasification time. All gasification experiments were tested at fixed operating conditions of 400 °C, 25 MPa and retention time of 4.5 s.

The study was conducted at Environment Science Center, The University of Tokyo Kashiwa Campus. It was conducted under the supervision of Associate Professor Teppei Nunoura and Assistant Professor Osamu Sawai of Nunoura Laboratory.

Chapter II
REVIEW OF RELATED LITERATURE

This chapter is divided into six sections. It presents the fundamental backgrounds and principles of SCWG as well as the current trends and scientific advances in this field from literature. In this chapter, the first section introduces the concept of supercritical water and its fundamental chemical theory. The second section reviews the related studies done at different operating parameters such as temperature, pressure, and biomass amount. It also includes the experimental studies done using different types of biomass mainly, lignocellulosic and proteinaceous biomass. A section presenting a review on catalytic SCWG is also included. It compares the performance of different types of catalyst used during SCWG. Also, it presents related studies that tackles the issue of catalyst deactivation. The last section presents the fundamental theories of the experimental design which involves fluid mechanics and thermodynamic calculations.

2.1 Supercritical water gasification

The study of an innovative method of converting biomass with high moisture content into viable syngas has been acknowledged by research communities and researchers worldwide. Supercritical water gasification (SCWG) uses water as the reaction medium that does not necessitate a drying step unlike other conventional methods such as pyrolysis and combustion[8]. An alternative method for converting wet biomass such as sewage sludge and manure is anaerobic digestion. However, this process presents drawbacks such as longer residence times (up to four weeks) and slow reaction rates[28]. At supercritical conditions, rates of reaction are accelerated that results to the shortening of residence times in the order of minutes[29]. Figure 2-1 adapted from Yakaboylu (2013)[31] shows the supercritical phase of water above its critical point of 374 ℃ and 22.1 MPa. Water at this condition holds desirable physical properties that are mainly exhibited by its density, static dielectric constant and ion dissociation constant. Figure 2-2 adopted from He (2014)[28] shows that beyond the critical point of water, density, static dielectric constant and ion dissociation constant decrease drastically thereby causing the rate of reaction to accelerate remarkably. Due to these property enhancements, water acts as a non-polar solvent with high reactant diffusivity, exceptional transport properties and solubility[30].

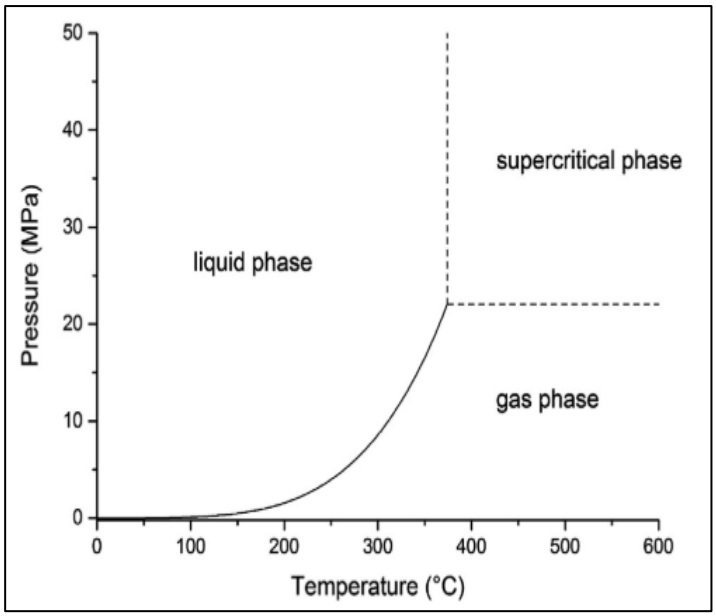

Figure 2-1. Schematic phase diagram of water[31].

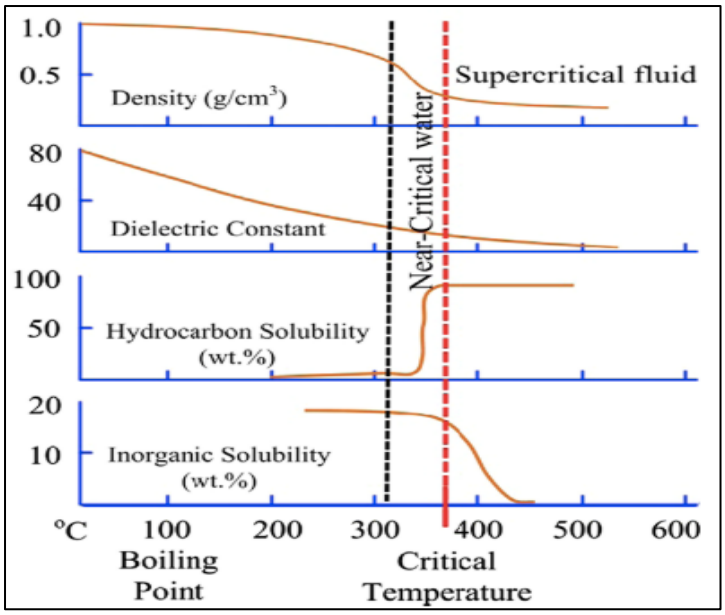

Figure 2-2. Properties of water above its critical temperature (Tc) and pressure (Pc)[29].

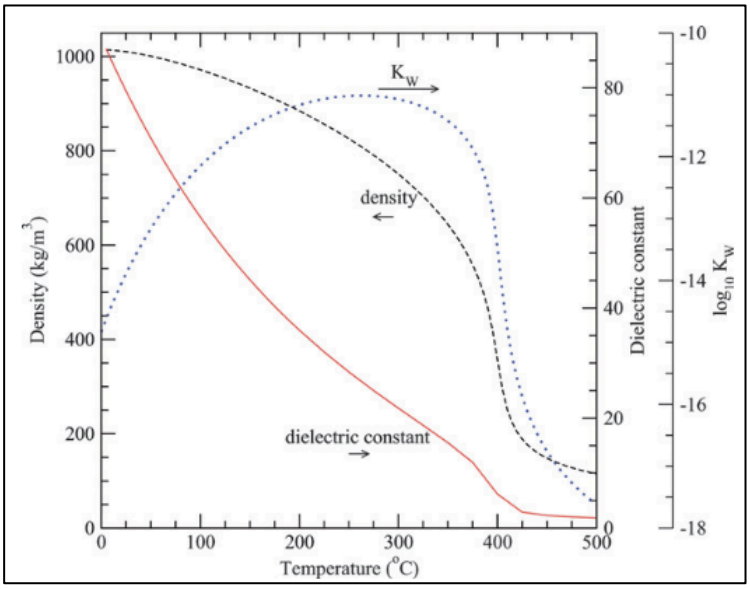

Figure 2-3. Density, static dielectric constant and ion dissociation constant (K_W) of water at 30 MPa as a function of temperature[32].

Peterson (2008)[32] gave a detailed explanation of how these properties change as water is heated as shown in Figure 2-3. Figure 2-3 illustrates the range of property changes that occur. Beyond the critical temperature of 374 °C, the solvation behavior of water significantly changes from a polar, highly hydrogen-bonded solvent to that of a typical non-polar solvent. Notable change can be seen for density as it drops from liquid-like (about 800 kg m^{-3}) to dense gas-like (about 150 kg m^{-3}) conditions as the temperature elevates from 300 °C to 450 °C. These density changes link with other macroscopic properties to reflect changes at the molecular level such as solvation power, degree of hydrogen bonding, polarity dielectric strength, molecular diffusivity and viscosity. From the figure above, it can be seen that dielectric constant decreases from approximately 80 °C to 25 °C to less than 2 at 450 °C while the ion dissociation constant first increases from 10^{-14} to 10^{-11} just below 350 °C and then decreases by five orders of magnitude above 500 °C. The ion dissociation or self-ionization constant, is the product of the acidic and basic concentration forms of water, $K_W = [H_3O^+][OH^-]$, in units of $mol^2\ kg^{-2}$.

2.2 Process Parameters in SCWG

2.2.1 Effect of temperature

Three main reactions[33] were identified in SCWG process which includes steam reforming, water gas shift, and CO and CO_2 methanation reactions as presented by Equations 1-1 to 1-3, respectively.

$$C + H_2O \rightarrow CO + H_2 \qquad \Delta H = +132 \text{ kJ mol}^{-1} \qquad [1\text{-}1]$$

$$CO + H_2O \leftrightarrow CO_2 + H_2 \qquad \Delta H = -41 \text{ kJ mol}^{-1} \qquad [1\text{-}2]$$

$$CO + 3H_2 \leftrightarrow CH_4 + H_2O \qquad \Delta H = -206 \text{ kJ mol}^{-1} \qquad [1\text{-}3]$$

Researchers such as Lan[34] and Li[35], both from State Key Laboratory of Multiphase Flow in Power Engineering, Xi'an Jiaotong University in China, stated that the effect of temperature can be predominantly observed during SCWG process. It should be considered as the most important parameter due to its significant influence during the process. Boukis et al.[36]conducted a series of experiments using corn silage and ethanol sludge in SCW at temperature range of 540 – 600 °C. From their research, it was found out that reaction temperature had a positive influence on carbon gas yields. Using SCW, de Jesus et. al[37] gasified corn silage at temperature and pressure ranges of 300 – 700 °C and 25 – 40 MPa. At lower temperatures (T < 500 °C), gasification yield was too low that hardly any gas was produced. At higher temperatures (T > 600 °C), the production of H_2 was favored. At 700 °C, an almost complete total conversion was achieved. With increasing temperature, the amount of CO in the gas product decreased. At T > 600 °C, CO concentration was less than 1%. This increase in H_2 and decrease in CO production in the gas phase suggest that water gas shift reaction was accelerated with increasing temperature at supercritical water conditions.

The types of reaction mechanisms present at SCW conditions were also identified from the results obtained by Promdej and Matsumura[38]. By performing SCWG of glucose at temperature range of 300 – 460 °C at 25 MPa, they identified two types of reaction mechanisms – ionic and radical reactions. Under subcritical condition (T < 374 °C), the reaction mechanism is ionic. At supercritical condition, the mechanism is radical. This is concept is backed up by the research findings of Kruse et al.[39]. From the findings of their research, it was revealed that as temperature increases, density and ionic product decrease

and the process shifts to radical reactions. Beyond the water's critical point, free radical reaction and gasification efficiency were enhanced.

2.2.2 Effect of pressure

Studies conducted to investigate the influence of pressure on SCWG had seen its minimal effect on the overall efficiency of the process[40–42]. In the SCWG of glucose, Hao et al.[40] concluded that pressure did not have a great effect on gasification efficiency and gas product composition. Authors such as Matsumura et al.[41] also had the same observation. During the SCWG of coconut shell activated carbon, they concluded that varying the pressure from 25.5 – 34.5 MPa did not have much effect on gas composition. According to Kruse et al.[42], pressure decrease leads to an increase of H_2 formation. Based on the results of SCWG of pyrocatechol at 700 ℃ and pressure range of 0.01 – 40 MPa, H_2 and CH_4 yield decreases and increases, respectively as pressure increases. Meanwhile, the composition of other gases had changed slightly. From this, it was concluded that the dependence of gas composition on pressure is negligible. Figure 2-4 presents the results of their study.

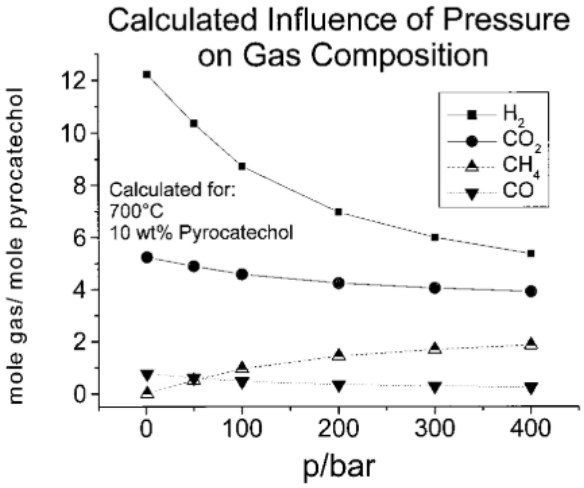

Figure 2-4. Calculated equilibrium data of the relative gas yields as a function of pressure at 700 °C and 10 wt. % pyrocatechol[42].

This is also in agreement with the results obtained by de Jesus et al.[37] during SCWG of corn silage. Their results revealed that pressure has a negligible effect on the gasification of corn silage. Researchers such as Buhler and Dinjus[43] proposed two competing reaction pathways. First is the ionic reaction pathway, which is favored at low temperature and high pressure. Second is the free radical reaction pathway, which is favored at high temperature

and low pressure. Since desired gas products (e.g. H_2) are produced from free radical reactions, high temperature and low pressure are preferred[33].

2.2.3. Biomass for SCWG

2.2.3.1. Utilization of biomass feedstocks for SCWG

Demirbas[44] cited some of the advantages of biomass utilization for H_2 production. The most notable is its independence from oil imports, where net products remain within the managing country and estimated improvement of CO_2 balance in the atmosphere is around 30%. According to the US National Research Council[45], two types of biomass feedstock are desirable for hydrogen production: (i) dedicated bioenergy crops, (ii) less expensive organic waste residues such as non-food and agricultural biomass. To evaluate the effectiveness of SCWG, Azadi and Farnood[46] cited that there are two varying types of biomass feedstocks that are typically studied in laboratories: real biomass and model compounds. Experiments conducted using real biomass feeds offer concrete evidence on the actual performance of the process. On the other hand, model compounds are used to conduct fundamental studies with an aim of representing the actual gasification conditions. However, it should be noted that despite the existence of property similarities of real biomass and model compounds, their gasification results may significantly differ in the rate of catalyst deactivation. According to Afif et al.[47], this is partially influenced by the existence of sulfur and other inorganic impurities found in real biomass feedstock. Such impurities may react with the active metal and form a less active surface or may deposit into the catalyst pores thereby reducing the number of accessible sites. Nevertheless, if we take the concept of projecting these laboratory-scale experiments into industrial scale, surely there is a need to conduct an in-depth investigation of catalytic SCWG using real biomass to further determine which part of the process needs further enhancement.

2.2.3.2. Effect of biomass concentration

In a study conducted by Yu et al.[48], glucose was gasified at 600 °C at 34.5 MPa in SCW using tubular flow reactors. Their results presented in Figure 2-5 revealed that the yields of H_2 decrease while CH_4 yields increase as glucose concentration increases. The experiments were carried out using tubular flow reactors made of Inconel and Hasteloy.

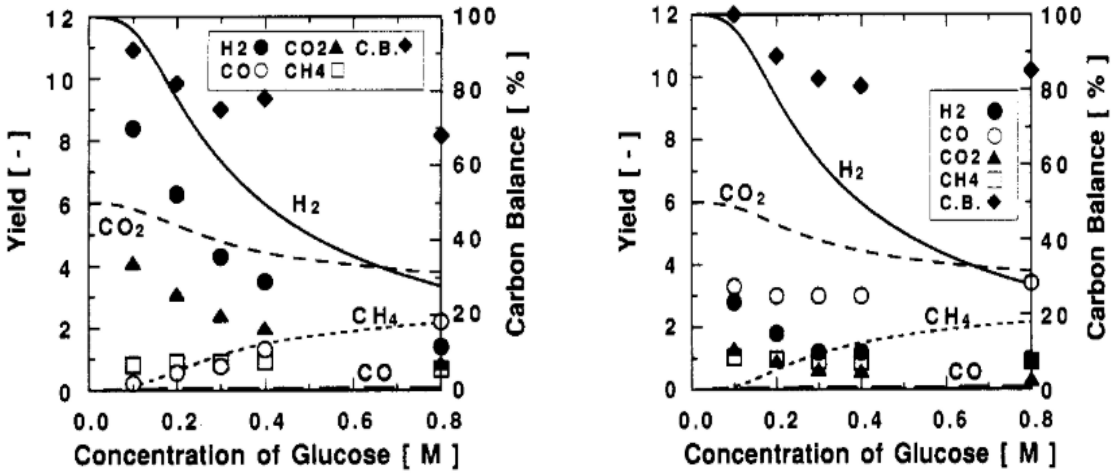

Figure 2-5. Effect of reactant concentration on gasification[48]. Lines, equilibrium data; Symbols, experimental data at 600 ℃, 34.5 MPa, 34 s using the Inconel SCCFR (left) and Hasteloy SCCFR (right) flow reactor.

The same trend was observed by Kruse et al.[49] when they gasified chopped mixture of carrots and potatoes at 500 ℃ and 30 MPa using a continuous stirred tank reactor (CSTR). It was found out that the gasification efficiency decreases if dry matter concentration increases. Matsumura et al.[50] acknowledged that high gasification efficiencies are possible at high temperature (temperature range 500 – 800 ℃) SCWG. However, the results suggested that as the organic feedstock (glucose) concentration increases, gasification efficiency drops. In terms of gas yields, they observed that H_2, CH_4, CO_2 yields decreased if glucose concentration was increased; however, an increase in CO yield was observed. In another contrasting study using glucose as model biomass and using a tubular reactor, Hao et al.[40] observed that H_2 and CO_2 yields increased with increasing glucose concentration in the range of 0.1 M to 0.9 M; on the other hand, reduction in CO and CH_4 yields was observed. Investigation of the effect of biomass concentration using real biomass was also done. Gasification using wood sawdust[47–49] and corncob[53] in SCW revealed that both gasification efficiency and carbon conversion efficiency were lower in experiments carried out using higher biomass concentration than lower concentration experiments. For liquid feeds, the effect of biomass concentration was found to have a similar impact on the overall process. Boukis et al.[36] used methanol (CH_3OH) in SCW and found out that as CH_3OH molar ratio to water was decreased from 32 to 25 vol%, H_2 yield increased.

2.2.4. Catalyst for SCWG

Tang et al.[54] developed a thermodynamic model to estimate the equilibrium composition of different biomass types during SCWG. Their calculation results revealed that during non-catalytic reactions: (i) In high temperature range of > 600 °C, CO yield is highly significant, (ii) In response to high CO yield, H_2 and CO_2 yields are low, (iii) In low temperature (near-critical) conditions, CH_4 concentrations are lower. These results led them to conclude that catalysts are needed to support H_2 production via the water-gas shift reaction (Equation 1-2) and the formation of CH_4 through methanation reaction (Equation 1-3) to reach equilibrium yields. In a non-catalytic SCWG, Lee et al.[55] studied the decomposition of glucose at 480 – 750 °C, 28 MPa using a tubular reactor. It was found out that CO content was relatively high. Its production only slowed down when temperature reached above 650 °C. They suspected that this is due to the start of water-gas shift reaction. Reduction of high energy input with maximum H_2 yields implies the significance of using catalysts during SCWG[56].

The use of catalysts is known to qualitatively and quantitatively vary the composition of reaction products during SCWG. Sinag et al.[57]investigated the gasification performance of glucose in SCW at 500 °C, 30 MPa, and 1 hr reaction time in a batch reactor. They performed a non-catalytic experiment and catalytic gasification using two different catalysts – K_2CO_3 and Raney nickel. The results suggest that H_2 yields increased twice as much as without catalyst in the presence of K_2CO_3. Water-gas shift reaction was also enhanced as evidenced by low CO production. The use of Raney Nickel, which is known as a hydrogenating catalyst, favored the formation of CH_4. The addition of K_2CO_3 and Raney nickel catalyst led to a reduced yield of unwanted furfurals and increased the yield of desired gases such as H_2 and CH_4.

In 1981, Mudge et al.[58] published a work about steam gasification of wood using alkali carbonates and naturally occurring minerals as catalysts. They concluded that an effective catalyst for CH_4-rich gas production should have a property which includes (i) having a nickel content of 30 wt% or greater, (ii) a BET surface area of 100 $m^2\ g^{-1}$ or greater and (iii) nickel surface area of 30 $m^2\ g^{-1}$ or greater. In early 1990's, pioneering work in the field of hydrothermal gasification using catalysts had been carried out[51]. Researchers such as Elliot et al.[19] and Sealock et al.[59] were the first ones to investigate the biomass gasification performance using catalysts at the Pacific Northwest National Laboratory. Their scientific advances resulted to the development of a pressurized catalytic gasification

process operated at low-temperature under the trade name TEES (thermochemical environmental energy system) process. The TEES process typically operated at sub-critical region (350 ℃, 20 MPa) and was able to perform processes including steam reforming, water-gas shift and methanation reactions. Several catalysts were tested and evaluated for long-term operation. Among the catalysts, ruthenium, rhodium and nickel were identified as active metal catalysts. Throughout the development and scaleup of TEES, nickel catalyst had been chosen to be used in the system[19]. Since then, SCWG studies using nickel as catalyst had been published and several authors had pointed out its desirable catalytic performance in increasing the H_2 content of the resulting gas[59–61].

Recent studies by Guo et al.[16] and Azadi et al.[46] pointed out the desirable catalytic performance of nickel and ruthenium among metal catalysts during biomass SCWG. Since nickel offers a comparably lower cost than other metal catalysts, it is widely used in industrial processes. Subsequently, most of the studies utilized commercially available nickel catalysts for steam reforming of CH_4 and higher hydrocarbons[63]. Using sawdust and rice straw as real representative biomass, Yoshida et al.[21] used nickel catalysts in SCW at 400 ℃ and 25 MPa. Catalyst deactivation was observed; however, it was concluded that if sufficient amount of catalyst is used, high gasification ratios could be achieved. These studies generally show that using nickel as a catalyst for SCWG process has advantages in terms of economic performance among other metal catalysts.

2.2.5 Catalyst deactivation in SCWG

From previous discussions, it was known that developing catalysts suitable for the SCWG processing environment is important to make this process economically viable. The identification of active catalyst in SCWG and their catalytic behavior has been studied by by Elliott et al.[64] using 10% phenol as a model waste in water. Studies involving catalyst deactivation in hydrothermal gasification conditions have been published by Osada et al.[65-66] using a lignin model and Nguyen et al.[24-25] using ethanol fermentation stillage. Elliott et al. formulated and tested improved catalysts for hydrothermal gasification at constant operation conditions of 350 °C and 21 MPa. They were able to identify catalytically active metals that were limited to nickel, ruthenium, and rhodium. To further extend the catalytic lifetime of nickel, it was stabilized by incorporating ruthenium, copper, silver, rhenium and tin. Also, from the results of their study, ruthenium was identified as a very stable metal during hydrothermal gasification. It was also able to promote methanation reactions. In

terms of support materials, monoclinic zirconia, rutile titania and carbon showed promising results. Osada et al.[65] initially published a study wherein they were able to explain the mechanism of sulfur atoms adsorption on ruthenium metal particles. From their research findings, it was found out that sulfur atoms inhibited the C-C bond breaking and methanation reaction due to the decrease of ruthenium ensembles responsible for these reactions. In their next study[66], an attempt was made to regenerate the catalyst, S-Ru/TiO_2, by removing the sulfur from sulfur-containing feedstock in subcritical water treatment (sub-CWT). Their attempt was successful and resulted to higher gas yields and methane composition. They concluded that streaming the catalyst in subcritical water treatment improves the catalytic gasification activity, therefore alternating SCWG and sub-CWT of the Ru/TiO_2 catalyst would provide a consistent high gasification performance. These results are presented in Figure 2-6.

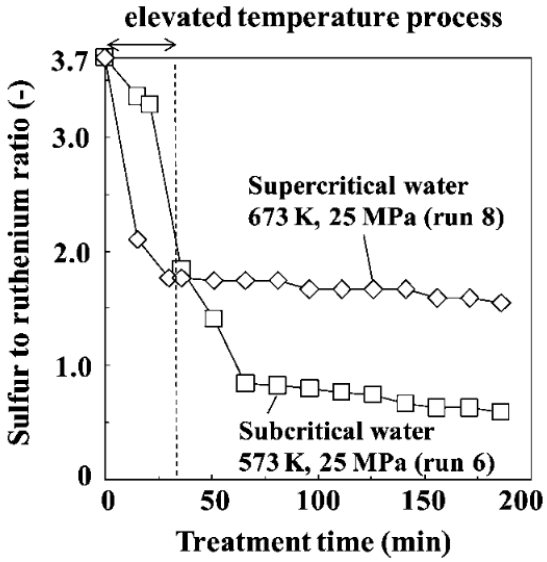

Figure 2-6. Sulfur to ruthenium ratio during the catalyst treatment under subcritical and supercritical water conditions[66].

In a recent study published by Nguyen et al.[24], they identified oxidation as the major cause of Raney-Ni catalyst deactivation in SCWG of ethanol fermentation stillage as model feedstock for proteinaceous biomass. In their next study[25], they attempted to mitigate the catalyst deactivation by reactor modification and methanol addition and these measures were met with certain success. Recommendation to further conduct a more detailed and elaborate study by exploring the surface chemical state of Raney-Ni catalyst was advised.

2.3 Design and operating parameters (flow reactor)

2.3.1 Residence Time

For batch reactors, the residence time (t) is the natural performance measure defined as the time duration that reactants stay inside the reactor[67]. For flow reactors, their proper performance measures are space-time (τ) and space velocity (s). Adopted from Levenspiel[68], the equations of space-time and space-velocity are described below.

$$\tau = \frac{1}{s} = \begin{pmatrix} \text{time required to process one} \\ \text{reactor volume of feed measured} \\ \text{at specified conditions} \end{pmatrix} = [time] \qquad [2\text{-}1]$$

$$s = \frac{1}{\tau} = \begin{pmatrix} \text{number of reactor volumes of} \\ \text{feed at specified conditions which} \\ \text{can be treated in unit time} \end{pmatrix} = [time^{-1}] \qquad [2\text{-}2]$$

The variation of density of the main reactant component (water) with temperature along the reactor should also be taken into consideration. The value for space-time and space-velocity depends on the temperature, pressure, and state (gas, liquid, or solid) at which the measurement of the volumetric feed flowrate (V_0) is taken. If they are assumed to be the stream entering the reactor, the relation between s and τ becomes:

$$\tau = \frac{1}{s} = \frac{C_{A0}V}{F_{A0}} = \frac{\left(\frac{\text{moles A entering}}{\text{volume of feed}}\right)(\text{volume of reactor})}{\left(\frac{\text{moles A entering}}{\text{time}}\right)} \qquad [2\text{-}3]$$

$$= \frac{V}{V_0} = \frac{(\text{reactor volume})}{(\text{volumetric feedrate})}$$

In this study, the simplified Equation 2-3 was used to describe the residence time used for flow experiments.

2.3.2 Design of the preheater and heat exchanger

Preheating of the feed is required to heat the reactants up to the desired reaction temperature. Figure 2-7 shows the pre-heater design. Figure 2-8 shows the temperature profile of the pre-heater. As adopted from Geankoplis[69], the length of the pre-heater tube is calculated using the heat transfer rate equation represented by Equation 2-4.

$$Q = \dot{m}Cp\Delta T = U_i A_i (T_O - T_i) = U_o A_o (T_O - T_i) \quad [2\text{-}4]$$

where; Q = overall heat transfer rate (W)

$\dot{m}$ = mass flowrate (kg s^{-1})

C_p= heat capacity (J $kg^{-1} K^{-1}$)

ΔT = differential temperature (K)

U_i = heat transfer coefficient inside the tube (W $m^{-2} K^{-1}$)

U_o = heat transfer coefficient outside the tube (W $m^{-2} K^{-1}$)

A_i = tube inner area (m^2)

A_o = tube outer area (m^2)

T_i = bulk or average temperature of the fluid (K)

T_o = temperature of the wall in contact with the fluid (K)

Since the temperature drop, $T_o - T_i$, is assumed to be constant for all parts of the heating surface, Equation 2-4 only holds at one point in the apparatus when the fluids are being heated.

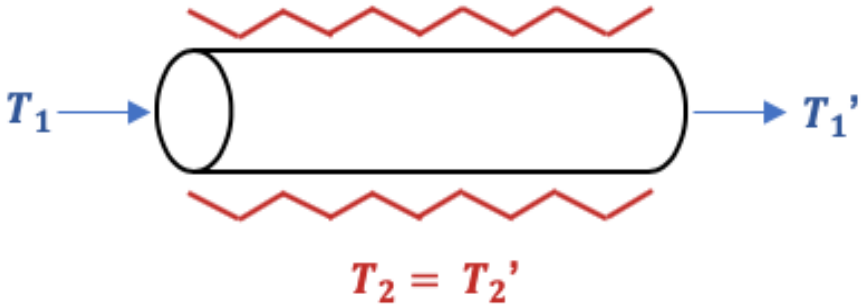

Figure 2-7. Design of a single tube pre-heater.

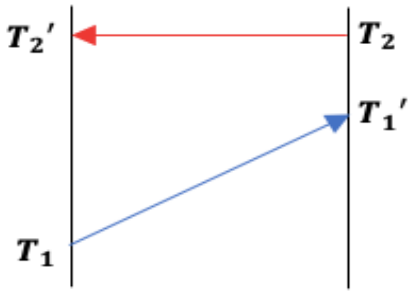

Figure 2-8. Pre-heater temperature profile.

As the fluids travel through the tube, they become heated or cooled and both T_i and T_O or either T_i and T_O vary. Then ΔT varies with position and a mean ΔT must be used for the whole system. Hence, in the case where the overall heat transfer coefficient U is constant throughout the equipment, and the heat capacity of each fluid is constant, the proper temperature driving force to use over the entire equipment is the log mean temperature force represented by Equation 2-5.

$$\Delta T_{LM} = \frac{\Delta T_2 - \Delta T_1}{\ln\left(\frac{\Delta T_2}{\Delta T_1}\right)} \; ; \; \Delta T_1 = T_2{}' - T_1 \text{ and } \Delta T_2 = T_2 - T_1{}' \qquad [2\text{-}5]$$

where; ΔT_{LM} = log mean temperature (K)

T_1 = initial temperature of the entering fluid (K)

$T_1{}'$ = final temperature of the entering fluid (K)

$T_2 = T_2{}'$ = set temperature of the heating element (K)

From Figure 2-7, the fluid enters at initial temperature T_1 and is being heated to a final temperature $T_1{}'$ as it moves along the tube by an external heating element set at a constant temperature $T_2 = T_2{}'$. Then, Equation 2-4 can be modified and rearranged as;

$$Q = UA\Delta T_{LM} \qquad [2\text{-}6]$$

where; U= overall heat transfer coefficient inside the tube (W m^{-2} K^{-1})

A = average heat transfer area (m^2)

Using a cylindrical surface area, $SA_{cylinder} = \pi D_i L$ [2-7]

where; D_i = inner tube diameter (m)

L = preheater length (m)

the preheater length could be estimated by rearranging Equations 2-6 and 2-7;

$$L = \frac{\dot{m}}{\pi D} \sum \frac{C_p \Delta T}{U \Delta T_{LM}} \qquad [2\text{-}8]$$

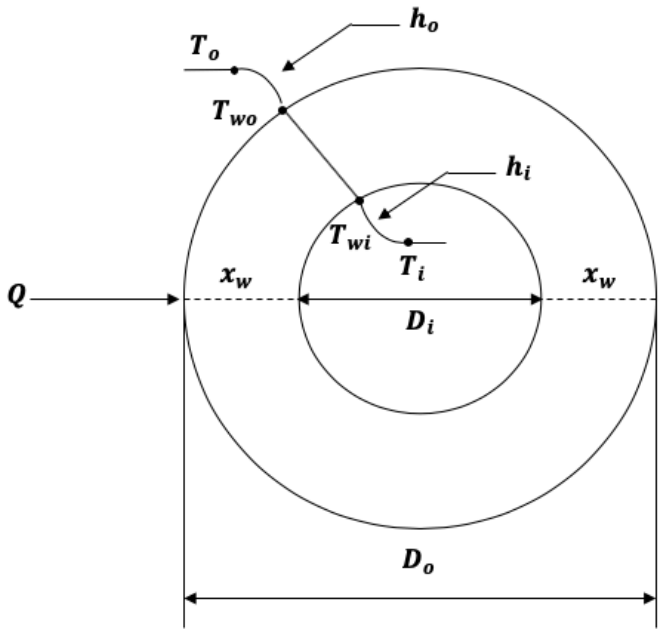

Figure 2-9. Heat flow in a cylindrical wall with convective boundaries.

Considering that a hot fluid at temperature Ti on the inside tube surface is being heated by a furnace with temperature To, an inside and outside convective or film coefficient (h_i and h_o, respectively) must be defined. The heat-transfer rate equation then becomes;

$$Q = h_i A(T_o - T_{wo}) = \frac{k_A A}{X_w}(T_{wo} - T_{wi}) = h_o A(T_{wi} - T_i) \qquad [2\text{-}9]$$

where; h_i = inside convective (film) coefficient (W m^{-2} K^{-1})

h_o = outside convective (film) coefficient (W m^{-2} K^{-1})

T_{wo} = outside tube wall temperature (K)

T_{wi} = inside tube wall temperature (K)

X_w = tube wall thickness (m)

Expressing $1/h_iA$, X_w/k_AA, and $1/h_oA$ as resistances, Equation 2-9 can be simplified as:

$$Q = \frac{T_o - T_i}{\frac{1}{h_i A} + \frac{X_w}{k_A A} + \frac{1}{h_o A}} = \frac{T_o - T_i}{\Sigma R} \qquad [2\text{-}10]$$

The overall heat transfer is then expressed in terms of an overall heat-transfer coefficient U defined by:

$$Q = UA\Delta T_{overall}\ ;\ \Delta T_{overall} = T_o - T_i \qquad [2\text{-}11]$$

Then, U can be calculated as:

$$U = \frac{1}{\frac{1}{h_i} + \frac{X_W}{k_A} + \frac{1}{h_o}} \quad [2\text{-}12]$$

In order to determine the values of h_i and h_o, it is crucial to determine the type of fluid flow, whether its laminar or turbulent since most of the resistance to heat transfer is in a thin film close to the wall. Film coefficients are also affected by the fluid's physical properties, its flow velocity, temperature difference, and geometry of the heat transfer vessel. To correlate these data for film coefficients, dimensionless numbers such as the Reynolds and Prandtl numbers are used. Reynolds number is determined by Equation 2-13 from Geankoplis (2003)[69]:

$$N_{Re} = \frac{D_i v \rho}{\mu} = \frac{4\dot{m}}{\pi D_i \mu} \quad [2\text{-}13]$$

where: D_i = inner tube diameter (m)
v = average fluid velocity (m s^{-1})
ρ = fluid density (kg m^{-3})
μ = fluid viscosity (Pa s)
$\dot{m}$ = mass flowrate (kg s^{-1})

The flow is considered laminar when the Reynolds Number (N_{Re}) in a specific tube is less than 2000. If N_{Re} exceeds 4000, the fluid is said to be in turbulent flow. Prandtl number physically relates the relative thickness of the fluid layer and thermal boundary layer. It is described by Equation 2-14.

$$N_{Pr} = \frac{\mu/\rho}{k/\rho C_p} = \frac{C_p \mu}{k} \quad [2\text{-}14]$$

where; μ/ρ = shear component for diffusivity for momentum
$k/\rho C_p$ = diffusivity for heat
k = fluid thermal conductivity (W m^{-1} K^{-1})

Nusselt number, N_{Nu}, is another dimensionless number used to relate data for the heat-transfer coefficient, *h* to the thermal conductivity *k* of the fluid and a character dimension *D*.

$$N_{Nu} = \frac{hD}{k} \qquad [2\text{-}15]$$

Referring to the Swagelok catalog (provided by the manufacturing company), an SUS $\frac{1}{8}$ inch tube with OD = $\frac{1}{8}$ inch has thickness (X_w) of 0.71 mm and can withstand a maximum pressure (P_{max}) of 58.5 MPa. Using the equations presented previously, Table 2-1 presents the estimated length of the preheater using a $\frac{1}{8}$ inch tube.

Table 2-1. Estimated required length of the preheater.

Temperature Range	Flowrate (mL/min)	Required Length (m)	Estimated Length to be used (m)
25 °C →	5	0.41	1.5
400 °C	10	0.59	1.5
	15	0.77	1.5
	20	0.95	1.5

For the heat exchanger design, the same principles of discussed previously were followed. As shown in Figure 2-10 and 2-11, T_1 and T_1' are the initial and final temperature of the feed solution and T_2 and T_2' are the initial and final temperature of the heating or cooling fluid. The heat exchanger used was designed to handle a counter-current flow with the hot fluid entering the inside tube while being cooled by the fluid entering the outer tube. A double tube heat exchanger was used as a basis for the computation. The hot gases will

enter the inner tube while being cooled by the counter-current flowing cooling water passing through the outer tube.

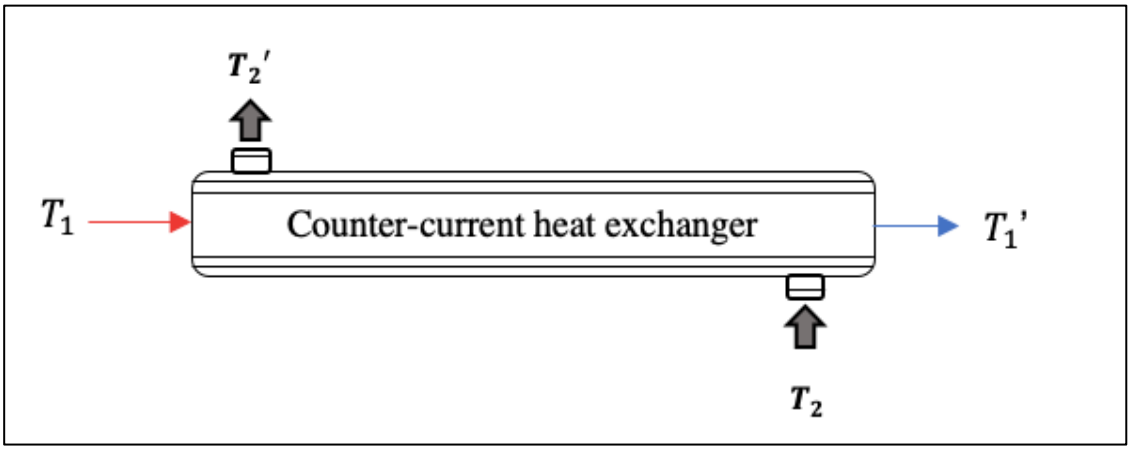

Figure 2-10. Design of the counter-current heat-exchanger.

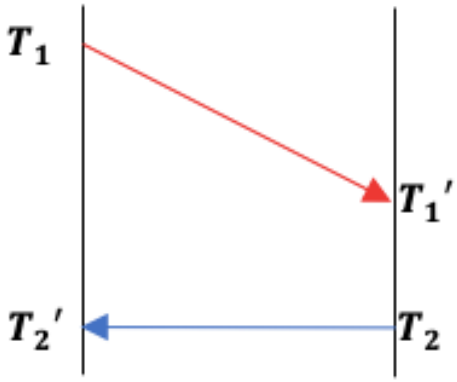

Figure 2-11. Heat exchanger temperature profile.

The inner tube has the following properties: OD = $\frac{1}{8}$ inch, X_w = 0.71 mm, and P_{max} = 58.5 MPa. While the outer tube has the following properties: OD = $\frac{3}{8}$ inch, X_w = 1.24 mm, and P_{max} = 33.0 MPa Assuming that cooling water cools the hot gases at a rate of 1200 mL/min and enters at an ambient temperature, the estimated heat exchanger length according to varying flowrates are presented in Table 2-2.

Table 2-2. Estimated required length of the heat exchanger.

Temperature Range	Flowrate (mL/min)	Required Length (m)	Estimated Length to be used (m)
400 °C → 25 °C	5	0.22	1.0
	10	0.43	1.0
	15	0.65	1.0
	20	0.87	1.0

Chapter III
METHODOLOGY

This study aims to investigate the main cause of nickel catalyst deactivation in supercritical water gasification of waste oil. This chapter discusses the experimental methodology done to conduct SCWG experiments. The first section presents the experimental conditions applied in the research. The second section gives a description of the methods and materials used to carry out the experiments. The third section presents the analytical procedures used to sample and analyze the reactants, gasification products and catalysts. The last section presents the results taken from preliminary testing of the experimental setup. All experiments were conducted at the Environmental Science Center, University of Tokyo Kashiwa Campus.

3.1 Experimental conditions

The experimental conditions applied in this study were suitably chosen to represent the SCWG of waste oil. Since the use of catalyst was employed in this study, minimal operating conditions are desired. Based on the catalytic SCWG of real biomass using nickel catalyst experiments conducted by Yoshida et al.[21], a fixed temperature of 400 °C was made constant in all experiments. From literature[40–42], varying pressure had minimal contribution in the change of gasification results. Therefore, a constant pressure of 25 MPa was applied in all experiments. Moreover, the operating parameters evaluated in this study were biomass concentration, catalyst amount and reaction time.

3.1.1 Effect of biomass concentration

To determine the suitable biomass amount for the SCWG experiment of waste oil, concentration was varied. Four biomass concentrations were tested: 2, 3, 4 and 5 oil wt%. The gasification products in gas and liquid phases were also analyzed to determine the possible decomposition pathway of waste oil at high and low concentrations.

3.1.2 Effect of catalyst amount

To determine the effect of catalyst amount on the gasification products, catalyst amount was varied at 10% and 20% reactor volume. An experiment was also conducted without the presence of catalyst to compare the difference in terms the gasification products. Between catalytic and non-catalytic SCWG, the gas products were sampled and analyzed to compare the differences in gas yields and efficiencies when catalyst amount is varied.

3.1.3 Catalyst deactivation

To observe the catalyst deactivation under chosen suitable biomass and catalyst amount, reaction time was varied by 60, 180, and 300 mins in reference to the contact time between the catalyst and biomass reactants.

3.2 Materials

3.2.1 Feedstocks

Canola oil (Ajinomoto) was chosen as the biomass in this study. It is mainly composed of C (77.51%), H (11.62%) and O (10.87%) as determined by CHN analysis. Its viscosity ranges from 56 – 189 mPa·s at temperature range of 0 – 25 ℃ as measured by Sine-wave Vibro Viscometer SV-10. In Japan, canola oil is the most used cooking oil which makes it a suitable representative biomass of waste oil[73]. In a study conducted by Chhetri et al.[74], it was found out that the physical and chemical properties of fresh and waste cooking oils were not different from each other. This suggests that the main functional groups of waste cooking oil remained unchanged after being used for cooking. For ease of conducting experiments, this supports the eligibility of using fresh oil as substitute for waste oil.

Deionized water was used throughout the experiments which was prepared in our laboratory using Milli-Q A10 (Millipore).

The catalyst used in the study was composed of Ni (67.2%), Al (31.9%), and Mo (0.9%) with an average surface area of 58.23 $m^2 g^{-1}$ and was purchased from Nikko Rica, Japan.

3.2.2 Experiment Setup

As seen in Figure 3-1, two types of pumps were used to deliver the reactants to the system. Slurry (Toyo Koatsu) and plunger pumps (Nihon Seimitsu Kagaku) were used to deliver water and oil, respectively. The laboratory-scale flow reactor (Figure 3-2) with an inner volume of 17.27 mL and the preheater (Figure 3-3) was made of stainless steel (SUS

316) tubing and Swagelok® SUS 316 fittings/valves. A cylindrical furnace was used to heat and maintain the temperature of both preheater and reactor at 400 ^{0}C. Aluminum gas bags (GL Science) were used to collect the gas produced by the reaction. Gas flowrate was measured by a gas flowmeter (GL Science).

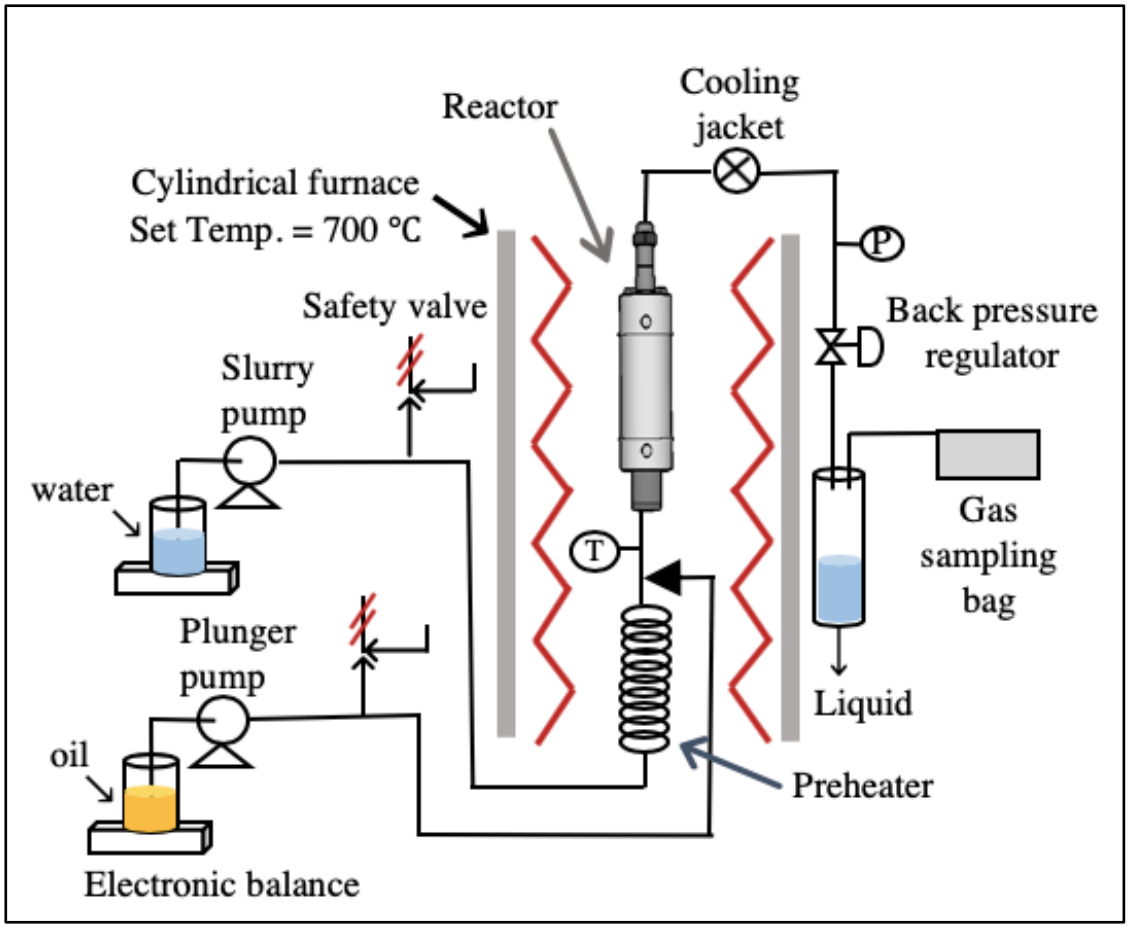

Figure 3-1. Schematic diagram of the SCWG experiment setup.

3.2.3 Experimental Design

3.2.3.1 Effect of biomass concentration

Four biomass concentrations were tested: 2, 3, 4 and 5 oil wt. %, hereby noted as SCWG 0.02, 0.03, 0.04 and 0.05, respectively. The oil and water proportions were determined from oil mass balance. An example calculation is presented in Figure 3-4. Table 3-1 summarizes the water and oil flowrate conditions. The plunger pump which delivers the oil to the system has a minimum flowrate of 0.45 mL min^{-1}. This limits the oil delivered to the system to a minimum concentration of 2 wt. % with water flowrate of 23.0 mL min^{-1}. Setting the water flowrate above 23.0 mL min^{-1} made the heating time up to 400 °C slower and reactor residence time shorter thus, it was decided to keep the water flowrate to 23.0 mL min^{-1} with a uniform

residence time of 4.5s. The issue with the plunger pump's minimum flowrate became one of the limitations of the study.

Figure 3-2. The reactor used in the study.

Figure 3-3. The preheater used in the study.

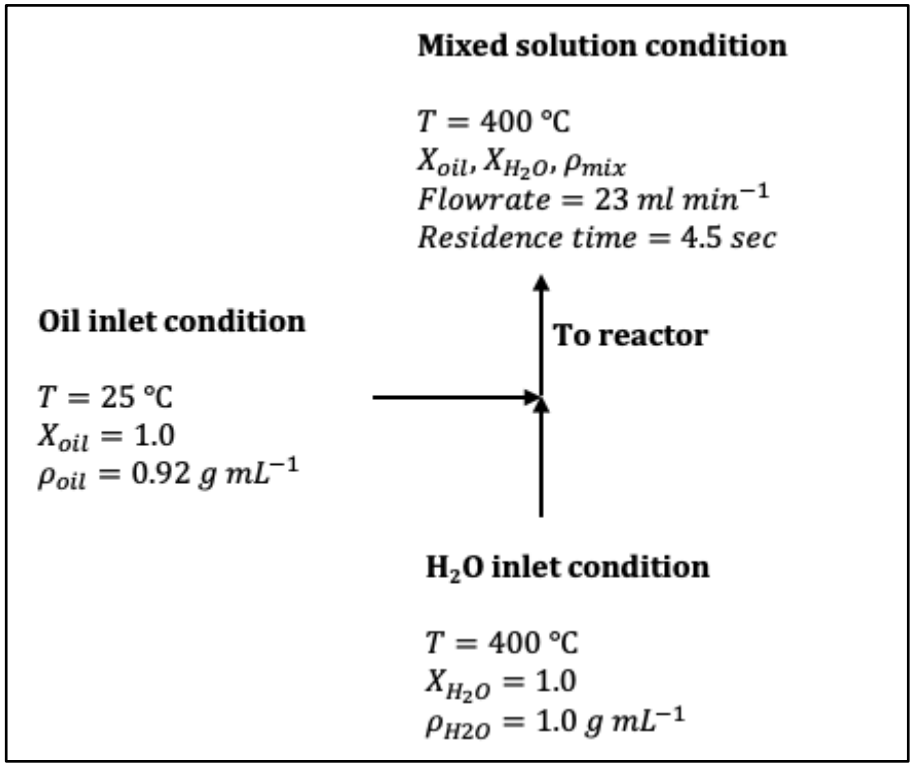

Figure 3-4. Sample calculation of conditions at the mixing point.

Table 3-1. Parameter summary of conditions at the mixing point.

Reactant	Inlet condition	EXPERIMENT RUN			
		SCWG 0.02	**SCWG 0.03**	**SCWG 0.04**	**SCWG 0.05**
H_2O	X_{H_2O}	1.0	1.0	1.0	1.0
	FR (mL min^{-1})	22.5	22.3	22.1	21.9
	ρ (g mL^{-1})	1.0	1.0	1.0	1.0
Oil	X_{oil}	1.0	1.0	1.0	1.0
	FR (mL min^{-1})	0.48	0.71	0.92	1.1
	ρ (g mL^{-1})	0.92	0.92	0.92	0.92
Mixed solution	X_{H_2O}	0.98	0.97	0.96	0.95
	X_{oil}	0.02	0.03	0.04	0.05
	FR (mL min^{-1})	23.0	23.0	23.0	23.0
	ρ (g mL^{-1})	0.99	0.99	0.99	0.99

Catalyst amount for each experimental run was made at 10% of reactor volume which corresponds to approximately 9.08 g catalyst. It was recommended to use 10 – 15 % catalyst amounts based on reactor volume to give sufficient headspace inside the reactor allowing

thorough mixing of reactants and catalyst through SCWG[75]. All experiments were conducted at 400 ℃ and 25 MPa.

Two types of pumps were readily available in the laboratory – the slurry and plunger pumps. While planning on how to proceed with the experimental design, careful considerations were made based on each pump's functionality. In Figure 3-5, the classification of pumps is presented.

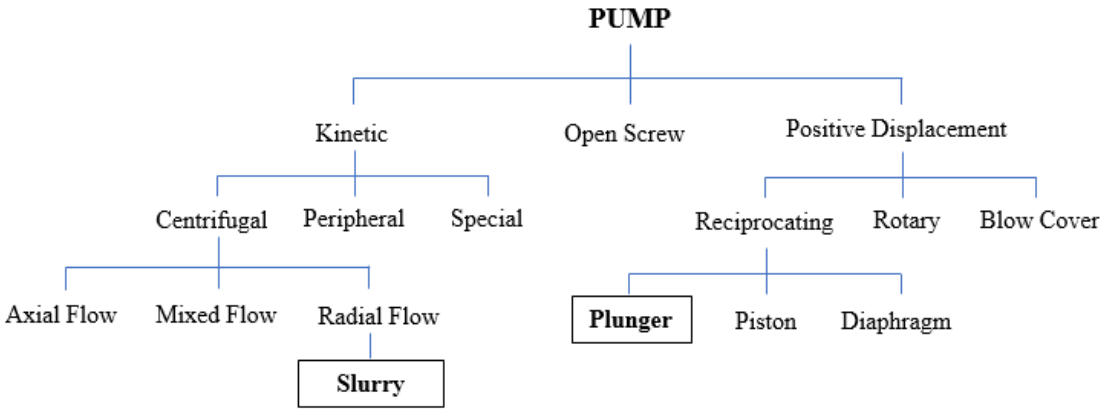

Figure 3-5. Classification of pumps[71].

A plunger pump falls under one type of reciprocating pumps that follow the principle of positive displacement. Positive displacement pumps are usually selected for their ability to handle high viscosity fluids at high pressures and relatively low flows as their efficiency is not affected by pressure. Due to the internal clearances high viscosities are handled easily and flow rate increases with increasing viscosity[76-77]. It works by trapping confined amounts of liquid and forces it from the suction to the discharge port. This produces pressure by creating flow. Figure 3-6 presents the simple structure of positive displacement and centrifugal pumps taken from Perry and Green[71]. The centrifugal slurry pump utilizes the centrifugal force generated by a rotating impeller to impart energy to the slurry in the same manner as clear liquid type centrifugal pumps. Flow rate rapidly decreases with increasing viscosity, even any moderate thickness, due to frictional losses inside the pump. As seen from the right-hand side figure, the mechanics of centrifugal pumps is as follows: first, the impellers (B) rotating within the stationary casing (C) pass on the velocity from the motor (outside source, A) to the liquid. The velocity head it has acquired when it leaves the blade tips is changed to pressure head as the liquid passes into the volume chamber and out the discharge E. This produced flow by creating pressure.

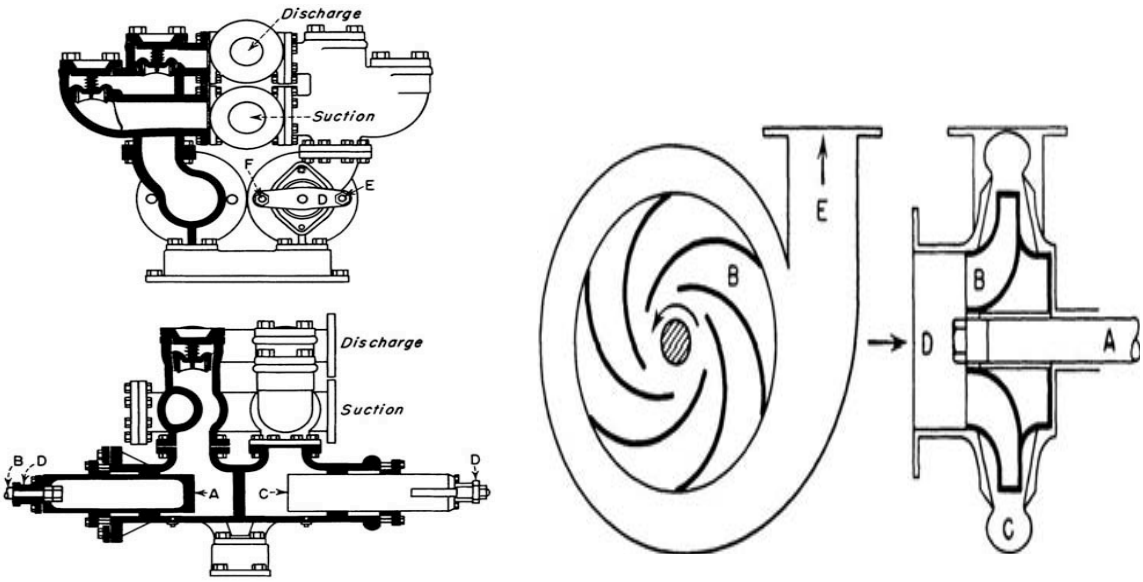

Figure 3-6. A duplex single acting plunger pump (left) and a simple centrifugal pump (right)[71].

Table 3-2. Summary of the main performance difference between positive displacement and centrifugal pumps[76].

Factor	Positive Displacement Pump	Centrifugal Pump
Viscosity	High viscosities are handled easily due to internal clearances. Flow rate increases with increasing viscosity.	Flow rate rapidly decreases with increasing viscosity due to frictional losses.
Efficiency	As viscosity increases, flow rate does too because the higher viscosity liquids fill the clearances of the pump, causing higher volumetric efficiency.	As viscosity increases, pump performance diminishes due to friction loss. Viscous drag imparts on the impeller, the pump's head and flow are reduced, and the horsepower required is increased.

In Table 3-2, the main function of each pumps was summarized according to performance category. Since the biomass used in this study is canola oil, using a positive displacement pump is suitable due to its highly viscous nature. Centrifugal pump was chosen to deliver water as its properties are appropriate to handle this fluid.

3.2.3.2 Effect of catalyst amount

Catalyst amount was varied at 10% and 20% based on reactor volume. For 10%, approx. 9.08 g (wet) catalyst was loaded while for 20%, approx. 18.09 g (wet) catalyst was loaded.

3.2.3.3 Catalyst deactivation experiments

After determining the suitable biomass concentration, catalyst deactivation was observed by varying the reaction time. Reaction times investigated were 60, 180 and 300 mins. The catalysts will be characterized before and after the reaction. Consequently, mechanisms will be proposed that best describes the deactivation behavior of the nickel catalyst.

3.2.3.4 Experiment procedure

The execution of each experiment has three parts – equilibrating the system, SCWG reaction and cooling the system.

I. Equilibrating the system

1) Secure the Swagelok fittings and make sure the screws are tightened accordingly.
2) Start equilibrating the system by allowing both pumps to deliver water. Again, check for any leakage.
3) After making sure that there is no leak, slowly build up the pressure by adjusting the back-pressure regulator up to 25 MPa. Check for leakage.
4) Once the desired pressure is achieved, shut both preheater and reactor inside the furnace (see Figure 3-8, left).
5) Turn on the furnace and set it to 700 °C. It approximately takes 1.5 hours for the system to reach 400 °C, depending on the ambient room temperature.

II. SCWG reaction

To determine the retention time of the reactant inside the whole system, ethanol (C_2H_6O) was used as a traced component and its concentration was analyzed using TOC analyzer. Table 3-3 presents the parameter conditions used to determine the system residence time of the reactants. Figure 3-7 shows the result of TOC analysis of C_2H_6O for the entire flow system. This data was used to appropriately calculate the residence time for the entire system at varying flowrates.

Table 3-3. Parameter conditions for retention time determination.

	Flowrate (mL/min)	H_2O fraction (X_{H2O})	C_2H_6O fraction (X_{C2H6O})
		$\rho_{H2O} = 1\ g/cm^3$	$\rho_{C2H6O} = 0.78\ g/cm^3$
Slurry Pump	2.7	1.0	0
Plunger Pump	0.37	0	1.0
System	3.0	0.90	0.10

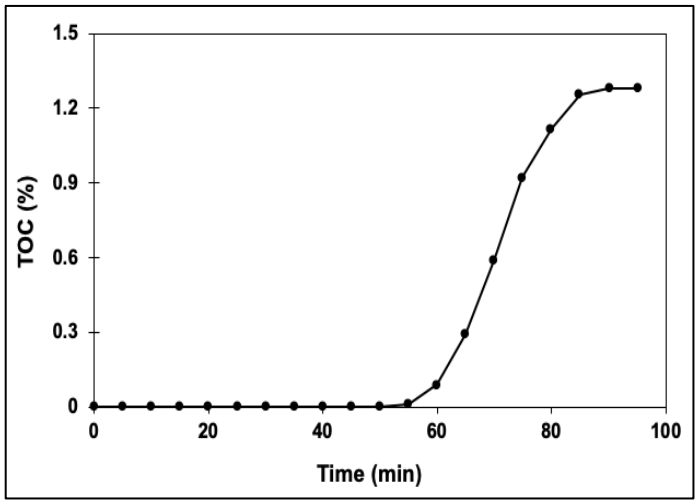

Figure 3-7. Determination of total system residence time of reactants using C_2H_6O.

1) Once system equilibrium was achieved, the plunger pump was switched to pumping oil.
2) To measure the gas flowrate, a gas flowmeter was used. Gas sampling was done every 30–min interval, with 20–min flowtime.

Gas flowrate measurement was done before the attachment of the gas bag and after its detachment. The sampling procedure followed is listed as follows:

a) Using the Luer-lock connector, connect the sampling tube of the flowmeter to the gas collector.
b) As seen in Figure 3-8, a gas flowmeter was used to determine the initial gas flowrate.
c) Attach the gas sampling bag and then start the timer for 20 mins.
d) After 20 mins, detach the gas bag.
e) Determine the final gas flowrate.
f) Repeat steps a) – e) with other gas samples.

The average value of the initial and final gas flowrates of each sample was calculated. This value was used to determine the amount of gas (V_{gas}).

3) Liquid samples were taken every 20–min interval. They were collected using 10 mL glass vials and stored in refrigerator.

III. Cooling the system

1) The plunger pump is then switched to pumping water instead of oil.
2) System was kept at 400 ℃, 25 MPa until there was no decomposed product or any oil residues left in the system.
3) After making sure that only water was coming out of the system, the furnace was switched off.
4) When the system cooled below 100 ℃ , pressure was lowered by releasing the back-pressure regulator.
5) Continuous flow of water was done until the system cooled to room temperature.

The procedures described were followed for all experiments. The next section will describe how product sampling and analysis were conducted. Figures 3-8 presents the furnace and gas flowmeter used in the study.

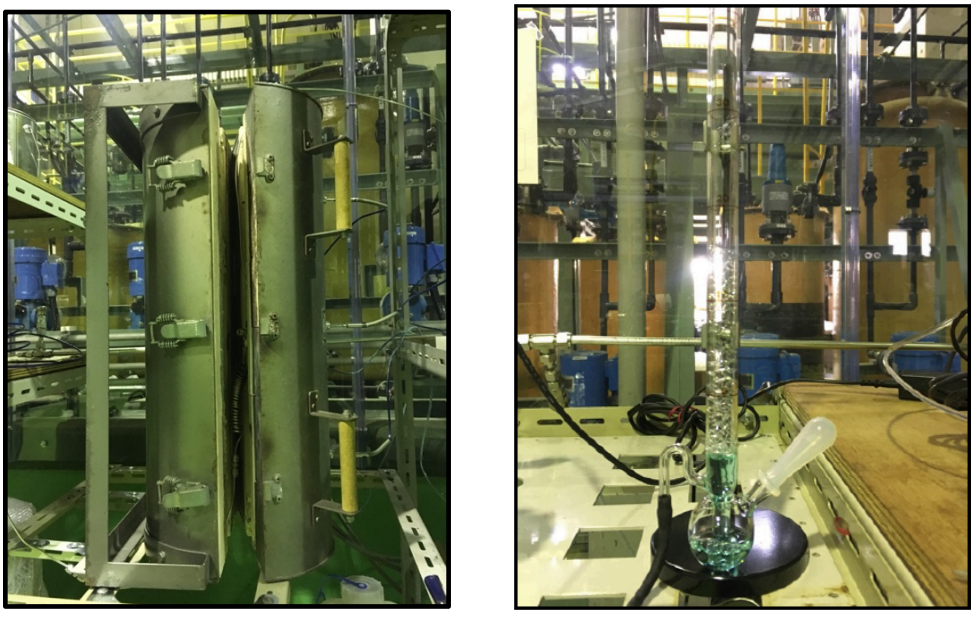

Figure 3-8. The cylindrical furnace (left) and soap-film flowrate meter (right) used in the study.

3.3 Analytical Methods

3.3.1 Liquid analysis

The liquid products obtained in each experiment were analyzed using Total Organic Carbon (TOC), Gas Chromatography – Mass Spectrometer (GC-MS) and High-Pressure Liquid Phase Chromatography (HPLC). To analyze the concentration of heavy metals in the samples, Inductively Coupled Plasma Mass Spectrometry (ICP-MS) analysis was carried out. The details of each analytical procedure are in the next sections.

3.3.1.1 TOC analysis

To determine the carbon content contained in a sample, the TOC 5000-A (SHIMADZU) Total Organic Carbon analyzer was used. The measurable analytes are Total Carbon (TC), Inorganic Carbon (IC) and Total Organic Carbon (TOC). To account for the overall carbon content needed for carbon balance, the TOC value was used. It works via combustion/non-dispersive infrared gas analysis method with combustion temperature at 680 °C. The carrier gas is air with an in-flow rate of 150 mL min^{-1}. Calibration curves for TC and IC analytes were made before each analysis using standard solutions. Below is the preparation procedure of each standard solution.

a) TC standard solution: 1000 ppm

   2.125 g of potassium hydrogen phthalate ($C_8H_5KO_4$) dissolved in 1000 mL H_2O.

b) IC standard solution: 1000 ppm

   3.50 g sodium hydrogen carbonate ($NaHCO_3$) + 4.41 g sodium carbonate (Na_2CO_3) dissolved in 1000 mL H_2O.

Calibration curves were made by diluting the stock solution down. The stock solutions were stored in the chiller for future use. Sample preparation and analysis were done according to the following procedure:

a) Samples were diluted with deionized water by a factor of 600. The decomposed samples are miscible with water and using a dilution factor of 600 is well within the detection limit of 100 ppm calibration curve for TC and IC.

b) The TOC value is calculated using the formula:

$$\mathrm{TOC\ (ppm)} = \mathrm{TC} - \mathrm{IC} \qquad [3\text{-}1]$$

After obtaining the TOC value, it will then be multiplied by the dilution factor to get the actual TOC in the samples.

c) Then the carbon present in the liquid phase could be calculated using Equation 3-2.

$$\text{C in liquid (\%)} = \frac{\text{mol C in effluent}}{\text{mol C in oil}} \text{ x } 100 \qquad [3\text{-}2]$$

3.3.1.2. GC-MS analysis

The purpose of this analysis is to identify the compounds present in the liquid phase. GC-MS analyses were carried out with a Shimadzu GC-2010, equipped with mass selective detector, MS QP-2010. Helium was used as the carrier gas. The electron ionization energy was 70 eV, ion-source temperature 200 °C and the interface temperature 280 °C. A fused silica column 5% phenyl-poly-dimethyl-siloxane (DB-5MS 30 m x 0.32 mm i.d. and 0.25 μm film thickness, J&W Scientific) was used. Data acquisition was performed with MassLab software for the mass ranges 30 - 300 m/z with a scan speed of 1 scan/s. The identification of compounds was performed by comparing their mass spectra with data from US National Institute of Standards and Technology (NIST, USA). A splitless injection at 250 °C injector temperature was employed. The oven temperature was programmed as follows: from 50 °C (3 min hold) raised at 2 °C/min to 250 °C (20 min hold). Total analysis time is 123 min. Figure 3-9 presents the temperature profile for this program.

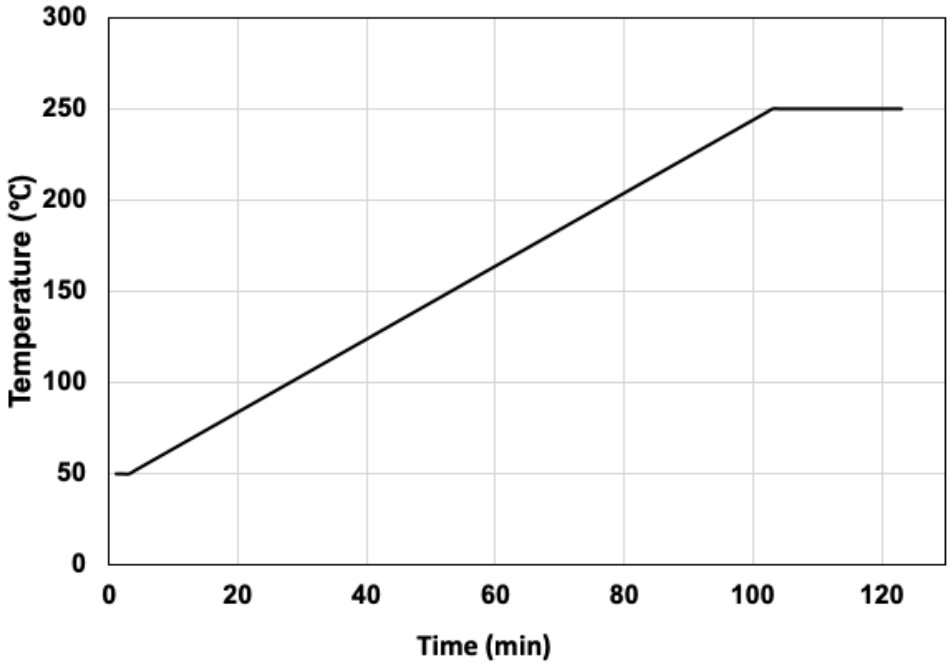

Figure 3-9. Temperature profile of the program used for GC-MS analysis.

The analysis was carried out as follows:

a) Preserved samples were subjected to 30 min ultrasonication to ensure homogeneity.
b) The sample concentration was adjusted by diluting with acetonitrile such that 10 vol. % was achieved. As an example, 0.2 mL sample was dissolved in acetonitrile to make a 2 mL sample for injection.
c) Using a gas-tight syringe, a sample of 2 μL was injected.

3.3.1.3. HPLC analysis

To quantify the compounds in the liquid samples, HPLC analysis was carried out. The HPLC system was JASCO LC Net II/ADC equipped with a UV-Vis photodiode detector (UV-2075 Plus) and refractive index detector (RI-2031 Plus). The procedure was patterned after the methods published by Guarrasi et al.[78] for fatty acid analysis using HPLC. For the eluent, a mixture of acetonitrile, methanol, and n-hexane in the ratio 90:8:2 were prepared at an isocratic flow rate of 1 mL/min. The UV wavelength (λ) was set to a single value of 208 nm. YMC-Triart C18, an organic hybrid silica-based column was used. Column oven was set to 40 ℃. All mixtures tested were acidified with 0.2% acetic acid to stabilize the fatty acids in their associated form. Mixtures of standard FA's were prepared at different concentrations (500, 250, 100, and 50 ppm) to establish a calibration curve for each fatty acid. Two types of fatty acids were analyzed; saturated and unsaturated FA. For saturated FAs, stearic, linolenic and linoleic acids were prepared. For unsaturated FAs, oleic and palmitic acids were prepared. All standard solutions and samples were prepared and dissolved in HPLC grade acetonitrile. The sampling injection was set to 10 μL.

3.3.1.4. ICP-MS analysis

Quantification of nickel, aluminum and molybdenum in the liquid samples were conducted using ICP-MS (ICP 8500, SHIMADZU) analysis. The carrier gas used was Ar with gas cylinder pressure set at 0.75 MPa. First, standard mixtures of Ni, Al and Mo were prepared at 250, 100, 50, 25 and 10 ppb to draw a calibration curve. A 1% HNO_3 was used as a diluting solvent to make the standards. The SCWG samples were diluted by water up to 20 times. For each sample injection, at least 10 mL were prepared to make sure that sufficient sample is available for rinsing and analysis.

3.3.2 Gas analysis

To determine the composition of gas products, Gas chromatography (GC-2014) equipped with thermal conductivity detector (TCD) was used. Six types of gases were quantified namely, H_2, CO, CO_2, CH_4, N_2 and O_2. Calibration curves were made using 300, 500 and 1000 μL of standard gas which contains 5.59% H_2, 14.20% CO, 18.39% CO_2, 4.44% CH_4 and the rest is N_2 balance. Since the air present in the tip of micro syringe should also be accounted, a volume correction using the amount of oxygen was made. To analyze O_2, 500 μL of air was analyzed and the O_2 area obtained was subtracted to each O_2 area in the standard gas. A formula describing this calculation is represented by Equation 3-3. Table 3-4 presents the program configuration for the analysis.

$$\text{Correction value (mL)} = \frac{\text{Area } O_2 \text{ in standard gas}}{\text{Area } O_2 \text{ in air}} \text{ x 0.5 mL air} \qquad [3\text{-}3]$$

This correction value is the volume of air contained in the standard gas injected in GC.

Table 3-4. GC-TCD analysis conditions.

Parameter		Analyzed Gas	
		H_2, CO, CO_2, CH_4, N_2	O_2
Column		PORAPAQ N (SHIMADZU)	
Carrier gas		Argon (Flowrate: 30 mL min^{-1})	
Injection Temperature (°C)		170	
Detector temperature (°C)		170	
Temperature program	Initial (°C)	50	120
	Ramp rate (°C/min)	2	-
	Final (°C)	120	120
Total analysis time (min)		21	7

Gas analysis was conducted using the procedure below.

a) To make a calibration curve for each gas; a measured gas volume of 300, 500 and 1000 μL was taken from an aluminum bag containing the standard gas using a gas tight micro syringe.

b) Air was analyzed using the above procedure and temperature program presented in Table 3-4.

c) The real volume of each standard gas was calculated using Equation 3-4.

$$\text{Real gas volume } (\mu L) = \text{ Measured volume } (\mu L) - \text{Correction value } (\mu L) \quad [3-4]$$

d) Using aluminum gas sampling bags, 700 µL of SCWG gas sample was taken using a gas tight syringe. Analysis was carried out following the same procedure as a). The gas compositions and ratios were calculated. After the validation of calculations, the gas inside the sampling bag was released. The sampling bag was then vacuumed to be used for next sampling.

e) To evaluate the conversion of oil in SCW, gas yield and efficiency indices were used as defined in Equations 3-5 to 3-7.

Gas yield [mol/ kg biomass]

$$= \frac{\text{mol of gas production [mol]}}{\text{amount of biomass [kg]}} \quad [3-5]$$

Carbon gas efficiency [%]

$$= \frac{\text{mol of carbon atoms in gas product [mol]}}{\text{mol of carbon atoms in the biomass loaded [mol]}} \text{ x } 100 \quad [3-6]$$

Hydrogen gas efficiency [%]

$$= \frac{\text{mol of hydrogen atoms in gas product [mol]}}{\text{mol of hydrogen atoms in the biomass loaded [mol]}} \text{ x } 100 \quad [3-7]$$

3.3.3 Catalyst characterization

Catalyst properties were determined using N_2 gas sorption techniques. The change in catalyst crystal structure was determined by X-ray diffractometer (XRD). To probe the catalyst surface and quantitatively measure the elements on the catalytic surface, scanning electron microscope with energy dispersive spectroscopy (SEM-EDX) was employed. The following section will discuss the procedures for each analytical method.

3.3.3.1. Gas sorption methods

Sections 3.3.3.1.1 and 3.3.3.1.2 will briefly discuss the theories behind BET and BJH method along with the essential equations used to calculate the needed parameters for catalyst characterization.

3.3.3.1.1 BET analysis

This technique was used to measure the specific surface area of the catalyst. This technique was based on the well-known Brunauer, Emmett and Teller (BET)[79] theory which is used to estimate the number of molecules required to cover the adsorbent surface with a monolayer of adsorbed molecules as described in Figure 3-10. Nitrogen is usually employed as the gaseous adsorbate for this analysis. Consequently, standard BET analysis is usually conducted at the boiling temperature of N_2 (-196.15 ℃ or 77 K). The range of validity of this theory is between 0.05 and 0.35 relative pressures. The BET equation is given by Equation 3-8.

$$\frac{1}{v[(P_o/P)-1]} = \frac{c-1}{v_m c}\left(\frac{P}{P_o}\right) + \frac{1}{v_m c} \qquad [3\text{-}8]$$

where: P = equilibrium pressure, P_o = saturation pressure, v = adsorbed gas volume, v_m = monolayer adsorbed gas volume, c = BET constant

The total surface area (S_{total}) and the specific surface area (S_{BET}) are given by:

$$S_{total} = \frac{(v_m N s)}{V} \qquad [3\text{-}9]$$

where: N = Avogadro's number, s = adsorption cross sectional area of the adsorbed species, V = molar volume of the adsorbate gas

$$S_{BET} = \frac{S_{total}}{\alpha} \qquad [3\text{-}10]$$

α = mass of the adsorbent

The pore diameter can be computed from the results of BET analysis. The total amount of N_2 taken up at a pressure of 1 atm and at a temperature of 77 K gives the total pore volume (V_{pore} or v). Using the cylindrical pore model, the total pore volume is;

$$V_{pore} = \frac{1}{4}\pi d^2 L \qquad [3\text{-}11]$$

where: d = mean pore diameter, L = total length of pores

Rearranging equations 3-9 to 3-11, other parameters such as pore diameter and pore length were determined.

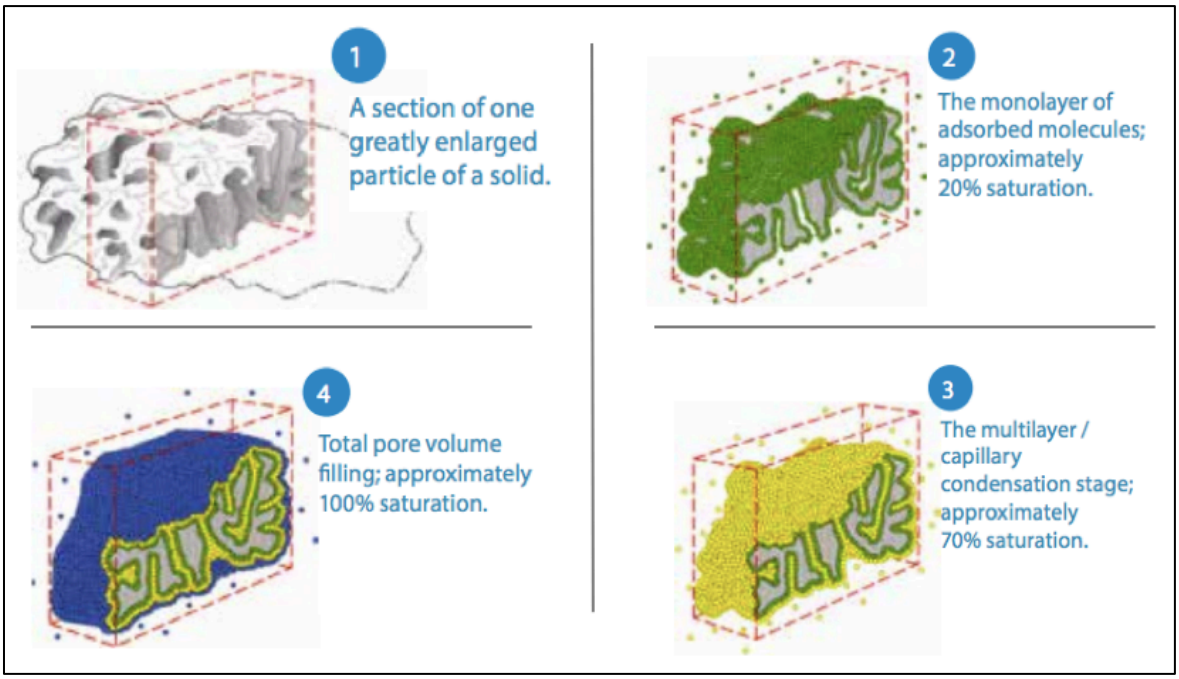

Figure 3-10. The gas sorption process[80].

3.3.3.1.2 BJH analysis

The method developed by Barrett, Joyner, and Halenda is a procedure for calculating pore size distributions from experimental isotherms using the Kelvin model of pore filling. From the isotherms, the number of micro, meso and macropores is determined. This technique is done with the continued addition of gas molecules beyond monolayer formation. This eventually leads to the gradual stacking of multiple layers (or multilayers). The range of validity of this theory is between 0.35 and 0.99 relative pressures. Their formation occurs in parallel to capillary condensation. The latter process is approximated by the Kelvin equation, which quantifies the proportionality between residual (or equilibrium) gas pressure and the size of capillaries capable of condensing gas within them. To investigate the way liquid N_2 is condensed or evaporated during the adsorption and desorption cycles, the pressure at which the liquid will condense in a radius r_k is given by the Kelvin Equation:

$$\ln\left(P/P_o\right) = \frac{-2\gamma V_m \cos\emptyset}{RT\, r_k} \qquad [3\text{-}9]$$

where: r_k = Kelvin radius or critical radius
γ = surface tension of the condensed liquid
$\emptyset$ = equilibrium contact angle
(usually assumed to be 0° due to complete wetting)

Taking into account the statistical film thickness change after each decrement of $^{P}/_{P_o}$, an equation developed by de Boer[79] for the estimation of film thickness is as follows;

$$t\,(\text{Å}) = \left(\frac{13.99}{\log\left(^{P_o}/_{P}\right) + 0.034}\right)^{\frac{1}{2}} \qquad [3\text{-}10]$$

Then, the pore radius is given by;

$$r_p = r_k + t \qquad [3\text{-}11]$$

3.3.3.1.3 Sample preparation and analysis procedure

After each experiment, the catalyst sample was dried for 24 hours under the fume hood. Before each gas sorption analysis, the sample was degassed to completely clean the catalyst surface by flowing an inert gas (N_2) under high vacuum conditions. Table 3-5 presents the conditions for BET and BJH analysis.

Table 3-5. Parameter conditions for BET and BJH analysis.

Parameter		Analysis	
		BET	BJH
Gas sorption system		NOVA 2000e (QUANTACHROME)	
Adsorbate		Liquid N_2	
Adsorbate cross section (Å^2)		16.2	
Outgas time (min)		60	
Outgas temperature (°C)		300	
Isotherms	Adsorption	✓	✓
	Desorption	-	✓
Parameters	Surface Area ($m^2 g^{-1}$)	✓	-
	Particle density (g cm^{-3})	-	✓
	Pore volume (cm^3 g^{-1})	-	✓
	Pore diameter (Å)	-	✓
	Pore length (Å)	-	✓
Approx. total analysis time (min)		80	280

3.3.3.2 XRD analysis

To determine the change in the catalyst crystal structure, X-ray diffractometer (Rigaku Smartlab) was employed. The catalyst was ground first to fine particles to ensure sample uniformity before being subjected to the analysis. The XRD spectra of nickel, aluminum, and molybdenum were acquired using the monochromatic CuKα radiation (λ = 0.154 nm) generated at 40 kV and 130 mA. The diffraction pattern was measured between the 2$\emptyset$ wide angle of 10° - 90° at a scanning speed of 0.2° min^{-1}.

3.3.3.3 SEM-EDX analysis

A scanning electron microscope model, JSM 5600 (JEOL) equipped with energy dispersive X-ray was used to quantitatively analyze the catalyst surface. The main elements being detected are nickel, aluminum, molybdenum and carbon. The acceleration potential used in the analysis was 20 keV. The samples, both in pellet or powdered form were attached on a double-sided adhesive carbon tape and mounted on a silver sample holder. The X-ray peaks generated during scanning were used to identify the elements present on the catalyst surface. Once scanning is finished, elemental mapping was executed to identify the elements generated.

Chapter 4

Decomposition of oil in supercritical water gasification

This chapter presents the results of SCWG experiments using the setup, methods and analytical techniques discussed in Chapter 3. In the first section, the results for the conversion of oil into gaseous products are discussed. It includes the evaluation of the effect of biomass concentration using four different oil concentrations which aimed to determine the optimum oil concentration during SCWG. This discussion is essential in understanding the reactivity of oil in SCW and its tendency towards gaseous product formation. The performance of the process was evaluated according to gas yield and efficiencies introduced in Chapter 3. In the second section, the decomposition products identified in the liquid phase are presented. Liquid phase analysis shows the degree of carbon conversion and the products produced during SCWG of oil. The third section will present the overall carbon mass balance from the results of analysis. A decomposition scheme is also presented which explains the reaction pathway of oil during SCWG. To show the effect of catalyst amount, a fourth section was included. It aimed to compare the process performance and efficiency when catalyst loading is increased and the trend towards gaseous product formation.

4.1 Gas product analysis

To investigate the extent of oil conversion into gaseous products in SCW, gas products were analyzed using GC-TCD. Table 4-1 shows the experiments and their conditions.

Table 4-1. Conditions in the effect of biomass concentration experiment at 400 °C, 25 MPa and 4.5 s residence time.

PARAMETER	Experiment Run			
	SCWG 0.02	SCWG 0.03	SCWG 0.04	SCWG 0.05
Oil fraction (X_{oil})	0.02	0.03	0.04	0.05
H_2O fraction (X_{H2O})	0.98	0.97	0.96	0.95
Oil flowrate, mL min^{-1}	0.50	0.75	0.99	1.25
H_2O flowrate, mL min^{-1}	23.0	23.0	23.0	23.0

Canola oil was first characterized to determine its initial elemental composition. The analysis was carried by Microanalytical Laboratory in The University of Tokyo Graduate School of Science. The oil sample has an elemental composition of 77.51 %C, 11.62 %H and 10.87 %O. Since the sample does not contain nitrogen, the calculation for the ratio of compounds in the gas products excludes nitrogen. Four different oil concentrations were investigated. As presented in Table 4-1, the experiments are denoted as SCWG 0.02, SCWG 0.03, SCWG 0.04, and SCWG 0.05, each representing the oil concentrations used to conduct each test.

Figures 4 – 1 to 4 – 4 present the gas yield and efficiencies obtained from the results of the experiments. From the results, all experimental conditions displayed a similar trend in terms of gas yields and efficiencies. High gas yields and efficiencies could be observed at the start of the reaction. However, as reaction time progressed, gas yields and efficiencies followed a steep decline. By the end of the 300-min gasification time, the percent difference between the initial and final values of these parameters were relatively significant. The percent difference was determined using Equation 4-1 and is presented in Table 4-2.

$$\text{Percent difference} = \frac{\text{Initial}-\text{Final}}{\text{Initial}} \text{ x } 100 \qquad [4\text{-}1]$$

Table 4-2. Percent difference between the initial (T_0) and final (T_{300}) values of gas yield, HGE and CGE.

Experiment Run	Percent difference (%)		
	Overall Gas Yield	HGE	CGE
SCWG 0.02	29.27	32.22	35.23
SCWG 0.03	5.00	24.90	18.54
SCWG 0.04	41.71	38.79	29.44
SCWG 0.05	34.87	50.01	39.50

**Values are based on Figures 4 – 1 to 4 – 4.*

Comparing the initial gas yields, SCWG 0.02 had the greatest yield of 123.6 mol/kg oil which is comparatively higher than the other experimental conditions. The initial gas yields for the 3, 4 and 5% oil concentrations were 81.5, 60.6 and 40.9 mol/kg oil. At the end of the 300-min gasification time, the gas yields of SCWG 0.02, 0.03, 0.04 and 0.05 dropped to 87.4, 77.0, 35.0, and 27.0 mol/kg oil, respectively.

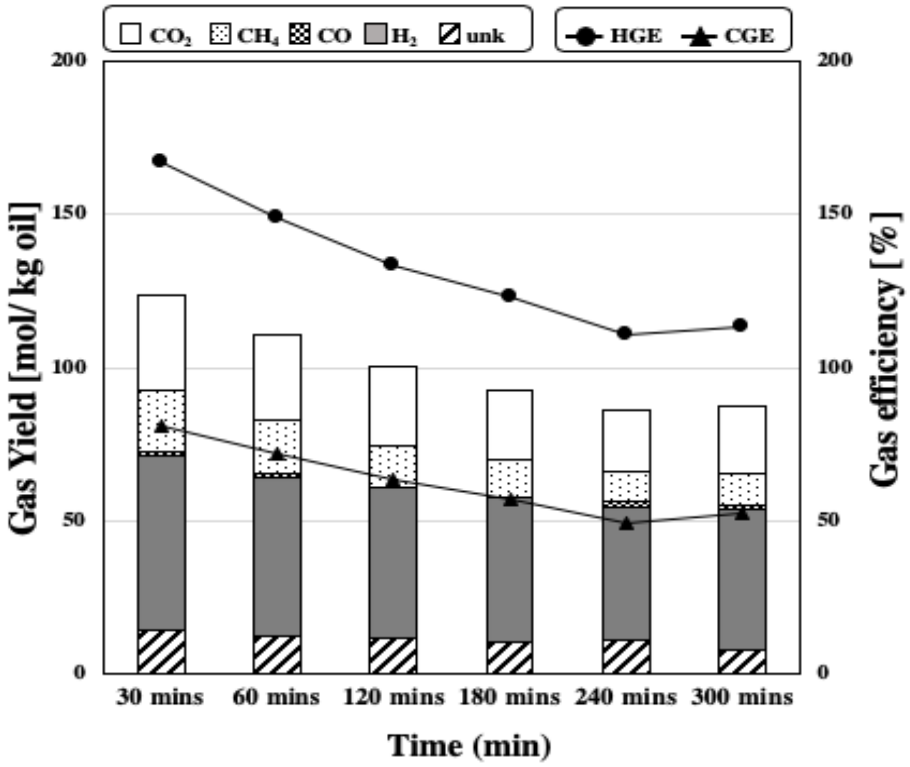

Figure 4-1. Gas yield and efficiency of SCWG 0.02 at 400 ℃, 25 MPa and 4.5 s residence time.

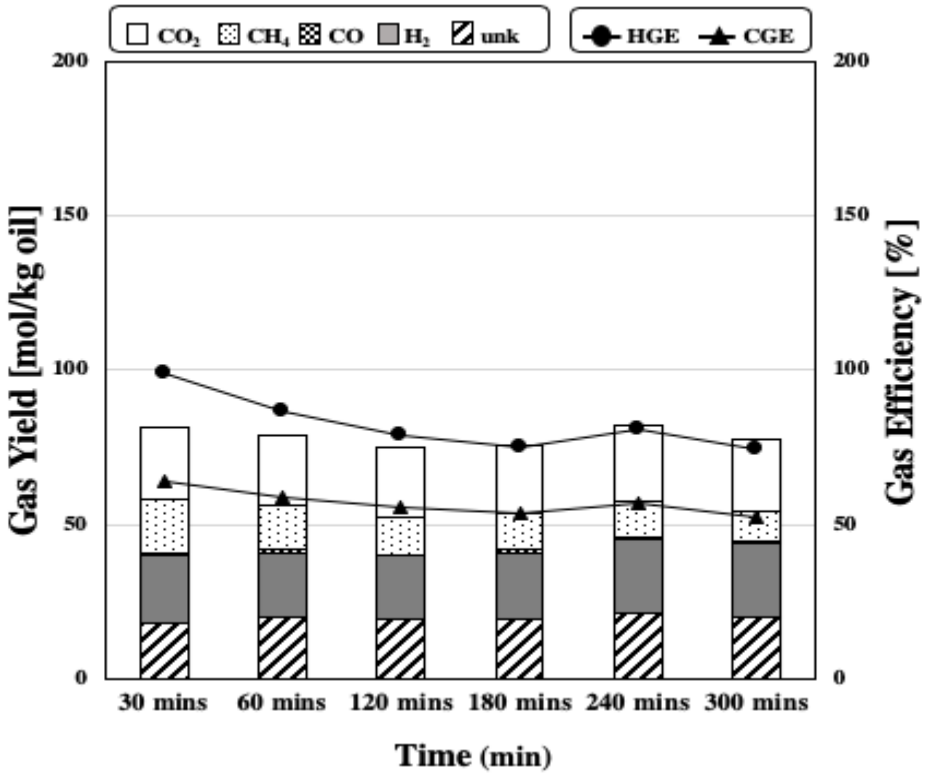

Figure 4-2. Gas yield and efficiency of SCWG 0.03 at 400 ℃, 25 MPa and 4.5 s residence time.

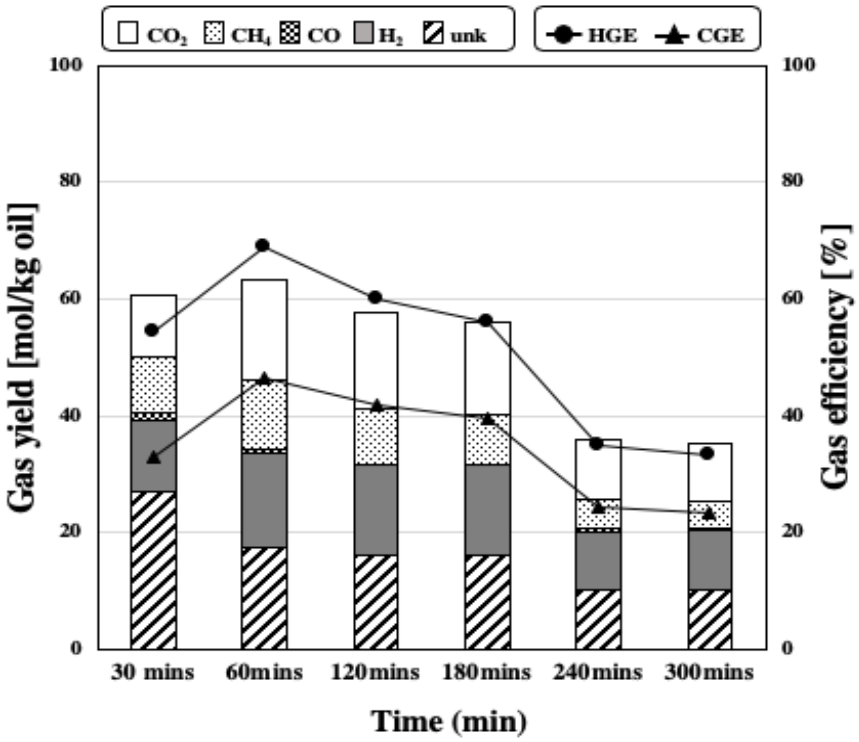

Figure 4-3. Gas yield and efficiency of SCWG0.04 at 400 ℃, 25 MPa and 4.5 s residence time.

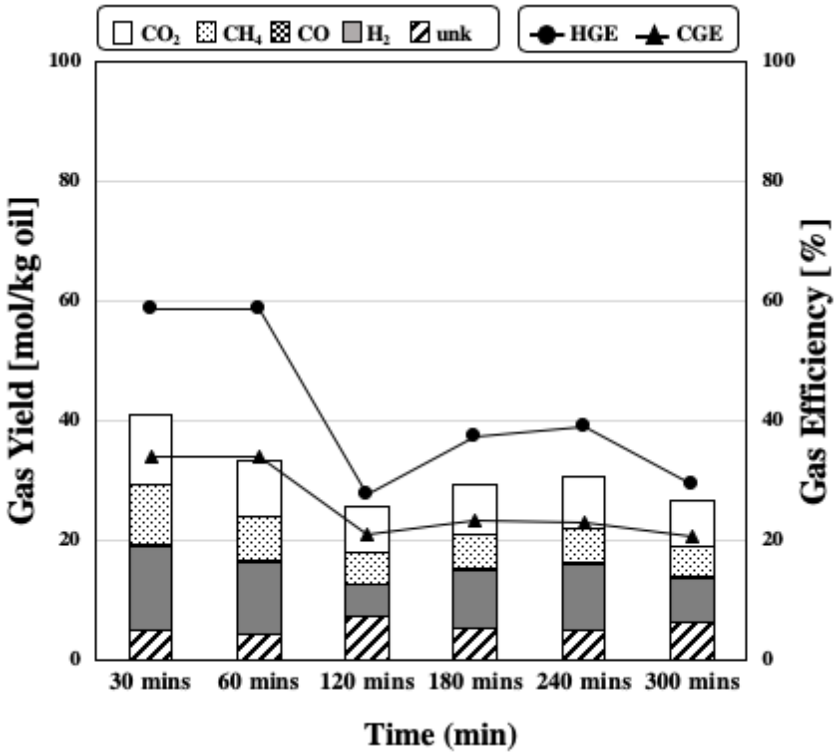

Figure 4-4. Gas yield and efficiency of SCWG0.05 at 400 ℃, 25 MPa and 4.5 s residence time.

The results are tabulated in Table A1. From the results, it was notable that as oil concentration increased, gas yield decreased. As observed, SCWG 0.02 exhibited better performance among the conditions tested. Also, its mean gas yields are high suggesting that the system was able to gasify the biomass well at lower concentrations. In terms of hydrogen gas efficiency, SCWG 0.02 had an initial value of 167.1% which is the highest among other conditions. This value is well above 100% which could either be attributed by the hydrogen present inside the catalyst pores. To check how much H_2 came from the catalyst pores, a blank test was conducted using pure water at 400 ℃, 25 MPa and 10% catalyst amount.

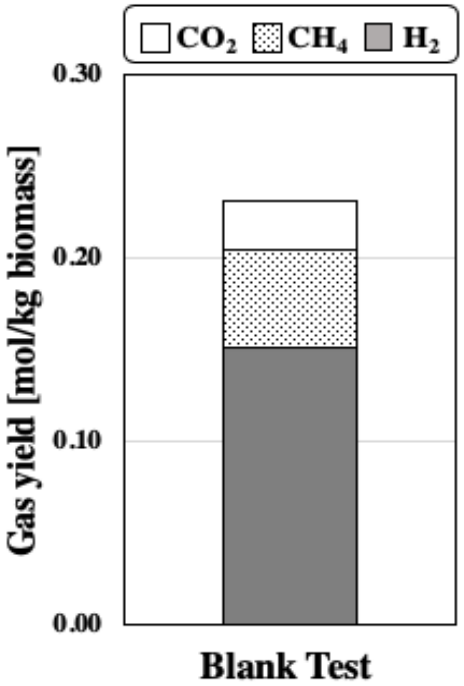

Figure 4-5. Gas yield of blank test using pure water conducted at 400 ℃, 25 MPa.

Figure 4-5 presents the results of blank test using pure water and 10% catalyst amount. The hydrogen gas yield was only 0.15 mol/kg biomass refuting the assumption that the high hydrogen yields were contributed by hydrogen present in the catalyst pores. Instead, hydrogen could have come from water and biomass, comprising 11.62% of total oil composition. As seen in Figure 4–1 to 4– 4, H_2 production selectivity was high at all tested concentrations, whereas CO production was low. This proves the ability of SCW to boost H_2 production with minimal CO production, making it a desirable process in harnessing hydrogen energy. The presence of unknown gas components herein expected to be C_2-C_4 hydrocarbons (C_2H_4, C_2H_6, C_3H_6, C_3H_8, C_4H_8, and C_4H_{10}) were prominent at higher oil

concentrations. This suggest that the cleavage of C-C bonds in longer alkane chains were not efficient, probably due to weak catalytic performance of the system. In terms of its hydrocarbon selectivity, CH_4 production was favored. However, as oil concentration increase, H_2 production was significantly low and hydrocarbon gas selectivity increased in favor of the unknown (C_2-C_4) gases with corresponding decrease in CH_4 selectivity.

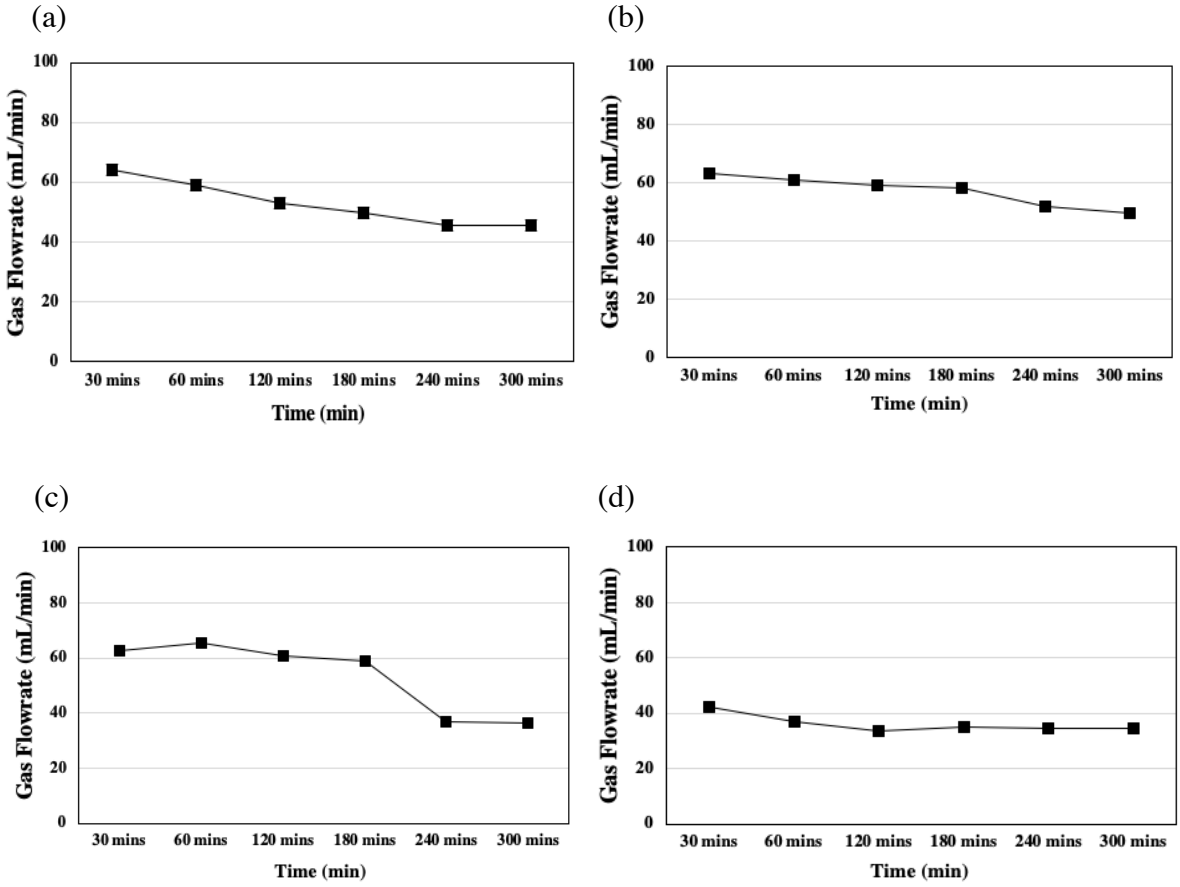

Figure 4-6. Gas flowrates of (a) SCWG 0.02, (b) SCWG 0.03, (c) SCWG 0.04, and (d) SCWG 0.05.

The gas flowrate of each experiment was plotted in Figure 4-6. For 2% and 4% oil concentration, gas flowrate had a significant decrease whereas 3% and 5% oil concentration had a slight decrease. This observation is based on the initial and final flowrate measured before and after gas sampling.

4.2 Liquid phase analysis

4.2.1 TOC analysis

TOC analysis was conducted to determine the amount of carbon present in the liquid phase. From Figure 4-7, the amount of carbon in liquid phase increases as gasification time increases. The percentage difference between the initial and final amount of carbon present in the liquid phase were 50.1%, 85.93%, 50.1%, and 63.8% for SCWG 0.02, 0.03, 0.04 and 0.05, respectively. These were calculated using Equation 4-2.

$$\text{Percent difference} = \frac{\text{TOC}_{\text{final}} - \text{TOC}_{\text{initial}}}{\text{TOC}_{\text{final}}} \text{ x } 100 \qquad [4\text{-}2]$$

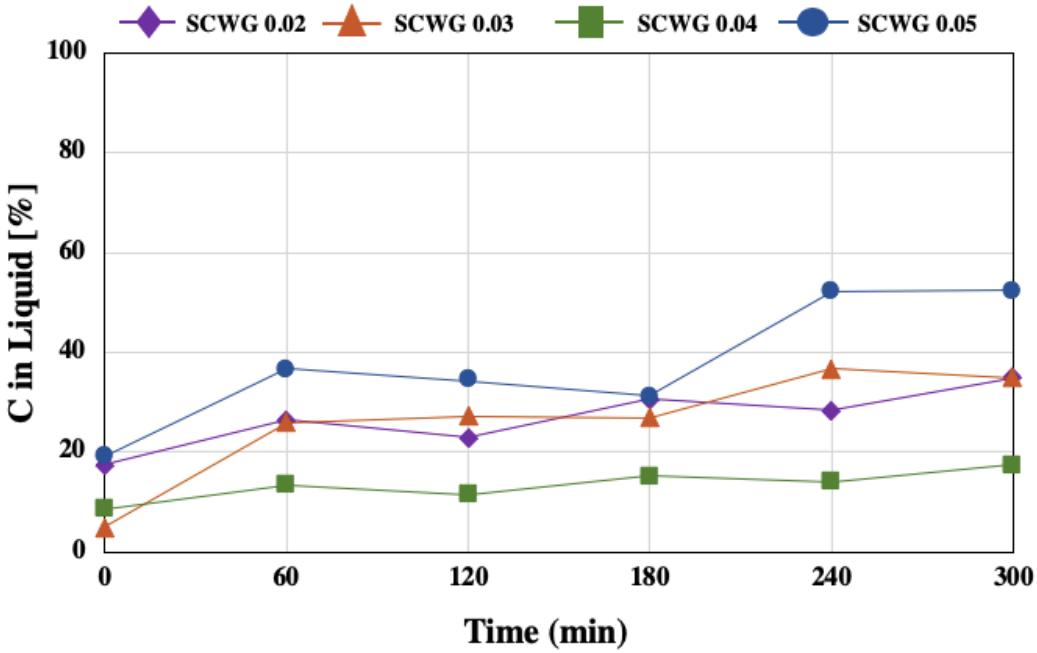

Figure 4-7. Carbon in effluent after 300-min gasification time.

SCWG0.02: TOC0 = 17.4% to TOC300 = 34.9%

SCWG0.03: TOC0 = 3.92% to TOC300 = 35.0%

SCWG0.04: TOC0 = 8.74% to TOC300 = 17.5%

SCWG0.05: TOC0 = 19.0% to TOC300 = 52.5%

This increase in TOC suggests that organics were continuously produced in the system, possibly due to the decline of catalyst performance. SCWG 0.05 had higher TOC amount compared with other experiments. Given that it has higher initial carbon content, the amount of its TOC is comparatively higher. SCWG 0.02 and 0.03 had relatively the same TOC conversion trend. Meanwhile, SCWG 0.04 had the lowest TOC conversion implying that less carbon was converted into liquid.

4.2.2 GC-MS Analysis

Liquid samples were dissolved in hexane or acetonitrile. Figure 4-8 shows the GC/MS chromatogram of pure canola oil. The liquid samples analyzed were taken after 30-min gasification. Table 4-3 tabulates the detected peaks. The identification of compounds was performed by comparing their mass spectra with data from US National Institute of Standards and Technology (NIST, USA).

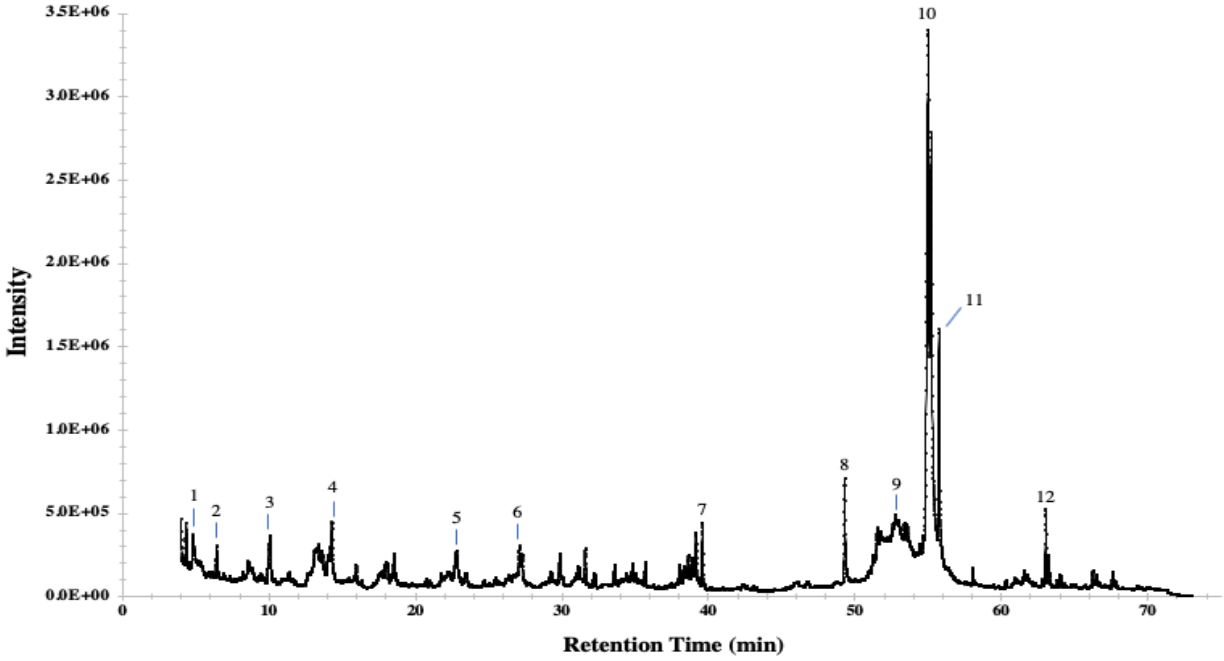

Figure 4-8. Pure canola oil dissolved in hexane at 50% v/v.

Oven temperature: 45°C (2 min hold) raised at 4°C/min to 280°C (10 min hold).

Table 4-3. The compounds present in pure canola oil.

Peak	Compound	Common Names	Chemical Formula	Similarity (%)
1	Hexanoic Acid	Caproic Acid	C6H12O2	88
2	Hexanoic Acid	Caproic Acid	C6H12O2	91
3	Pentanoic Acid	Valeric Acid	C5H10O2	86
4	Octanoic Acid	Caprylic Acid	C8H16O2	87
5	Tetradecanoic Acid	Myristic Acid	C14H28O2	86
6	Dodecanoic Acid	Lauric Acid	C12H24O2	80
7	Hexadecane	-	C16H34	94
8	n-Hexadecanoic Acid	Palmitic Acid	C16H32O2	87
9	9,12-Octadecadienoic Acid	Linoleic Acid	C18H32O2	92
10	Oleic Acid	-	C18H34O2	95
11	Octadecanoic Acid	Stearic Acid	C18H36O2	92
12	9-Octadecenoic Acid	Oleic Acid	C18H32O2	85

Taking the samples from 2% and 5% oil concentration which represents the lower and upper concentrations being investigated, the liquid product samples from SCWG 0.02 and 0.05 were analyzed. Figures 4-9 and 4-10 show the chromatogram, with their corresponding peak information tabulated in Tables 4-4 and 4-5.

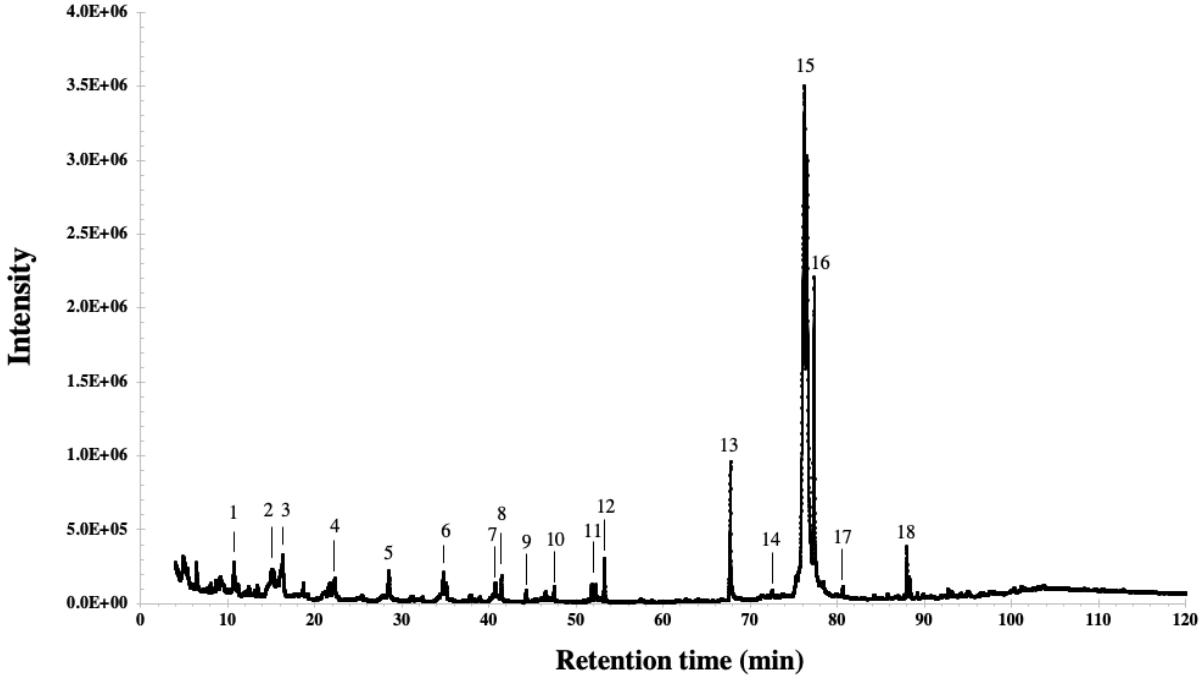

Figure 4-9. GC-MS chromatogram for SCWG0.02 liquid sample after 30 mins gasification time.

Table 4-4. Result of GC-MS analysis for SCWG0.02 liquid sample.

Peak	Compound	Common Names	Chemical Formula	Similarity (%)
1	Hexanoic Acid	Caproic Acid	C6H12O2	91
2	1-Octanol, 2-butyl-	-	C12H26O	88
3	Heptanoic Acid	Enanthic Acid	C7H14O2	81
4	Octanoic Acid	Caprylic Acid	C8H16O2	87
5	Nonanoic Acid	Pelargonic Acid	C9H18O2	84
6	Tetradecanoic Acid	Myristic Acid	C14H28O2	87
7	Dodecanoic Acid	Lauric Acid	C12H24O2	78
8	n-Hexadecanoic Acid	Palmitic Acid	C16H32O2	94
9	Octane, 2-cyclohexyl-	-	C14H28	84
10	Hexadecane	-	C16H34	94
11	1-Hexadecene	Cetene	C16H32	84
12	Hexadecane	-	C16H34	95
13	n-Hexadecanoic Acid	Palmitic Acid	C16H32O2	90
14	9,12-Octadecadienoic Acid	Linoleic Acid	C18H32O2	81
15	Oleic Acid	-	C18H34O2	96
16	Octadecanoic Acid	Stearic Acid	C18H36O2	92
17	n-Hexadecanoic Acid	Palmitic Acid	C16H32O2	81
18	9-Octadecenoic Acid	Oleic Acid	C18H32O2	85

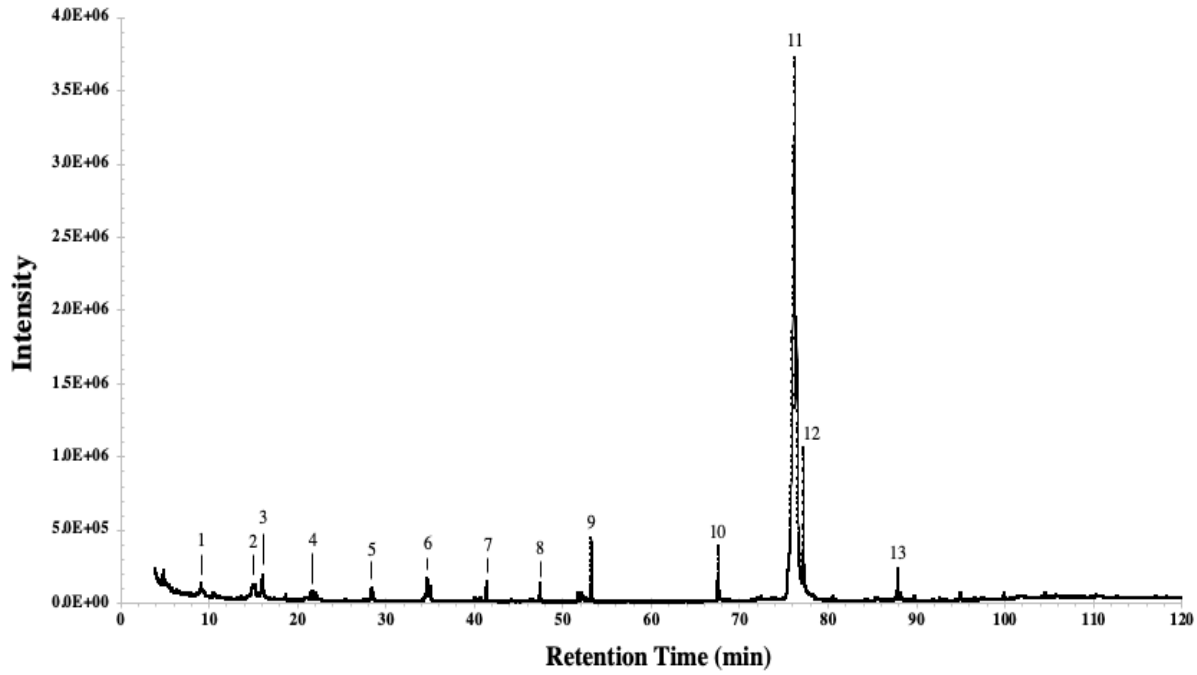

Figure 4-10. GC-MS chromatogram for SCWG0.05 liquid sample after 30 mins gasification time.

Table 4-5. Result of GC-MS analysis for SCWG0.05 liquid sample.

Peak	Compound	Common Names	Chemical Formula	Similarity (%)
1	Decane	-	C10H22	85
2	Isooctane, (ethenyloxy)-	-	C10H20O	86
3	n-Decanoic Acid	Capric Acid	C10H20O2	84
4	Formic acid, 2-methylpropyl ester	-	C5H10O2	76
5	Propanoic acid, propyl ester	-	C6H12O2	79
6	Tetradecanoic Acid	Capric Acid	C14H28O2	85
7	Acetaldehyde	-	C2H4O	82
8	Acetaldehyde	-	C2H4O	78
9	Acetaldehyde	-	C2H4O	83
10	Heptadecanoic Acid	Marganic Acid	C17H34O2	74
11	Oleic Acid	-	C18H32O2	95
12	Octadecanoic Acid	Stearic Acid	C18H36O2	85
13	9-Octadecenoic Acid	Oleic Acid	C18H32O2	90

From Figure 4-9 and Table 4-4 at 2% oil concentration, the presence of smaller molecular fatty acids was detected as higher molecular fatty acids decomposed. This suggests that oleic acid may have undergone decarbonylation and decarboxylation to shorter chain FAs and aliphatic compounds. At 5% oil concentration, lower molecular weight fatty acids were not noticeable; instead, the presence of aldehydes were mainly detected. This suggests that possible reaction pathways such as epoxidation of canola oil [81] may have

happened. Epoxidation of vegetable oils with molecular oxygen leads to the degradation of the oil to smaller compounds, such as aldehydes and ketones, as well as short-chain dicarboxylic acids.

4.2.3 HPLC results

To quantify the amount of fatty acids present in the sample, mixtures of standard fatty acids were analyzed at different concentrations (0.50, 0.25, 0.10, and 0.05 g-C/L) to establish a calibration curve for each fatty acid. Table 4-6 presents the retention times along with the detected peak area for each concentration.

Table 4-6. Average retention time and calibration data for fatty acid standards.

Fatty Acid	**Ave. Retention Time (min)**	**Chromatogram Area at each concentration**			
		0.50 g-C/L	0.25 g-C/L	0.10 g-C/L	0.05 g-C/L
Oleic (C18:1)	6.587	247975	126575	49573	25016
Linoleic (C18:2)	5.675	1792086	897580	359789	25016
Linolenic(C18:3)	5.097	2230464	1122179	436346	215989
Palmitic (C16:0)	6.658	22985	9080	3716	-
Stearic (C18:0)	8.085	16619	7360	3113	-

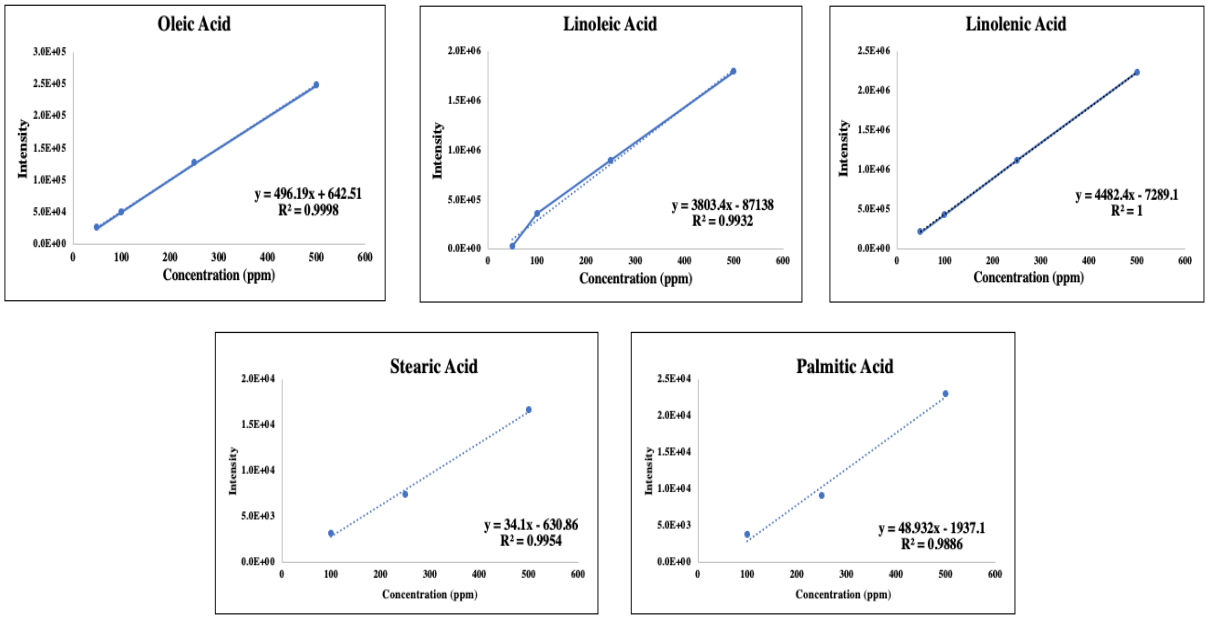

Figure 4-11. Calibration curves of prepared fatty acid standards.

Table 4-7. Fatty acid concentration detected in SCWG samples.

Experiment Run	Time (min)	Fatty acid concentration (g-C/L)				
		Oleic (C18:1)	Linoleic (C18:2)	Linolenic (C18:3)	Palmitic (C16:0)	Stearic (C18:0)
SCWG 0.02	30	1.70	0.24	0.05	-	-
	60	2.18	0.33	0.06	-	-
	120	2.62	0.39	0.06	-	-
	180	3.34	0.52	0.06	-	-
	240	1.57	0.24	0.05	-	-
	300	2.33	0.35	-	-	-
SCWG 0.05	30	4.93	0.95	0.32	-	-
	60	4.85	1.06	0.31	-	-
	120	5.52	1.22	0.40	-	-
	180	5.67	1.24	0.39	-	-
	240	5.63	1.23	0.39	-	-
	300	5.13	1.15	0.36	-	-

The main problem encountered for the determination of the fatty acid composition of the SCWG samples was not so much the chromatographic separation but the detection of the underivated free fatty acids. Since the fatty acids and samples tested did not underwent preliminary derivatization with chromophores or fluorescent dyes, the UV radiation was barely absorbed by saturated fatty acids (palmitic and stearic) and they could only be detected at higher concentrations (>50 ppm). At wavelength of 208 nm, the C=C could be detected, thus, quantification of unsaturated fatty acids (oleic, linoleic, and linolenic acids) was possible. The original TOC values of SCWG 0.02 and 0.05 samples are 15.5 g-C/L and 38.6 g-C/L, respectively. For SCWG 0.02, the carbon gas efficiency (CGE) during the first 60 mins of the experiment was more than 70%, suggesting that 30% were present in liquid phase. For SCWG 0.05, the CGE during the first 60 min was only around 34%, suggesting that 66% were present in liquid phase. From HPLC analysis, saturated FA such as palmitic and stearic acid were not detected in the samples. It is possible that the amount of palmitic and stearic acids was too low to be detected. One possible reason is that oleic acid, a mono-unsaturated fatty acid, decomposed into stearic acid which in turn decomposed into heptadecane (C17). Canola oil is typically composed of 92% unsaturated and 8% saturated fatty acids. Unsaturated FAs include oleic (56%), linoleic (26%), and linolenic (10%) acids. Saturated FAs include palmitic (4%) and stearic (2%) acids. From literature[82], oleic acid which comprises canola oil in higher quantity can decompose via C-C bond cleavage, decarbonylation and decarboxylation to shorter chain FAs and aliphatic hydrocarbons. This decomposition scheme is presented in Figure 4-13. If hydrogen is present, the unsaturated oleic acid can also hydrogenate to the saturated stearic acid. The short chain FA and

saturated FA both decompose through decarboxylation and decarbonylation to aliphatic hydrocarbons. However, in this research, since Canola oil is not a pure compound, the

Table 4-8. Summary of the amount of carbon quantified.

Experiment Run	Time (min)	TOCliq (mol)	Fatty acid (mol C)						% unaccounted carbon
			Oleic (C18:1)	Linoleic (C18:2)	Linolenic (C18:3)	Palmitic (C16:0)	Stearic (C18:0)	ΣC (mol)	
SCWG 0.02	30	0.005	2.49.E-03	3.54.E-04	7.04E-05	-	-	0.003	43.6
	60	0.008	3.21.E-03	4.88.E-04	8.23E-05	-	-	0.004	51.9
	120	0.007	3.85.E-03	5.80.E-04	8.66E-05	-	-	0.005	33.8
	180	0.009	4.91.E-03	7.69.E-04	8.22E-05	-	-	0.006	36.6
	240	0.008	2.31.E-03	3.56.E-04	6.77E-05	-	-	0.003	67.5
	300	0.010	3.42.E-03	5.16.E-04	-	-	-	0.004	62.1
SCWG 0.05	30	0.011	7.24.E-03	1.41.E-03	4.81.E-04	-	-	0.009	15.7
	60	0.027	7.12.E-03	1.57.E-03	4.66.E-04	-	-	0.009	66.4
	120	0.026	8.11.E-03	1.80.E-03	5.93.E-04	-	-	0.011	58.8
	180	0.023	8.33.E-03	1.83.E-03	5.80.E-04	-	-	0.011	53.7
	240	0.039	8.27.E-03	1.81.E-03	5.76.E-04	-	-	0.011	72.5
	300	0.039	7.54.E-03	1.70.E-03	5.29.E-04	-	-	0.010	74.9

difficulty of tracing its decomposition pathway was evident. I could only speculate its decomposition pathway by treating its main fatty acid components as separate entities, which in this case becomes a challenge because of great product variation at each decomposition stage. Take the case for oleic acid decomposition as an example. From Figure 4-13, it is said that oleic acid hydrogenates into stearic acid in the presence of H_2. Quantifying the amount of oleic acid before and after the reaction could give us an idea how much oleic acid was being converted to stearic acid. Same quantification method applies with stearic acid. However, at the start of the reaction, unsaturated FAs such as linoleic acid and linolenic acid were present wherein after the reaction could possibly be hydrogenated into oleic acid, making the final quantification of oleic acid a challenge. Therefore, if the goal is to follow the exact decomposition pathway, using a model compound could give us a clearer results and overview of the process.

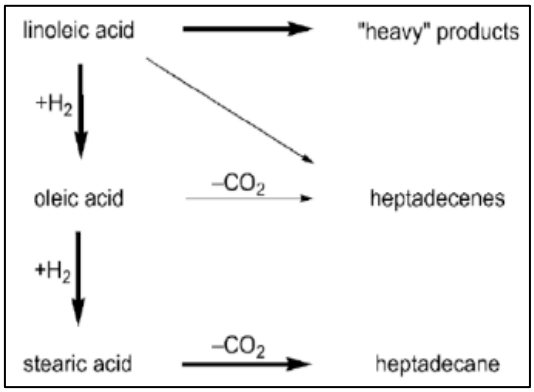

Figure 4-12. Hydrothermal catalytic reaction pathways for C18 fatty acids[82].

4.3 Overall carbon balance

To determine the proportion of product distribution, the overall carbon balance is plotted. Figures 4-13 to 4-16 present the carbon balance of SCWG 0.02, 0.03, 0.04, and 0.05 gasification experiments.

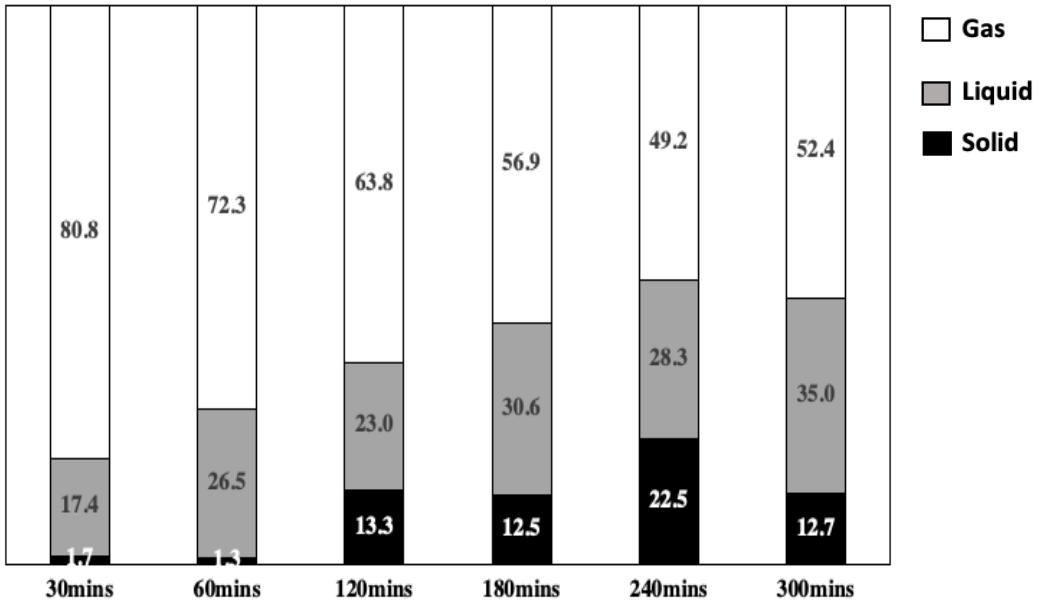

Figure 4-13. Carbon balance for SCWG 0.02.

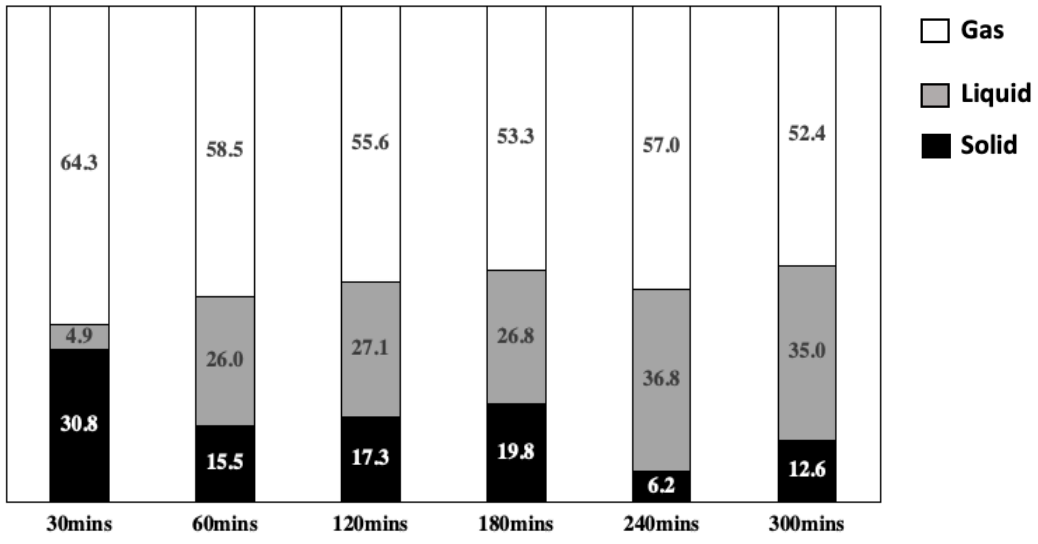

Figure 4-14. Carbon balance for SCWG 0.03.

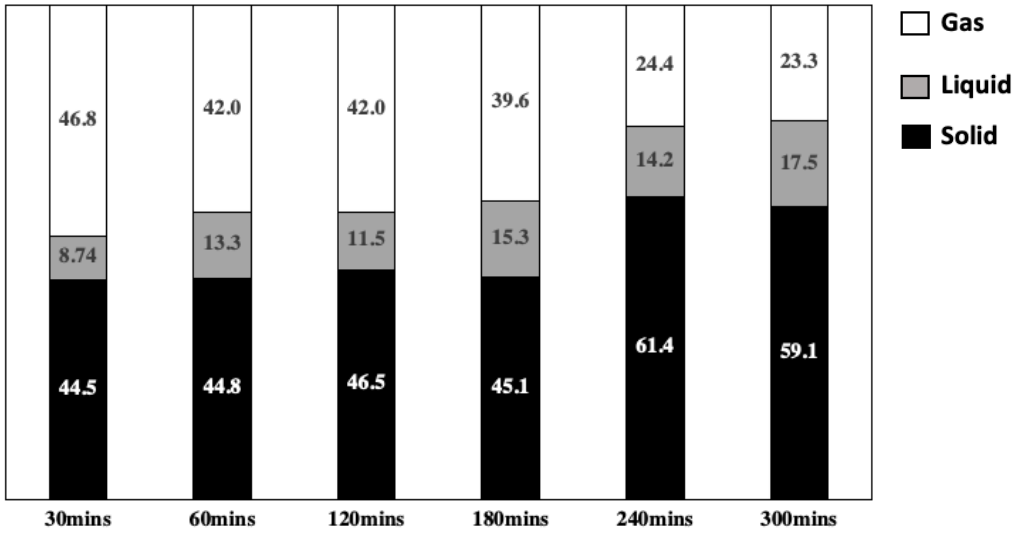

Figure 4-15. Carbon balance for SCWG 0.04.

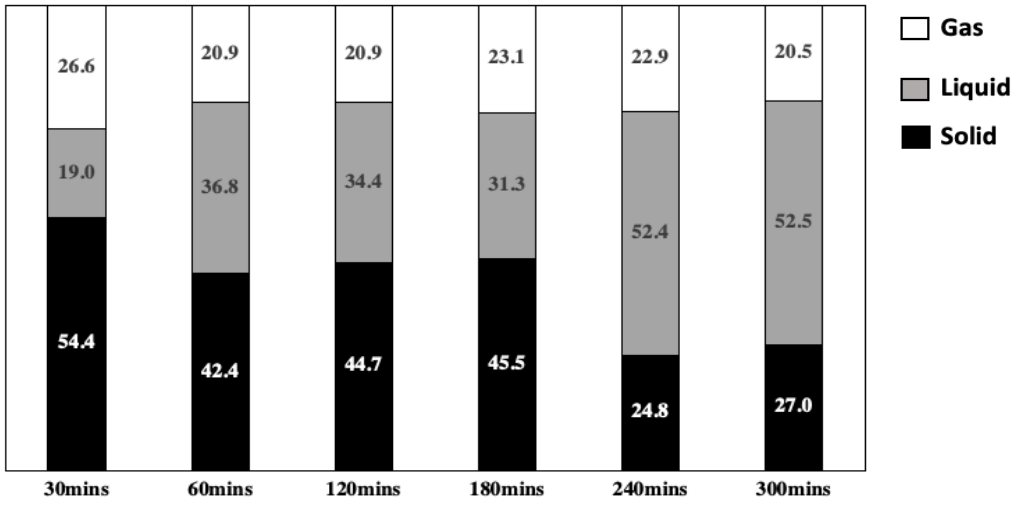

Figure 4-16. Carbon balance for SCWG 0.05.

For SCWG 0.02, the proportion of gas products was higher than liquid and solid. Most notable is the higher gas proportion obtained during the first 30 mins of the experiment. This shows that the system was able to convert the biomass into desirable gas products. The solid proportion was obtained by overall balance. As seen from Figure 4-14, as reaction time progressed, the amount of solids increased suggesting the formation of organics such as char and tar. This is an indication of declining system efficiency signifying the inability of the system to gasify the biomass into gas products. In Figure 4-15, the gas proportions were

high throughout the gasification time. However, in the first part of the reaction around 30 min, the solids proportion was high. This was also observed for SCWG 0.04 and 0.05. During the experiment with higher oil concentration, a whitish emulsion was observed coming out from the system. This emulsion did not mix with the liquid product, thus could represent the proportion of solids in the carbon balance scheme.

4.4 Effect of catalyst amount

To determine the effect of varying the amount of catalyst on the SCWG process, an experiment was added using 20% catalyst amount (i.e. 18.2 g). The experiments with 10% and 20% catalyst amount were conducted for 180 mins to see the difference in their gas yields and efficiencies. Comparing Figure 4-18 and 4-21, using 20% catalyst amount is better than using 10% catalyst amount in terms of gas yields and efficiencies. These results are already expected if the amount of catalyst is to be increased. Figure 4-19 presents the change in gas flowrate during SCWG 0.02 at 10% catalyst amount. As gasification time progressed, the flowrate of gas products became slower, thus a decreasing trend for gas volume is also expected.

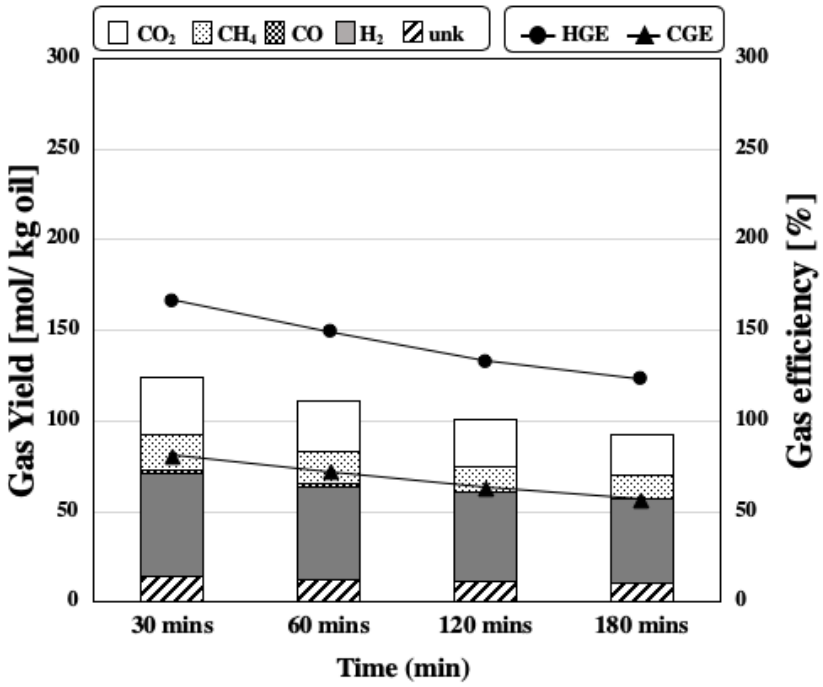

Figure 4-17. SCWG 0.02 at 10% catalyst loading, 400 °C, 25 MPa and 180 min gasification time.

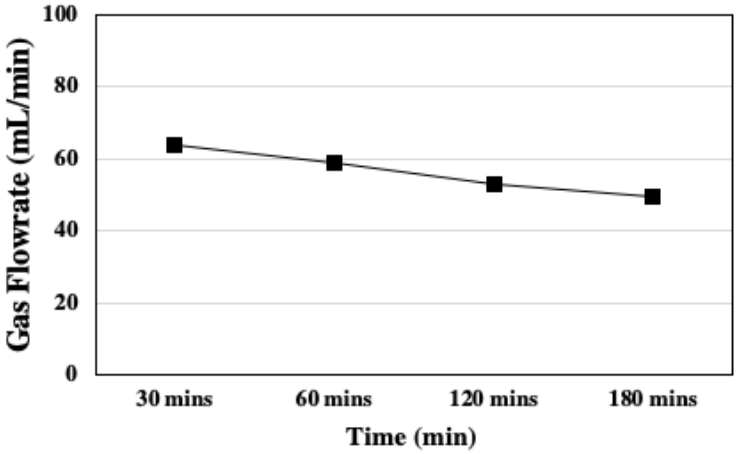

Figure 4-18. Gas flowrate of SCWG 0.02 at 10% catalyst amount.

The performance of the process loaded with 20% catalyst amount is compared with the data obtained for the 10% catalyst loading. As compared with Figure 4-18, the performance of this process is better in terms of gas yields and efficiencies, wherein deactivation is not evident. Instead, it could be seen that there was an enhancement in H_2 yield by the end of the 180-min gasification time. A slight increase in gas efficiency was also observed. In Figure 4-20, the gas flowrate is stable during the first 120 mins of the reaction and increased slightly towards the end of the gasification period. This implies that catalyst deactivation

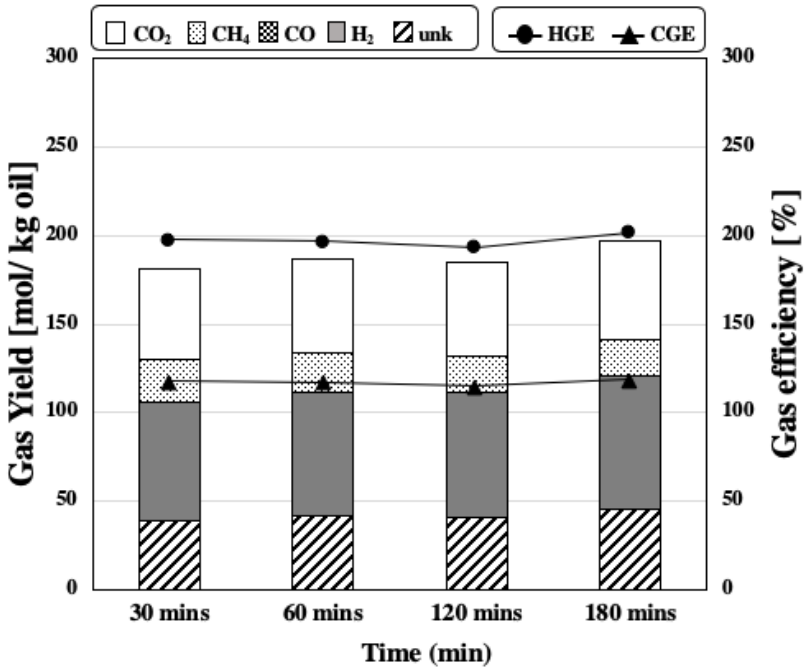

Figure 4-19. SCWG 0.02 at 20% catalyst loading, 400 °C, 25 MPa and 180 min gasification time.

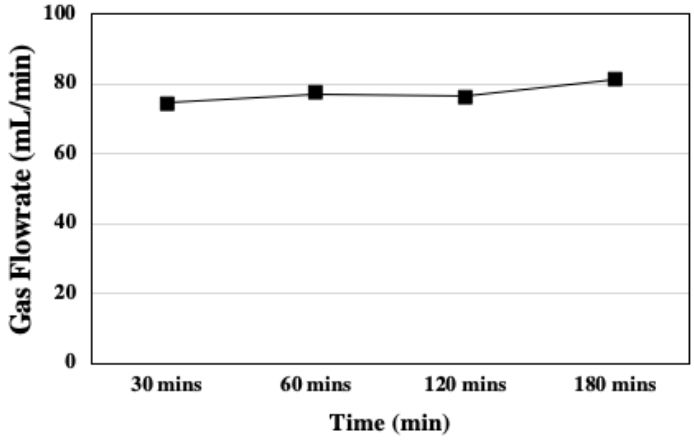

Figure 4-20. Gas flowrate of SCWG 0.02 at 20% catalyst amount.

was not yet evident within the 300-min gasification period. If the trend is carefully examined, the fact that the initial performance parameters (e.g. gas yield, efficiencies, flowrate and volume) were gradually increasing indicates that the rate of decomposition of reactants on the catalytic bed was not uniform.

In terms of gas products, the proportion of H_2 was high in both cases. In 10% catalyst amount, the gas yields and efficiencies were decreasing in contrast to the 20% catalyst amount wherein these parameters maintained an almost constant value and slightly increasing at the end of the 180 min gasification time. This suggests that the degree of catalyst deactivation was not so evident if the amount of catalyst was increased. From the acquired data, it can be concluded that increasing the amount of catalyst loading enhances and maintains the high gas yields and efficiencies of the process in reference to its initial performance. However, since the decline of catalyst performance is inevitable, extending the gasification time up to several more hours could give a predicted trend of decreasing gas yields and efficiencies. Also, it is to be noted that in 20% catalyst loading, the amount of the unknown gases suspected to be C_2-C_4 hydrocarbons increased. Since the target of this process is a greater H_2 yield, having C_2-C_4 hydrocarbons in the product gases may not be desirable in parallel with our research interests. Furthermore, in terms of economic viability, lower catalyst amount but having greater desired product yields and efficiencies is favorable. In this case, using 10% catalyst amount is deemed favorable in terms of economic viability. The performance of the process without using catalyst was also investigated. A non-catalytic SCWG 0.02 experiment was performed and Figure 4-24 presents the gas yields and efficiencies of the process.

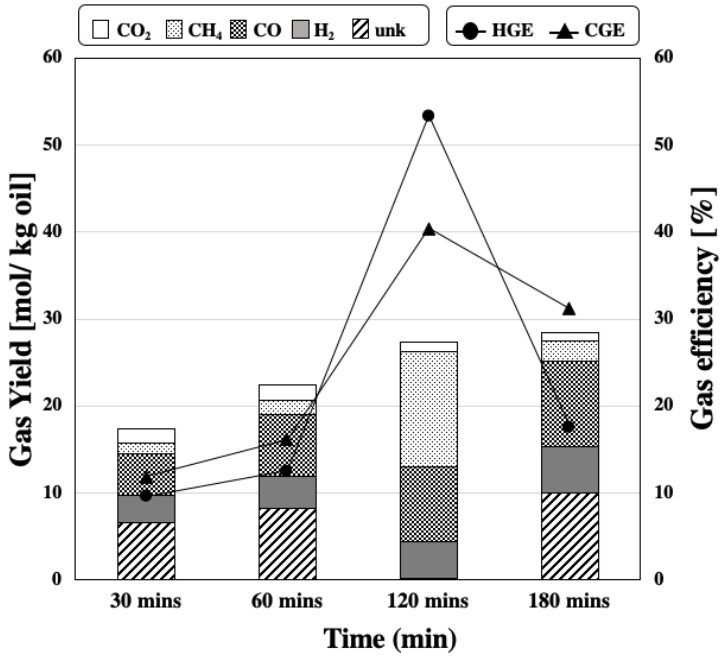

Figure 4-21. SCWG 0.02 without catalyst, 400 ℃, 25 MPa and 180 min gasification time.

The performance of the non-catalytic experiment was inferior compared with that of the catalytic SCWG. First, as indicated in Figure 4-21, the C_2-C_4 unknown gas products occupied a significant amount in the gas product distribution. This indicates that the system was not able to convert the larger alkanes into desired products. This is contrary to the results obtained for the catalytic SCWG process, wherein C_2-C_4 hydrocarbons did not exceed beyond 30% of the overall product gases. Another notable difference is the low amount of H_2 and CO_2 production in contrast with higher CO production. Hydrogen and carbon dioxide are mainly produced during the water-gas shift reaction [Equation 1-1 to 1-2] at the expense of CO. The fact that the process hardly produced H_2 means that the water-gas shift reaction was not executed to its full extent. The production of CH_4 was also hardly noticeable and the selectivity of the process towards CH_4 was very low. Since steam reforming is a stepwise process with methanation being the last step, it was evident that the whole reforming process did not reach this step during the first 60 minutes of the reaction. After 120 minutes, the amount of CH_4 dramatically increased with the amount of H_2 and CO_2 at a steady production rate. This could have been caused by experimental (or analytical) error committed during the conduct of the experiment. By the end of 180 minutes gasification, the yields and efficiencies dropped, and this time the production of C_2-C_4 hydrocarbons increased again, following the decrease of CH_4.

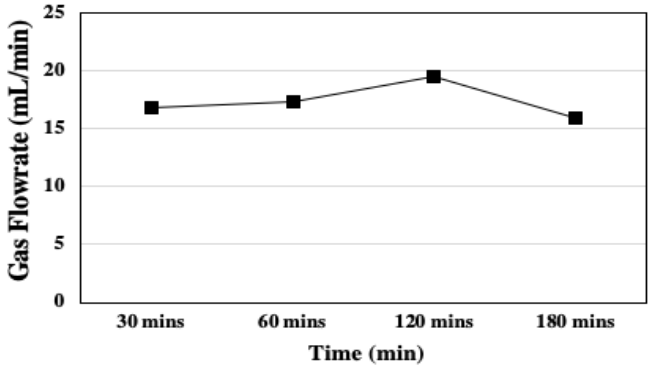

Figure 4-22. Gas flowrate of SCWG 0.02 without catalyst.

The gas flowrate of the non-catalytic SCWG 0.02 is presented in Figure 4-22. The gas flowrates were almost 2 – 3 times less compared with the catalytic processes. Comparing the results of these experiments, it can be concluded that using a catalyst during the SCWG of oil enhances the performance parameters such as gas yields and efficiencies. Moreover, the selectivity of desired gas products was better in catalytic processes. In terms of economic efficiency, incorporating a catalyst into the process gives viable economic results, given that the process proceeds in favor with the production of desired gas products.

Chapter 5
Characterization of nickel catalyst

In Chapter 4, the biomass concentration could clearly show catalyst deactivation. Among the experiments, the performance of lower biomass concentrations (SCWG 0.02 and 0.03) in terms of gas yields and efficiencies were better compared with experiments performed at higher biomass concentrations (SCWG 0.04 and 0.05). Using these findings, additional experiments and analysis were added in order to find out what causes the catalyst to lose its catalytic efficiency. This chapter is divided into three parts. The first part presents the characterization results obtained for the unspent catalyst. This data will be used to compare and describe the changes that occurred after the catalyst was streamed in SCW and used in experiments. The second part presents the catalyst characterization results of the catalysts obtained after each experiment described in Chapter 4. The third part presents the experiments using uniform concentration with varying reaction time to determine the deactivation behavior of the catalyst.

5.1 Initial catalyst characterization

Figure 5-1 shows the image of the unspent catalyst used before the reaction. The catalyst is an alloy of 67.2% Ni, 31.9% Al, and 0.9% Mo, based on manufacturer's data. It was subjected to BET and BJH analysis to characterize its physical properties. Using the BET analysis, the relationship between the catalyst surface area and pressure exerted by the absorbed gas can be determined. The unspent catalyst had an average surface area of 58.2 m^2/g.

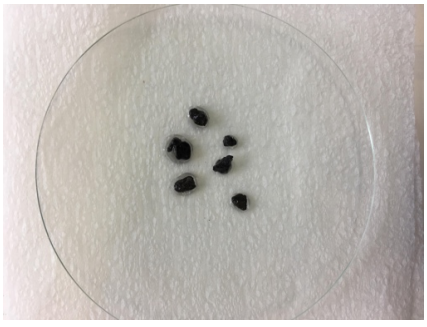

Figure 5-1. The unspent wet catalyst.

Table 5-1. BET surface area result of unspent catalyst.

Sample weight, g	0.688
Outgas time, min	60
Outgas temperature, °C	300
Analysis Gas	Nitrogen
Analysis time, min	81.8
Surface Area, m^2/g	58.2

After BET analysis, the catalyst sample was then subjected to BJH analysis. This is also known as capillary condensation wherein adsorbate pressures were increased between 0.35 and 0.99 relative pressures. Table 5-2 presents the results of BJH analysis.

Table 5-2. BJH analysis results for the unspent catalyst.

Sample weight, g	0.26	Particle density, g cm^{-3}	5.23
Sample volume, cm^3	0.09	Void Fraction	0.73
Outgas time, min	60	Pore Volume, cm^3 g^{-1}	
Outgas temperature, °C	300	Total	0.05
Adsorbate		Micropore	0.02
Analysis Gas	Nitrogen	Mesopore	0.03
Cross Section, $Å^2$	16.2	Pore diameter, Å	48.6
Analysis time, min	261	Pore length, Å	8.10

The catalyst has a true density of 6.94 g/cm^3. This density excludes the volume of any open and closed pores. It was calculated using Equation 5-1.

$$\text{True density} = \rho_{Ni}X_{Ni} + \rho_{Al}X_{Al} + \rho_{Mo}X_{Mo} \quad [5\text{-}1]$$

where; ρ_{Ni} = density of nickel (g cm^{-3})

ρ_{Al} = density of aluminum (g cm^{-3})

ρ_{Mo} = density of molybdenum (g cm^{-3})

X_{Ni} = weight fraction of nickel

X_{Al} = weight fraction of aluminum

X_{Mo} = weight fraction of molybdenum

The unspent catalyst has a bulk density of 1.44 g/cm^3 which was measured by using a graduated cylinder. This density comprises the interparticle voids, the volume of the catalyst including the open and closed pores. The volume of interparticle voids can change with packing, leading to the concept of 'tap density'. This is done by measuring a sample volume and then making a compact particle packing by tapping the holding vessel. The particle density was also calculated to be 5.23 g/cm^3. This density differs from the bed density as it is not dependent on the degree of compaction of the solid. Another important parameter is the void fraction. This void fraction estimates the available 'void space' that is accessible for reaction to occur. The pore volume was estimated to be 0.05 cm^3/g. From this, the micro and meso pore volumes were also determined to be 0.02 and 0.03 cm^3/g, respectively. The pore volumes were categorized according to pore type – micropores (< 20 Å), mesopores (20 - 500 Å) and macropores (> 500 Å).

After all pores are completely filled with the adsorbate gas, the adsorption process is reversed by withdrawing known amounts of gas from the system in steps, by which one generates desorption isotherms. The resulting hysteresis leads to isotherm shapes that can be related to those expected from particular pore shapes. There are four identified IUPAC hysteresis classifications. Each type relates to specific types of structures. Figure 5-2 presents the different types of hysteresis.

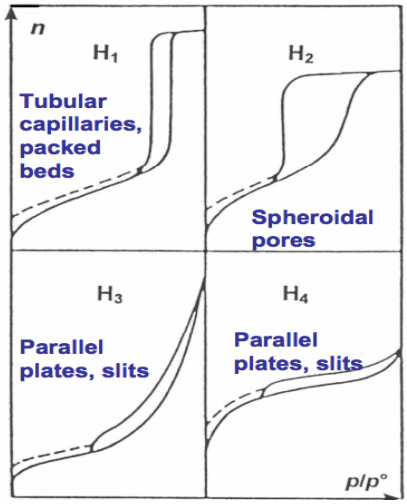

Figure 5-2. Different types of hysteresis[80].

Based from Figure 5-2, Type H2 closely resembles the hysteresis formed in our sorption analysis (Figure 5-3). From this, the average pore diameter and particle size can be calculated according to geometrical rules. The pore diameter and length were calculated to be 48.6 Å and 8.1 Å, respectively. Using a spherical pore model, we can imagine that the catalyst has shallow, wide pores.

In Figure 5-3, it shows the adsorption and desorption isotherms obtained using the BJH analysis. Meanwhile, the inset figure presents the pore size distribution (PSD) of the catalyst. From the isotherms, the hysteresis is shown opening clearly from 0.42 to 0.99 relative pressures. This section signifies the mesopore indicating the number of open pores while the micropore section is represented by the area from which the hysteresis closes until 0.05 relative pressure. In the inlet figure, the PSD graph shows the pore diameter mode. This means that the amount of micropores within the catalyst particle is present in abundant quantity. This makes its range value most likely to be sampled. From Table 5-2, the average pore diameter is 48.6 Å which is well within the PSD range in Figure 5-3.

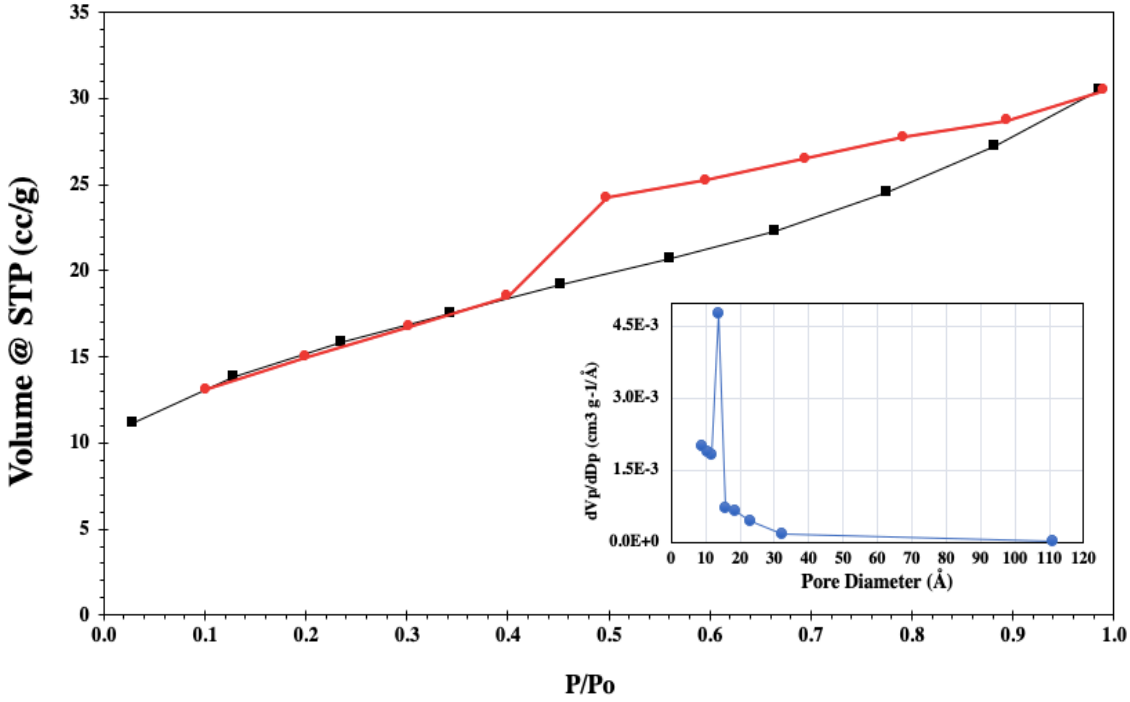

Figure 5-3. Adsorption and desorption isotherm and pore size distribution curve [inset] of the unspent catalyst.

To probe the catalytic surface, multiple SEM images were taken and the corresponding EDX analysis was also carried out to quantify the compounds adhering on the surface. Figure 5-4 presents the SEM images of the unspent catalyst. From these images, the catalyst has a smooth surface, with visible cracks and vices. Magnification of the surface gives a clearer view of these cracks and vices. In Table 5-3, the results of EDX analysis was presented.

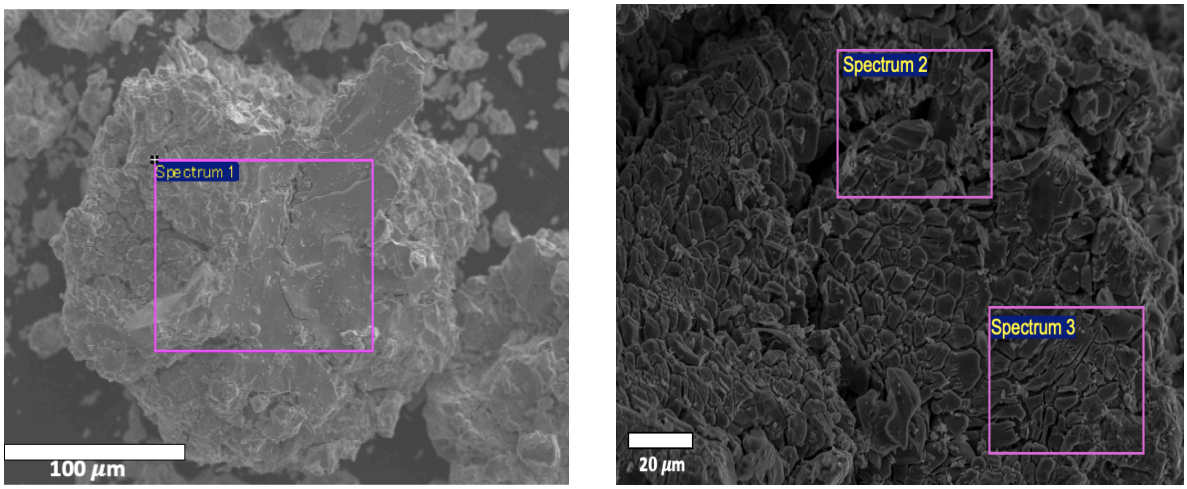

Figure 5-4. SEM image of unspent catalyst taken at 100 μm (left) and 20 μm (right) magnification.

Table 5-3. EDX analysis of the unspent catalyst.

Point of analysis	Weight percentage (%)			
	C	Al	Ni	Mo
Spectrum 1	5.70	6.29	76.82	11.18
Spectrum 2	2.14	3.16	90.34	4.36
Spectrum 3	5.85	5.37	85.07	3.71

From the above data, the catalyst particle is mainly composed of Ni which is in agreement with the manufacturer's data. Al and Mo were also detected in less quantity ratio. Since the catalyst is made by alloying these three main metals, the EDX data obtained for each point of analysis is not constant. This means that the elemental composition of the catalytic surface varies according to how it was alloyed or prepared. Nevertheless, these data proved that the catalyst is mainly made up of Ni which contains the active catalytic sites essential to assist the SCWG reaction. The presence of C on the catalytic surface could be a result of impurities contacted during the analysis.

A blank test conducted for 30 min was also performed to determine the morphology and change in particle characteristics of nickel catalyst if it is streamed in SCW only. As presented in Table 5-4, the surface area of the catalyst decreased to 40.3 m^2/g. This indicates that streaming the catalyst in SCW already gave a significant impact to its physical properties such as surface area. The influence of SCW on the pore volumes is not clarified at this stage and since the pore volume is a strong function of pore diameter and length, more test is needed to make a strong conclusion regarding this phenomenon. Figure 5-5 presents the PSD curve of the catalyst used in the blank test. From this graph, it is concluded that the catalyst had retained its microporous structure which is the same as the unspent catalyst.

Table 5-4. Properties of the catalyst used for blank test.

BET surface area, m^2/g	40.3
Pore Volume, $cm^3\ g^{-1}$	
Total	0.079
Micropore	0.004
Mesopore	0.075
Pore diameter, Å	117
Pore length, Å	19.5

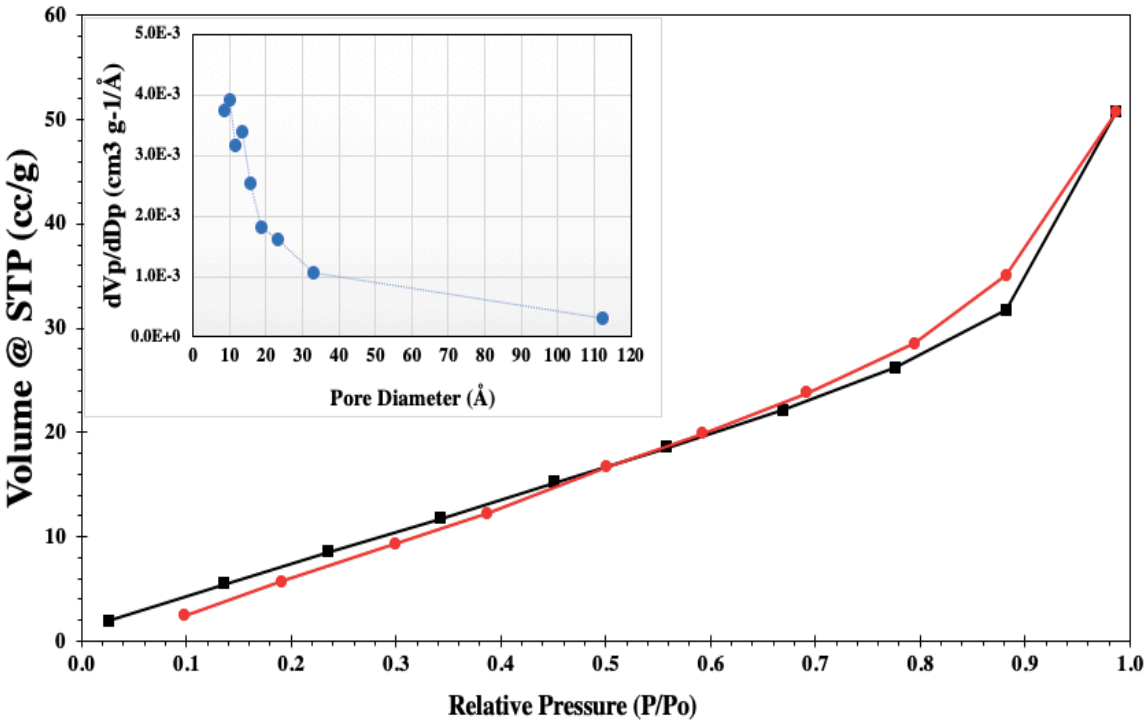

Figure 5-5. Adsorption and desorption isotherm and pore size distribution curve [inset] of the blank catalyst.

As presented in Figure 5-6, after streaming in SCW for 30 minutes, the catalytic surface resembled a disintegrated surface. This could explain the widening and lengthening of pore diameter and length. In Table 5-5, the amount of Ni is still present in abundant quantity indicating that streaming the catalyst in SCW alone does not have a significant influence in its metallic proportion. Moreover, the presence of C is still evident suggesting that there might be some carbon impurities present during sampling and analysis.

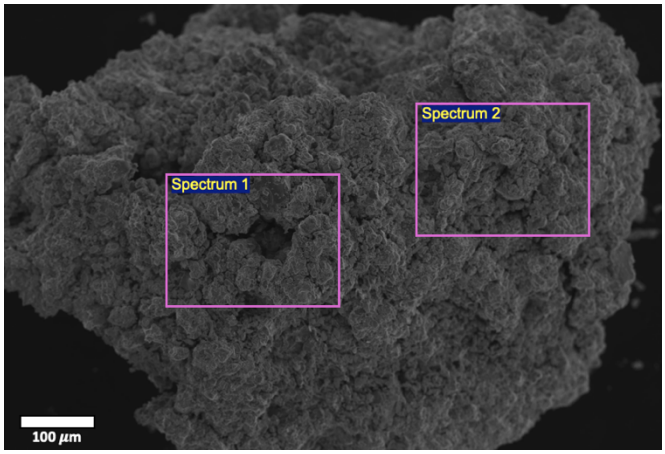

Figure 5-6. SEM image of the catalyst used during the blank experiment.

Table 5-5. EDX analysis of the catalyst used during the blank experiment.

Point of analysis	Weight percentage (%)			
	C	Al	Ni	Mo
Spectrum 1	2.47	5.35	90.92	1.27
Spectrum 2	4.01	11.09	83.62	1.28

5.2 Catalyst characterization after the gasification experiments

The experiments for the effect of biomass concentration on SCWG of oil was carried out using 2%, 3%, 4% and 5% oil concentration. The catalyst samples were obtained after each experiment, were dried and kept inside a fume hood for 24 hours under room temperature condition. Particle samples were randomly chosen among the dried samples from each experiment. It was then subjected to BET and BJH analysis using N_2 as the adsorbate gas. XRD and SEM-EDX analysis were also carried out to probe the catalyst surface. Qualification and quantification of elemental species present on the catalyst surface was also made possible using XRD and SEM-EDX analysis.

5.2.1 Characterization of the SCWG 0.02 catalyst

The catalyst subjected to SCWG of oil with 2% concentration for 300 min had an average BET surface area of 13.09 m^2/g which is over 4 times smaller than the unspent catalyst surface area. The total pore volume also decreased to 0.037 $cm^3\ g^{-1}$. The pore length and diameter also increased to 172 Å and 28.6 Å which indicates wider and deeper catalyst pore dimensions.

Table 5-6. Properties of the catalyst used for SCWG 0.02.

BET surface area, m^2/g	13.09
Pore Volume, $cm^3\ g^{-1}$	
Total	0.037
Micropore	0.003
Mesopore	0.034
Pore diameter, Å	172
Pore length, Å	28.6

From Figure 5-7, the PSD graph shows the distribution of pores within the catalyst particle. It shows that micropore sizes of about 13 – 15 Å were often sampled comprising the bulk of the catalytic structure. Nevertheless, this also implied that the catalyst was able

to retain its microporous structure. The BET surface area also had a significant decrease which was almost 4 times that of the unspent catalyst. This decrease in surface area may indicate pore blockage caused by species adhering on the catalytic surface. The widening of pore diameter and lengthening of pore length may be an indication of surface sintering due to extreme conditions observed in the process.

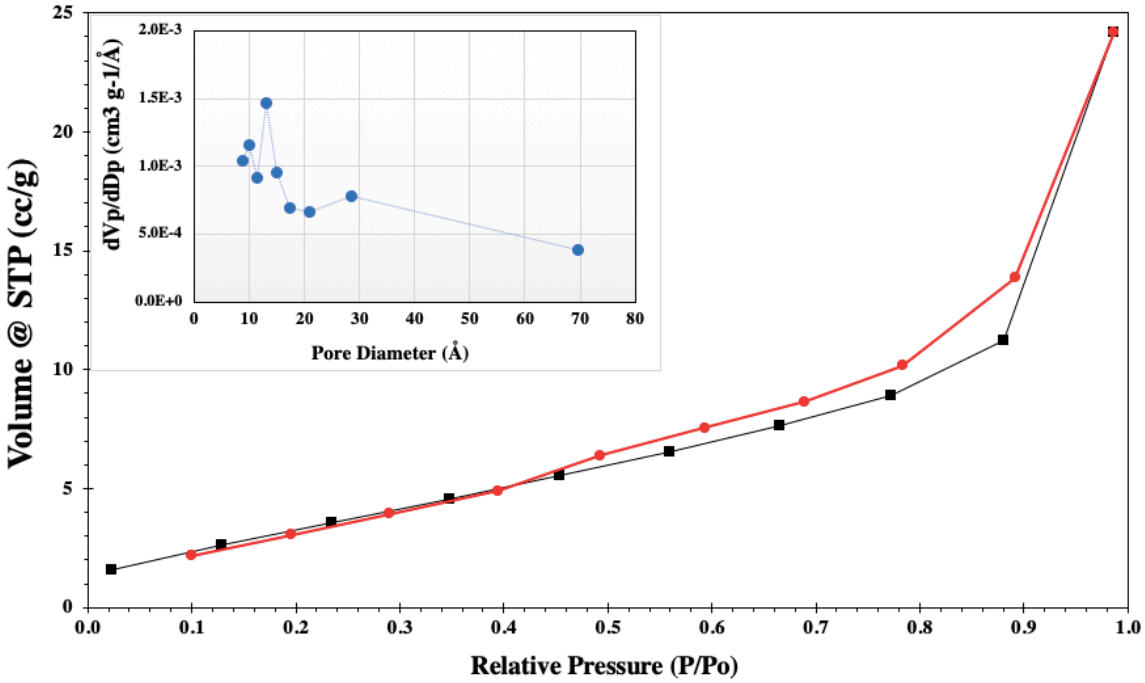

Figure 5-7. Adsorption and desorption isotherm and pore size distribution curve [inset] of the catalyst during SCWG 0.02.

The SEM-EDX analysis was also carried out to probe the catalytic surface. Both granulated and powdered catalyst particle left after the reaction were analyzed. Figure 5-8 shows the images and the EDX analysis point. It can be observed from these images that the catalyst outer structure had become fragmented. From the results of the EDX analysis presented in Table 5-7, the composition of the elements had changed. Nickel, which was the main component as shown in the results of unspent catalyst characterization had dramatically decreased its quantity. Meanwhile, the ratio of other elements had increased, particularly that of Al. Since EDX analysis computes the element composition based on the weight fraction of the detected elements, it cannot be used as a basis to quantify the elements according to the mass sample. Therefore, the increase in Al and Mo quantity ratio may have been possible due to the decrease in Ni quantity. Moreover, the decrease of Ni quantity may be due to its elution to liquid phase. Thus, ICP-MS analysis is essential to explain this phenomenon.

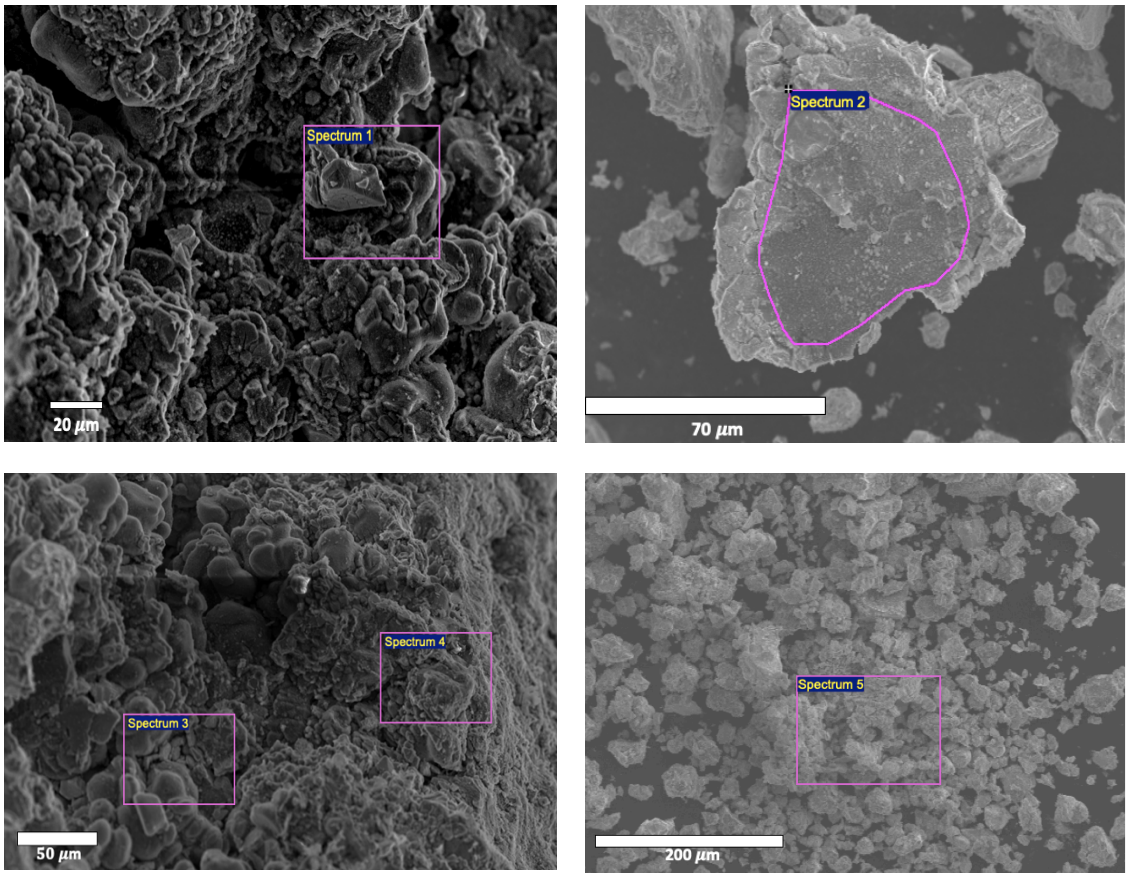

Figure 5-8. SEM image of the catalyst used during SCWG 0.02 experiment.

Table 5-7. EDX analysis of SCWG 0.02 catalyst.

Point of analysis	Weight percentage (%)			
	C	Al	Ni	Mo
Spectrum 1	7.24	6.48	84.78	1.50
Spectrum 2	11.41	61.13	25.40	2.06
Spectrum 3	8.42	8.34	79.12	4.12
Spectrum 4	7.58	4.22	84.15	4.05
Spectrum 5	12.35	70.67	0.26	66.77

5.2.2 Characterization of the SCWG 0.03 catalyst

As presented in Table 5-8, the catalyst subjected to SCWG of oil with 3% concentration for 300 min had an average BET surface area of 15.91 m^2/g. This surface area is slightly bigger than that of the SCWG 0.02 catalyst. The total pore volume is 0.048 $cm^3 g^{-1}$, which is slightly close to that of the unspent catalyst. The pore length and diameter also

increased to 181.4 Å and 30.2 Å which are slightly bigger than that of the SCWG 0.02 catalyst and are almost 4 times bigger than that of the unspent catalyst.

Table 5-8. Properties of the catalyst used for SCWG 0.03.

BET surface area, m^2/g	15.91
Pore Volume, $cm^3\ g^{-1}$	
Total	0.048
Micropore	0.001
Mesopore	0.047
Pore diameter, Å	181.4
Pore length, Å	30.2

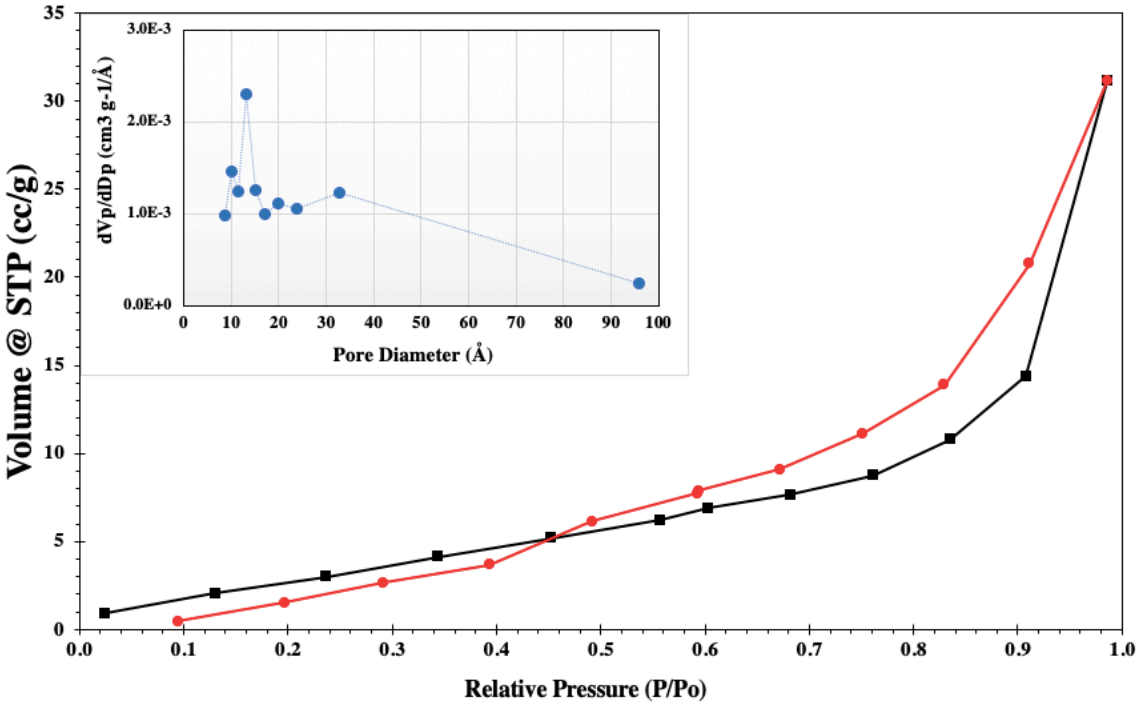

Figure 5-9. Adsorption and desorption isotherm and pore size distribution curve [inset] of the catalyst during SCWG 0.03.

Examining the PSD of the SCWG 0.03 catalyst shows that it has retained its microporous structure. The mode of the pore diameter sampling is from 10 – 20 Å, indicating that micropores still exist in abundant quantity. Figure 5-10 and Table 5-9 presents the SEM images and EDX point analysis results. From the images, some whitish particles are adhering on the catalytic surface. Moreover, the wider cracks could be observed and comparing with the images taken from the unspent catalyst, the surface structure is no longer smooth. From the results of EDX analysis, the amount of carbon adhering on the catalytic surface had taken a larger weight percentage share as compared with other detected elements.

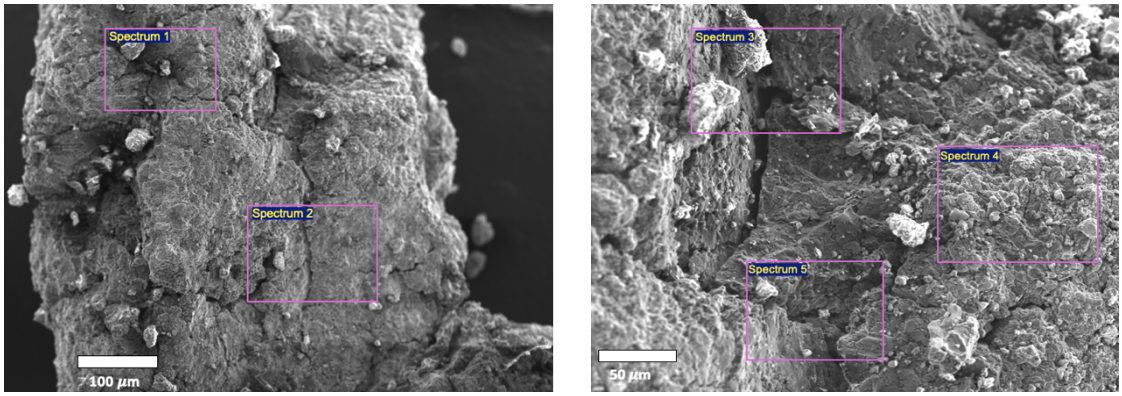

Figure 5-10. SEM image of the catalyst used during SCWG 0.03 experiment.

Table 5-9. EDX analysis of SCWG 0.03 catalyst.

Point of analysis	Weight percentage (%)			
	C	Al	Ni	Mo
Spectrum 1	39.15	18.38	41.47	1.00
Spectrum 2	40.22	12.06	47.09	0.63
Spectrum 3	29.16	38.32	31.98	0.54
Spectrum 4	33.45	28.50	36.25	1.80
Spectrum 5	38.84	23.69	36.55	1.04

It is possible that this carbon is either char or tar which are known products during incomplete biomass gasification. Also, the Ni quantity decreased while Al increased. One possible interpretation of this is that the Ni particles were eluted to liquid phase, exposing the hidden Al particles. This made the EDX detector detect the exposed Al particles, thus making its component ratio higher.

5.2.3 Characterization of the SCWG 0.04 catalyst

In Table 5-10, the catalyst subjected to SCWG of oil with 4% concentration for 300 min had an average BET surface area of 9.14 m^2/g. This surface area is almost 6 times smaller than that of the unspent catalyst and is also smaller than the SCWG 0.02 and SCWG 0.03 catalyst. The total pore volume is 0.027 $cm^3\ g^{-1}$, which is almost twice smaller than that of the unspent catalyst. The pore length and diameter also increased to 176.9 Å and 29.5 Å which are quite similar with that of the SCWG 0.03 catalyst. In Figure 5-11, the PSD curve plotted from gas sorption analysis of the SCWG 0.04 catalyst is presented.

Table 5-10. Properties of the catalyst used for SCWG 0.04.

BET surface area, m^2/g	9.14
Pore Volume, $cm^3\ g^{-1}$	
Total	0.027
Micropore	0.001
Mesopore	0.026
Pore diameter, Å	176.9
Pore length, Å	29.5

From the graph, the mode of the pore diameter increased to 30 Å suggesting that the majority of the catalytic particle now has a mesoporous structure. This may probably have been caused by the inability of the adsorbate gas to penetrate to the micropores due to pore blockage. This is also evident with the dramatic decrease in BET surface area. The occurrence of pore blockage is caused by two reasons. First, species and other impurities adhere on the catalytic surface. These potentially plug and foul the pores, thus making further diffusion to the micropore structures impossible. Second is the sintering of the catalytic pore. If it is possible that the outer catalytic structure is being removed due to extreme reaction conditions employed in the process, this potentially causes the removal of active catalytic sites. This assumption is supported by the decline of catalytic performance

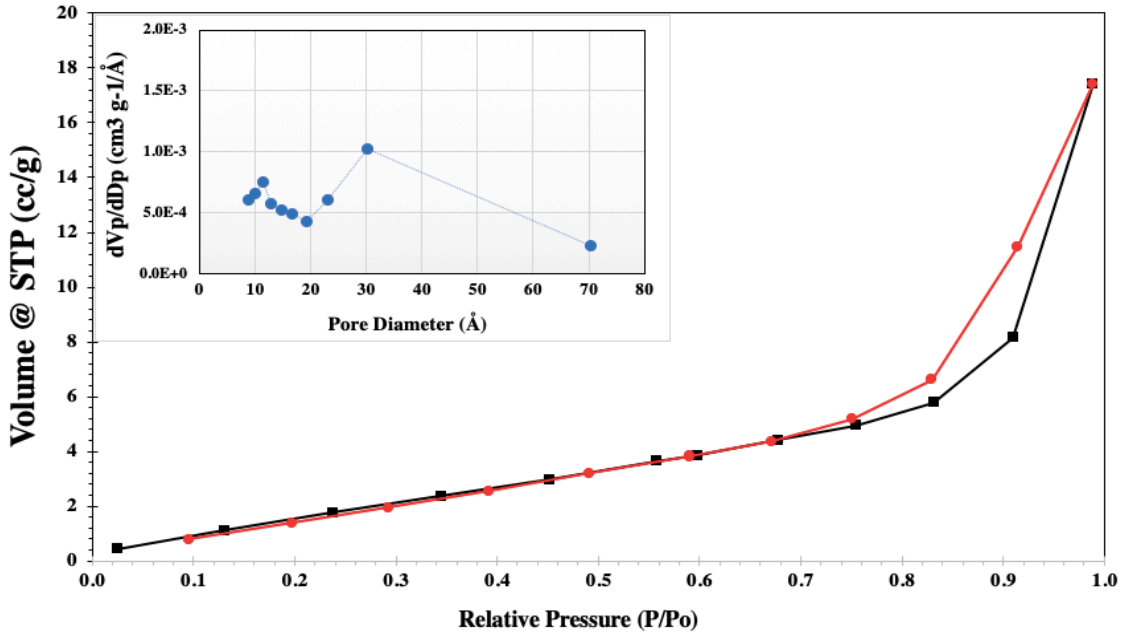

Figure 5-11. Adsorption and desorption isotherm and pore size distribution curve [inset] of the catalyst during SCWG 0.04.

in terms of gas yields and efficiencies. Probing of the catalyst surface using SEM-EDX shows the results in Figure 5-12 and Table 5-11. From the SEM images, some impurities adhere on the catalytic surface along its cracks and vices. Also, the surface appears to have a crumble-like appearance. From the results of EDX analysis, the amount of Ni particle is surprisingly higher compared with the results of the previous catalysts obtained after each experiment.

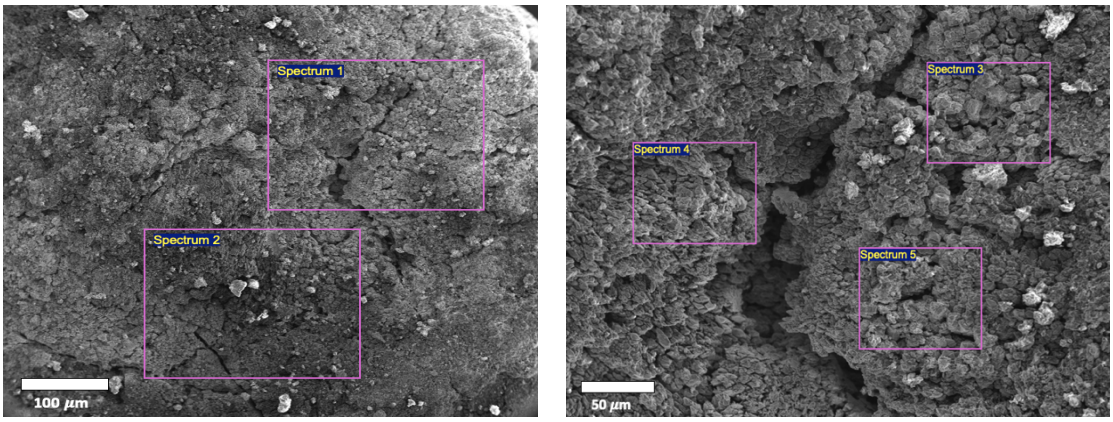

Figure 5-12. SEM image of the catalyst used during SCWG 0.04 experiment.

Table 5-11. EDX analysis of SCWG 0.04 catalyst.

Point of analysis	Weight percentage (%)			
	C	Al	Ni	Mo
Spectrum 1	6.16	1.48	92.13	0.23
Spectrum 2	4.76	7.80	86.78	0.66
Spectrum 3	13.54	9.09	76.10	1.28
Spectrum 4	4.66	0.84	94.35	0.15
Spectrum 5	1.73	0.96	97.30	0.00

Since the catalyst samples reserved for analytical measurements were taken randomly from the batch of catalysts used after every experiment, it is possible that the sample measured by SEM-EDX did not receive full extent of the impact of gasification. This means that the sample that was measured may have been in the position inside the reactor wherein deactivation has not fully taken into effect yet.

5.2.4 Characterization of the SCWG 0.05 catalyst

In Table 5-12, the catalyst subjected to SCWG of oil with 5% concentration for 300 mins had an average BET surface area of 15.01 m^2/g. This surface area is comparably similar with that of SCWG 0.02 and SCWG 0.03. The total pore volume is 0.032 $cm^3\ g^{-1}$ which is almost twice smaller than that of the unspent catalyst. The pore length and diameter also increased to 127.3 Å and 21.22 Å which are quite similar with that of the catalyst used during the blank test. In Figure 5-13, the PSD curve for the SCWG 0.05 catalyst is presented. From the graph, the catalyst had maintained a microporous structure. However, it is noticeable how the other pore structures are poorly sampled. Further tests and analysis should be done in order to have a proper conclusion regarding this outcome.

Table 5-12. Properties of the catalyst used for SCWG 0.05.

BET surface area, m^2/g	15.01
Pore Volume, $cm^3\ g^{-1}$	
Total	0.032
Micropore	0.008
Mesopore	0.024
Pore diameter, Å	127.3
Pore length, Å	21.22

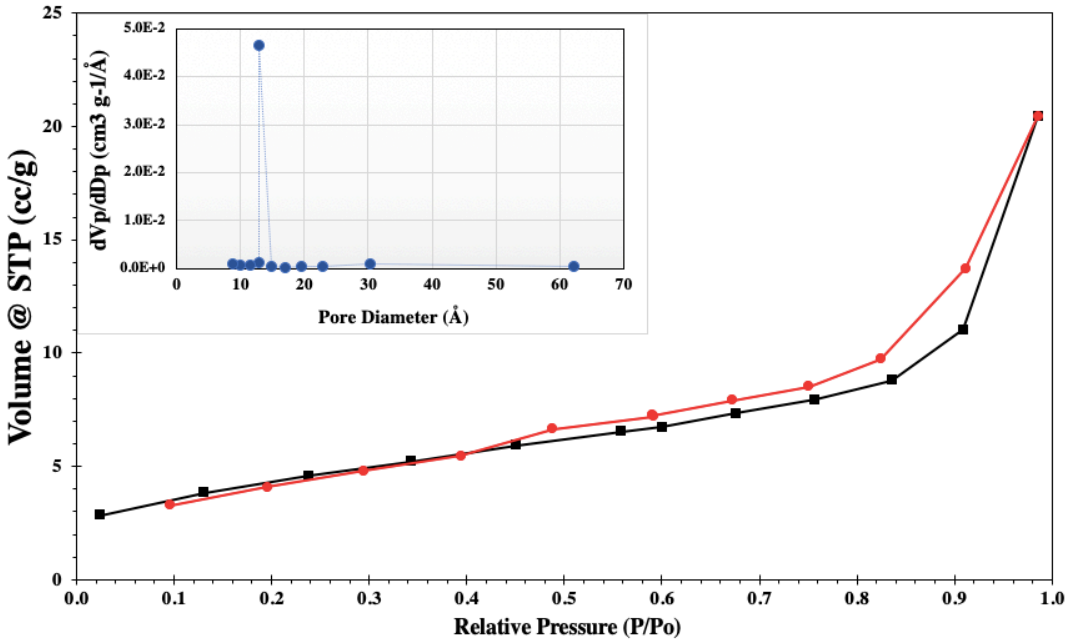

Figure 5-13. Adsorption and desorption isotherm and pore size distribution curve [inset] of the catalyst during SCWG 0.05.

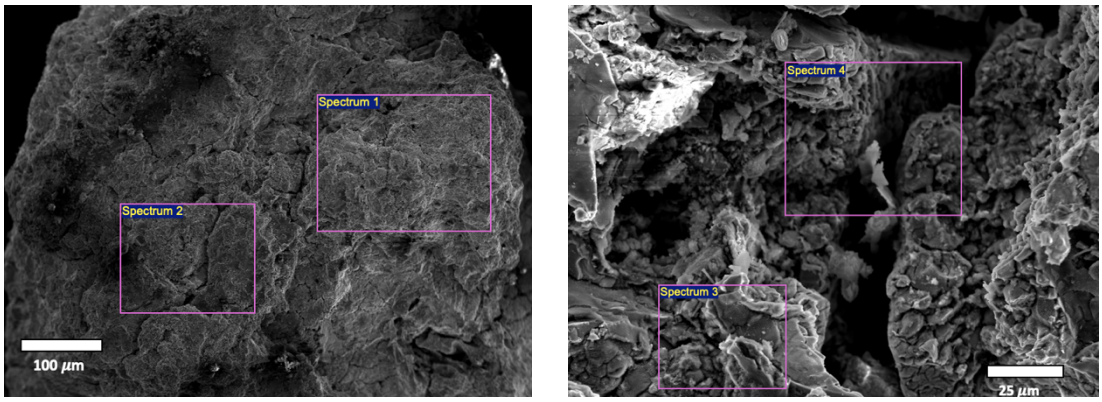

Figure 5-14. SEM image of the catalyst used during SCWG 0.05 experiment.

Table 5-13. EDX analysis of SCWG 0.05 catalyst.

Point of analysis	Weight percentage (%)			
	C	Al	Ni	Mo
Spectrum 1	11.52	23.04	64.98	0.46
Spectrum 2	9.46	14.98	74.74	0.82
Spectrum 3	57.29	16.08	26.42	0.22
Spectrum 4	10.00	69.76	18.37	1.87

Further probing of the catalyst surface using SEM-EDX revealed that the results obtained at each analysis points were not constant. The results vary from sample to sample that is being analyzed. From SEM images, it can be seen that the surface of the catalysts is rough, and some particles are adhering onto it. Meanwhile, EDX analysis shows that the percentage of Ni is greater than the other detected elements. However, it should be noted that the results vary according to each sampling point and catalyst sample. The presence of carbon is also notable which could be the species adhering on the catalytic surface.

5.2.5 Summary of the XRD results obtained for all experiments

XRD analysis was carried out to qualitatively analyze the catalyst surface. The appearance of oxidation peaks was not observed which rules out the speculation that oxidation on catalytic surface caused catalyst deactivation. From the results, it is noticeable how the metallic peaks are not emphasized in the unspent catalyst. Immersing the catalyst in SCW induced the growth of Ni and Al. This suggests that soaking the catalyst in SCW

enhances its Ni and Al content, probably due to the removal of impurities present in the unspent catalyst.

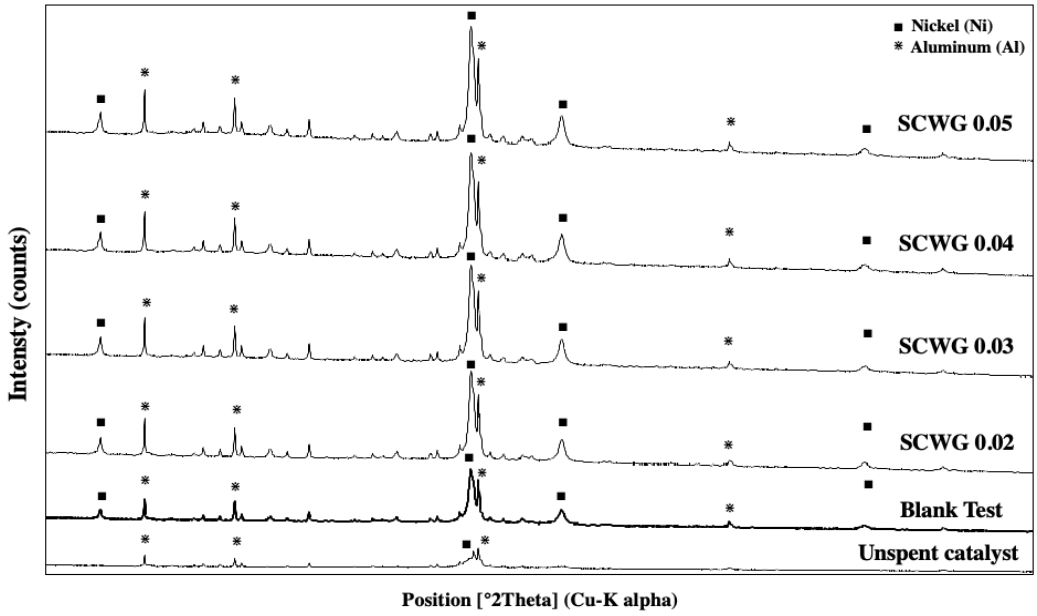

Figure 5-15. The XRD results obtained for all experiments conducted at 400 °C, 25 MPa.

5.3 Observation of catalyst deactivation

As shown in Table 5-14, the catalyst subjected to SCWG of oil with 2% concentration for 60 mins had an average BET surface area of 10.73 m^2/g. This surface area is smaller than the surface area obtained from the SCWG 0.02 run for 300 min. The total pore volume is 0.031 $cm^3\ g^{-1}$, which is slightly smaller than SCWG 0.02 at 300 min. The pore length and diameter were 176 Å and 29.3 Å which are quite similar with SCWG 0.02 at 300 min. In Figure 5-17, the PSD curve for the SCWG 0.02 at 60 min catalyst is presented. From the graph, the catalyst had maintained both microporous and mesoporous structure ranging from 13 – 30 Å.

Table 5-14. Properties of the catalyst used for SCWG 0.02 for 60min.

BET surface area, m^2/g	10.73
Pore Volume, $cm^3\ g^{-1}$	
Total	0.031
Micropore	0.008
Mesopore	0.025
Pore diameter, Å	176
Pore length, Å	29.3

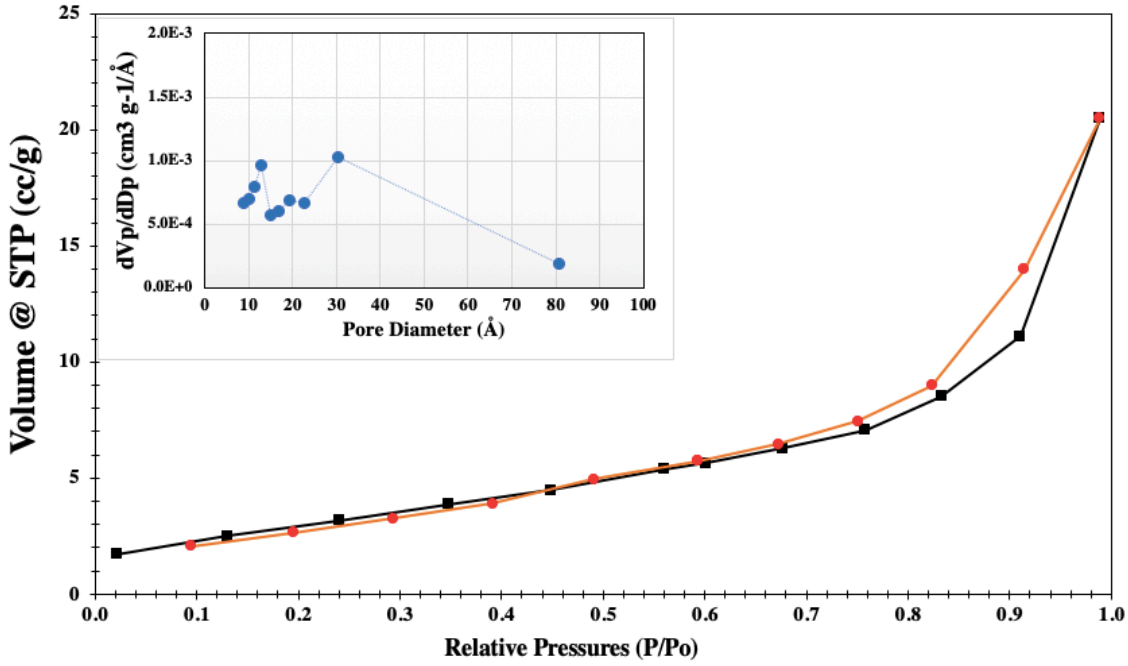

Figure 5-16. Adsorption and desorption isotherm and pore size distribution curve [inset] of the catalyst during SCWG 0.02 at 60 min gasification time.

Further probing of the catalytic surface using SEM generated images presented in Figure 5-18. It could be observed that after 60 min of reaction time, the catalytic surface had become rough, with cracks and vices visible on the surface. The presence of whitish layer on the surface is also visible, indicating that this may be a layer of carbon produced during biomass gasification.

In Table 5-15, the EDX results of each chosen points are tabulated. There is a significant amount of C adhering on the surface with the decrease of Ni content. The ratio of Al also increased by almost 10 – 15 times of that of the unspent catalyst, whereas the weight ratio of Mo increased. However, it should be noted that the results acquired were not constant and varied at each point of analysis. This indicates that deactivation in terms of carbon deposition and surface sintering was not uniform in each catalytic particle.

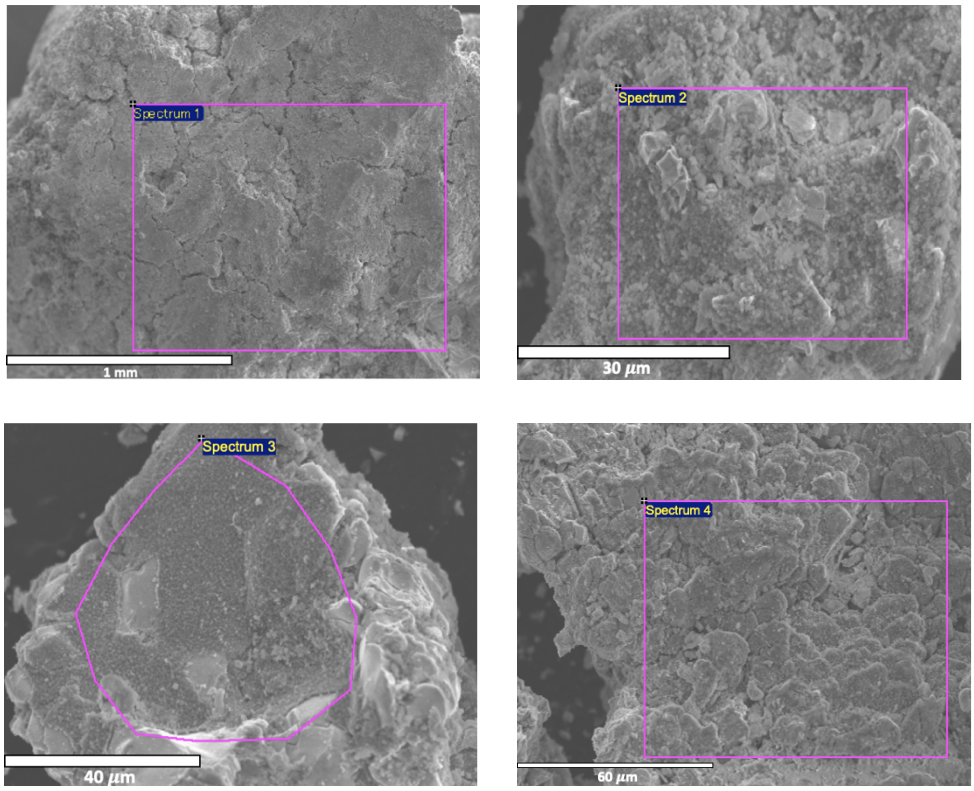

Figure 5-17. SEM image of the catalyst used during SCWG 0.02 at 60min experiment.

Table 5-15. EDX analysis of SCWG 0.02 at 60 min catalyst.

Point of analysis	Weight percentage (%)			
	C	Al	Ni	Mo
Spectrum 1	15.63	33.13	44.16	7.07
Spectrum 2	12.17	54.61	31.90	1.31
Spectrum 3	11.16	53.91	33.25	1.69
Spectrum 4	12.52	45.18	39.73	2.57

In Table 5-16, the catalyst subjected to SCWG of oil with 2% concentration for 180 min had an average BET surface area of 13.31 m^2/g. This surface area was larger than the surface area obtained from the SCWG 0.02 run for 60 min and comparatively similar to the SCWG 0.02 conducted at 300 min. The total pore volume is 0.046 $cm^3\ g^{-1}$, which is larger than SCWG 0.02 run for 300 min. The pore length and diameter were 206 Å and 34.2 Å which are larger compared with SCWG 0.02 run for 300 min. In Figure 5-18, the PSD curve

for the SCWG 0.02 at 180 min catalyst is presented. From the graph, the catalyst is mostly composed of micropores ranging from 10 – 20 Å.

Table 5-16. Properties of the catalyst used for SCWG 0.02 for 180min.

BET surface area, m^2/g	13.31
Pore Volume, $cm^3\ g^{-1}$	
Total	0.046
Micropore	0.009
Mesopore	0.037
Pore diameter, Å	206
Pore length, Å	34.3

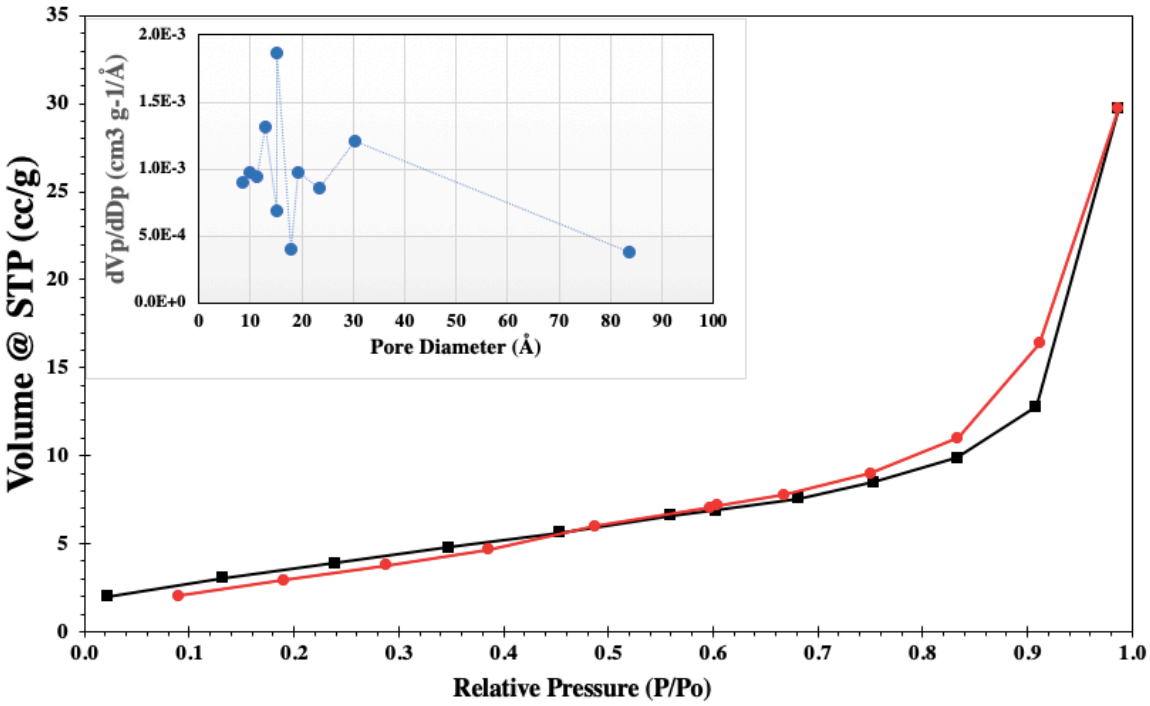

Figure 5-18. Adsorption and desorption isotherm and pore size distribution curve [inset] of the catalyst during SCWG 0.02 at 180 min gasification time.

Further probing of the catalytic surface gave the results of SEM-EDX analysis as presented by Figure 5-19. From the SEM images, the change in the catalytic surface is evident by the cracks and its rough surface. This may mean that the surface morphology has changed. At first, the catalyst had a smooth surface which was mainly composed of Ni; then as the particle was streamed in SCW, the surface slowly disintegrated and formed rough surface layers. From the results of EDX analysis, Spectrum 2 exhibits a smooth surface

wherein it is composed of 84.28% Ni. Comparing it with other images that has rough surface, the amount of Ni is less whereas C and Al mainly comprised the elemental distribution.

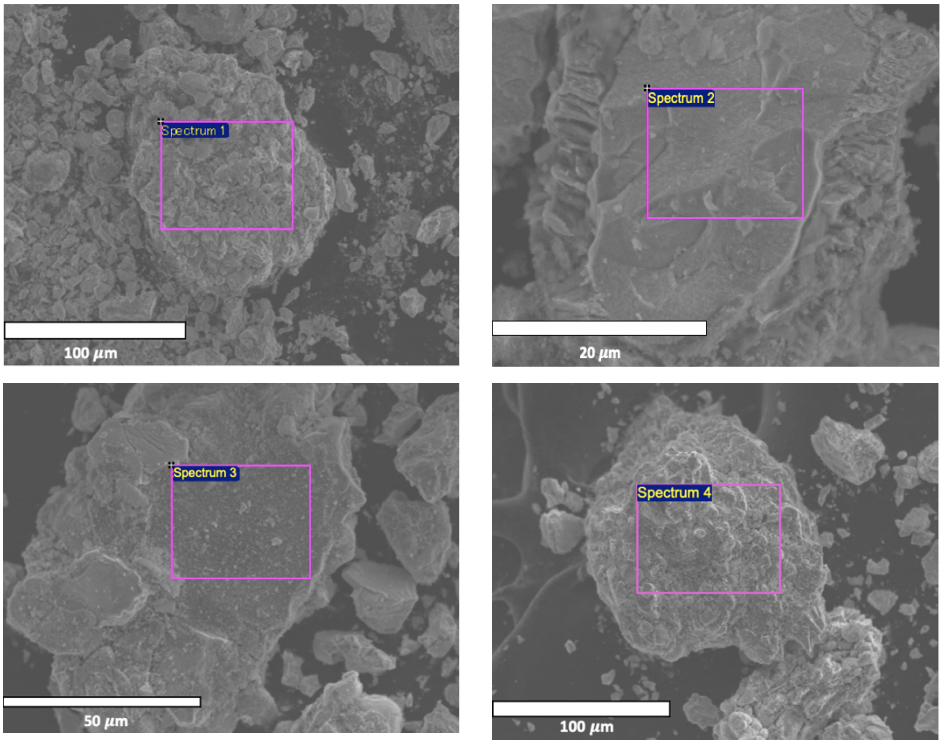

Figure 5-19. SEM image of the catalyst used during SCWG 0.02 at 180 min experiment.

Table 5-17. EDX analysis of SCWG 0.02 at 180 min catalyst.

Point of analysis	Weight percentage (%)			
	C	Al	Ni	Mo
Spectrum 1	34.21	25.25	18.85	21.70
Spectrum 2	5.24	5.29	84.28	5.20
Spectrum 3	8.00	21.83	67.89	2.29
Spectrum 4	35.76	28.84	15.60	19.80

5.4 Results of ICP-MS analysis

To determine the metal elution of the main components of the catalyst to the liquid phase, ICP-MS analysis was conducted. Three standards were prepared for Ni, Al and Mo analysis. However, it became a challenge to measure the Al content as aluminum exists in different isotopes and usually in minute quantities, making the measurement error large during the analysis of Al content.

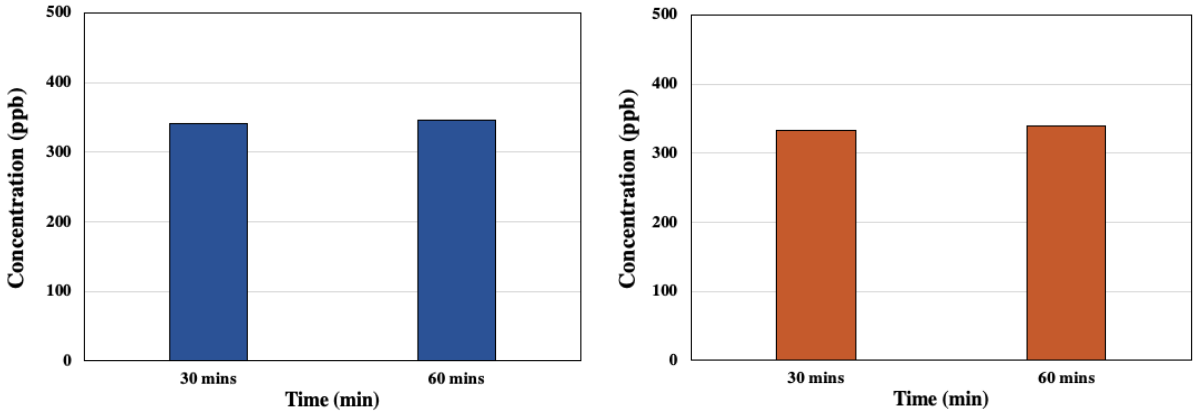

Figure 5-20. ICP-MS results of Ni (left) and Mo (right) for SCWG 0.02 after 60 min gasification time measured in ppb concentration.

From Figure 5-20, Ni and Mo eluting to the liquid phase were detected. During the first 30 min of gasification reaction, the elution of Ni to the liquid phase was evident. Assuming that the active catalytic sites were mainly composed of Ni, the loss of active catalytic sites is a possible candidate for catalyst deactivation. Furthermore, the elution of Mo to the liquid phase suggests that not only Ni is being removed during the SCWG process but also the other components that make up the catalyst bulk particle are eluted.

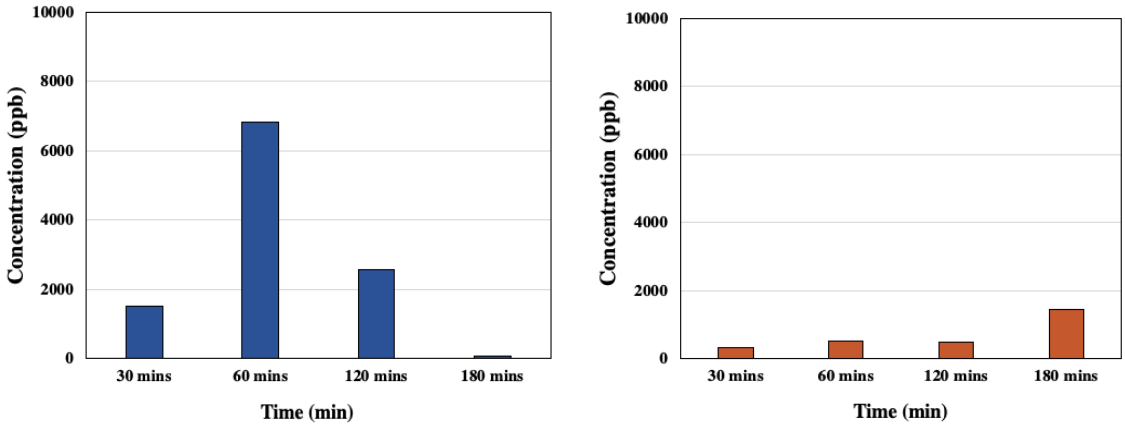

Figure 5-21. ICP-MS results of Ni (left) and Mo (right) for SCWG 0.02 after 180 min gasification time measured in ppb concentration.

Further analysis of liquid samples acquired after 180 min gasification also showed that Ni and Mo are being carried to the liquid phase. Although the initial results during the first 60 min of gasification are not similar to the results shown in Figure 5-20, particle elution is still evident, especially that of the Ni. After 60 min, the elution concentration was significantly high and decreased as gasification progressed. As for Mo, the elution concentration increased until the end of 180 mins experiment. One possible scenario could be that as more Ni particles elute to the liquid phase, the surface of the catalyst is being thinned exposing much of the alloyed Al and Mo components.

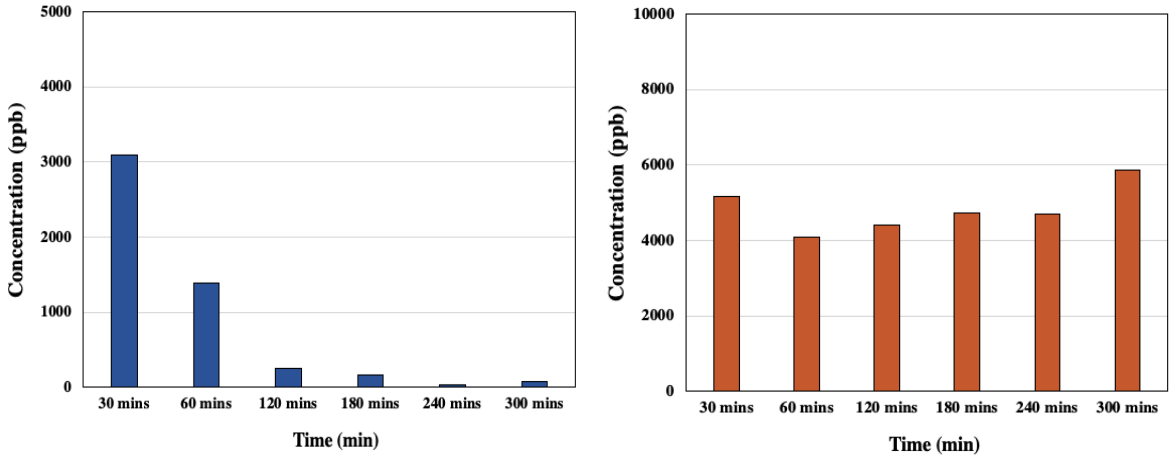

Figure 5-22. ICP-MS results of Ni (left) and Mo (right) for SCWG 0.02 after 300 min gasification time measured in ppb concentration.

After the 300-min gasification time, the trend of Ni and Mo particle elution to the liquid phase is presented in Figure 5-26. At the start of the reaction, much Ni was lost to the liquid phase and as reaction progressed, the elution decreased. One possibility could be that as more outer catalytic particles are being eluted away, the catalyst particle is thinned exposing the 'more compact' part of the particle. This is quite evident in Figure 5-23 and Table 5-16 wherein a smooth surface of the catalyst could be seen which is comprised mainly of Ni.

Chapter 6
SUMMARY, CONCLUSIONS AND RECOMMENDATIONS

This chapter presents the main findings of supercritical water gasification of vegetable oil using nickel catalyst study. From the results, conclusions were drawn and recommendations for future work were given. In the first section, the conclusions to each experimental section were discussed and answers to the research questions were given. The next section gives the future recommendations on how to improve the study.

6.1 Summary

In Chapter 4, the decomposition of oil in supercritical water gasification has been studied. The experiments were conducted to evaluate the effect of biomass concentration using four (4) different oil concentrations at 2, 3, 4, and 5%. This also aimed to determine the oil concentration which can give a clearer view of catalyst deactivation behavior. The performance of each operating condition was evaluated according to gas yields and efficiencies. The decomposition products identified from gas and liquid phase analysis were also presented. The results showed that as biomass concentration increased, gas yields and efficiencies decreased. From a study by Yu et al.[48], they also found this similar trend. From their results, the yields of H_2 decreased while CH_4 yields increased as glucose concentration increased. From this study, both H_2 and CH_4 yields decrease as oil concentration increased. Examining the carbon balance, the increase in the amount of solids was notable suggesting that inorganics are being formed. This is an indication of declining system efficiency signifying the inability of the system to gasify the biomass into gas products. This proves that catalyst deactivation behavior can be observed with the system's ability to convert the carbon present in the biomass. It is also concluded that at lower biomass concentration, the system performance was comparably better than higher biomass concentration.

The unspent catalyst was characterized using gas sorption techniques and it was found out to have a surface area of 58.2 m^2/g. However, after the gasification experiments conducted for 300 minutes, this surface area value decreased by 4 – 6 times. This suggests the loss of active surface area which may have caused the catalyst' decline in activity. Analysis probing the catalytic surface using SEM and quantification of the species adhering on the surface using EDX were carried out. From SEM images, the unspent catalyst was found out to have a smooth surface, with visible cracks and vices. However, after exposing

the catalyst to the gasification conditions, some impurities adhered on the catalytic surface along its cracks and vices. Results from qualitative analysis using XRD did not give the appearance of oxidation peaks. This rule out the speculation that catalyst deactivation was caused by oxidation. To further elucidate its deactivation behavior, two experiments were added at 60 min and 180 min total gasification time. After 60 min and 180 min reaction time, the catalytic surface had become rough, with cracks and vices visible on the surface. There was a significant amount of C adhering on the surface with the decrease of Ni content. Also, the ratio of Al increased by almost 10 – 15 times of that of the unspent catalyst, whereas the weight ratio of Mo increased. From this, carbon deposition and sintering of the catalyst could be the possible causes of deactivation. However, it should be noted that the results acquired were not constant and varied at each point of analysis. This indicates that deactivation in terms of carbon deposition and surface sintering was not uniform in each catalytic particle. To determine the metal elution of the main components of the catalyst to the liquid phase, ICP-MS analysis was conducted. From Figure 5-20 to 5-22, Ni and Mo particles eluting to the liquid phase were detected. The presence of higher Ni quantity at the start of the reaction as seen from EDX results in Table 5-5 and its gradual loss after exposure in SWCG of oil indicates the loss of active catalytic sites. As more Ni particles elute to the liquid phase, the surface of the catalyst is being thinned exposing much of the alloyed Al and Mo components. Two mechanisms are hereby proposed:

① Al and Mo exists in lesser quantity and that the bulk of the catalyst is made up of Ni. As the catalyst is streamed in SCW, Ni particles coating the surface is being removed and thereby adheres in the liquid phase. This causes the loss of active catalytic sites. However, the role of carbon in this mechanism should not be neglected. It could be that:

② At the early onset of gasification, carbon from the biomass adheres on the catalytic surface. However, as deactivation moves to its advance stages, the outer catalytic surface is being removed which includes the Ni and C particles.

6.2 Conclusion

In this study, the applicability of supercritical water gasification in vegetable oil treatment and the observation of nickel catalyst morphology during this process were studied. It was found out that at optimum conditions, SCWG proved to be a viable process in converting oil into desired gaseous products such as H_2 and CH_4. From the results, it was concluded that the loss of catalytic efficiency can be observed by the system's ability to convert the carbon into gaseous products. The possible causes of catalyst deactivation were also identified. It was concluded that carbon deposition followed by particle sintering could have been the possible cause of catalyst deactivation. Further experiments and analysis should be added to present a strong evidence to backed up these assumptions.

6.3 Recommendations

For the improvement of this research, the following recommendations are suggested:

1. Replacing the plunger pump with low flowrate-capable pump

   Throughout the whole study, a plunger pump was used to deliver the oil to the system. However, since the lowest acceptable flowrate it is capable of delivering was 0.45 mL/min, operation at lower flowrates was not achievable. Consequently, this limited the oil fraction to only 2% if the slurry pump, which was used to deliver water, was to be operated at 23.0 mL/min. Operating the slurry pump at higher flowrates would give lower reactant residence times which may not be sufficient for the reaction to occur. Also, at very high flowrates, heating rate is slow. At water flowrate of 23.0 mL/min and furnace set temperature of 700 °C, it approximately took 1 – 3 hours, depending on seasonal variations. This, in turn, leads to the next recommendation.

2. Conduct the experiment in a temperature-controlled room

   During the conduct of experiment, it was observed that the reactor heating and cooling rates varied according to seasonal changes. During summer, it took around 1.5 hours for the reactor to reach 400 °C with set furnace temperature of 700 °C. However, during winter, it took almost 3 hours to reach and maintain the desired temperature. Since the catalysts were preloaded in the reactor, exposure to such long heating time may have imparted some changes in the catalytic structure. The same is also true when cooling down the reactor. To rule out the seasonal variation problem, placing the entire setup in a temperature-controlled room is recommended.

3. Down-scaling of the experimental setup

   In the current research, the total system residence time, herein defined as the time it takes the reactants to reach the end of the gasification system, was quite long. Using low flowrates and downsizing the reactor by using a 1/2 inch OD Swagelok tube is recommended. Not only it achieves shorter equilibrium time, but also minimizes the experimental errors due to longer equipment and apparatus connected in the system.

4. Using a molten salt bath as the primary heating source

   The cylindrical furnace used for the experiments was designed to cater the upward flow of the reactants up to the reactor. However, its heating rate is very slow and this may have affected the catalyst inside the reactor. Using a molten salt bath with enough opening diameter and depth could address this concern. When the reactor is immersed in the salt bath preheated up to the desired temperature, the molten salt will envelop the reactor with uniform heating, thus an isothermal condition is achieved.

REFERENCES

[1] M. M. Rahman, S. B. Mostafiz, J. V. Paatero, and R. Lahdelma, "Extension of energy crops on surplus agricultural lands: A potentially viable option in developing countries while fossil fuel reserves are diminishing," *Renew. Sustain. Energy Rev.*, vol. 29, pp. 108–119, 2014.

[2] S. Ladanai and J. Vinterbäck, "Global Potential of Sustainable Biomass for Energy," *SLU, Institutionen för energi och Tek. Swedish Univ. Agric. Sci. Dep. Energy Technol.*, p. 32, 2009.

[3] E. Gasafi, M. Y. Reinecke, A. Kruse, and L. Schebek, "Economic analysis of sewage sludge gasification in supercritical water for hydrogen production," *Biomass and Bioenergy*, vol. 32, no. 12, pp. 1085–1096, 2008.

[4] M. Momirlan and T. N. Veziroglu, "Current status of hydrogen energy," *Renew. Sustain. Energy Rev.*, vol. 6, no. 1–2, pp. 141–179, 2002.

[5] S. S. Toor, L. Rosendahl, and A. Rudolf, "Hydrothermal liquefaction of biomass: A review of subcritical water technologies," *Energy*, vol. 36, no. 5, pp. 2328–2342, 2011.

[6] A. E. Farrell, D. W. Keith, and J. Corbett, "A strategy for introducing hydrogen into transportation," *Energy Policy*, vol. 31, no. 13, pp. 1357–1367, 2003.

[7] U. D. of Energy, "A national vision of America's transition to a hydrogen economy, to 2030 and beyond," 2002, no. United States Department of Energy, p. 28.

[8] E. COMMISSION, *Special Report Eur 20719 En*. 2003.

[9] Shell, "Energy needs, choices and possibilities: scenarios to 2050," 2001, p. 60.

[10] N. Brinkman, M. Wang, T. Weber, and T. Darlington, "Advanced Fuel / Vehicle Systems — A North American Study of Energy Use , Greenhouse," no. May, pp. 1–175, 2005.

[11] S. Dunn, "Comments on: Hydrogen futures: toward a sustainable energy system," 1776 Massachusetts Ave., NW Washington DC, 157.

[12] M. Toba, Y. Abe, H. Kuramochi, M. Osako, T. Mochizuki, and Y. Yoshimura, "Hydrodeoxygenation of waste vegetable oil over sulfide catalysts," *Catal. Today*, vol. 164, no. 1, pp. 533–537, 2011.

[13] R. Putra, T. Juliantoa, P. Hartono, R. Puspitasaria, and A. Kurniawan, "Pre-treatment of Used-Cooking Oil as Feed Stocks of Biodiesel Production by Using Activated Carbon and Clay Minerals," *Int. J. Renew. Energy Dev.*, vol. 3, no. 1, pp. 33–35, 2014.

[14] A. Sherif, S. A., Goswami, D. Y., Stefanakos, E. L., & Steinfeld, "Handbook of Hydrogen Energy," *CRC Press*, no. 22186, p. 960, 2014.

[15] Y. Lu, Y. Zhu, S. Li, X. Zhang, and L. Guo, "Behavior of nickel catalysts in supercritical water gasification of glucose: Influence of support," *Biomass and Bioenergy*, vol. 67, no. September, pp. 125–136, 2014.

[16] Y. Guo, S. Z. Wang, D. H. Xu, Y. M. Gong, H. H. Ma, and X. Y. Tang, "Review of catalytic supercritical water gasification for hydrogen production from biomass," *Renew. Sustain. Energy Rev.*, vol. 14, no. 1, pp. 334–343, 2010.

[17] D. D. Do and R. H. Weiland, "Substrate inhibited kinetics with catalyst deactivation in an isothermal CSTR," *AIChE J.*, vol. 26, no. 6, pp. 1020–1028, 1980.

[18] T. Minowa, F. Zhen, and T. Ogi, "Cellulose decomposition in hot-compressed water with alkali or nickel catalyst," *J. Supercrit. Fluids*, vol. 13, no. 1–3, pp. 253–259, 1998.

[19] E. G. Elliot, D.C., Sealock, L.J., Baker, "Chemical processing in high-pressure aqueous environments. 2. Development of catalysts for gasification.," *Ind. Eng. Chem. Res.*, vol. 32, pp. 1542–1548, 1993.

[20] S. Nanda, S. N. Reddy, A. K. Dalai, and J. A. Kozinski, "Subcritical and supercritical water gasification of lignocellulosic biomass impregnated with nickel nanocatalyst for hydrogen production," *Int. J. Hydrogen Energy*, vol. 41, no. 9, pp. 4907–4921, 2016.

[21] T. Yoshida, Y. Oshima, and Y. Matsumura, "Gasification of biomass model compounds in supercritical water," *Biomass and Bioenergy*, vol. 26, pp. 71–78, 2004.

[22] O. Sawai, T. Nunoura, and K. Yamamoto, "Supercritical water gasification of sewage sludge using bench-scale batch reactor: advantages and drawbacks," *J Mater Cycles Waste Manag*, no. 16, pp. 82–92, 2014.

[23] O. Sawai, T. Nunoura, and K. Yamamoto, "Application of subcritical water liquefaction as pretreatment for supercritical water gasification system in domestic waste water treatment plant," *J. Supercrit. Fluids*, vol. 79, pp. 274–282, 2013.

[24] H. T. Nguyen, E. Yoda, and M. Komiyama, "Catalytic supercritical water gasification of proteinaceous biomass: Catalyst performances in gasification of ethanol fermentation stillage with batch and flow reactors," *Chem. Eng. Sci.*, vol. 109, pp. 197–203, 2014.

[25] H. T. Nguyen, H. Lu, E. Kobayashi, T. Ishikawa, and M. Komiyama, "Raney-nickel catalyst deactivation in supercritical water gasification of ethanol fermentation stillage and its mitigation," *Top. Catal.*, vol. 57, no. 10–13, pp. 1078–1084, 2014.

[26] H. Kumar, P. Baredar, P. Agrawal, and S. C. Soni, "Effect of moisture content on

gasification efficiency in down draft gasifier," *Int. J. Sci. Eng. Technol.*, vol. 3, no. 4, pp. 411–413, 2014.

[27] J. Yanik, S. Ebale, A. Kruse, M. Saglam, and M. Yuksel, "Biomass gasification in supercritical water: Part 1. Effect of the nature of biomass," *Fuel*, vol. 86, no. 15, pp. 2410–2415, 2007.

[28] O. Yakaboylu, J. Harinck, K. G. Smit, and W. De Jong, "Supercritical Water Gasification of Biomass: A Literature and Technology Overview," pp. 859–894, 2015.

[29] C. He, C. L. Chen, A. Giannis, Y. Yang, and J. Y. Wang, "Hydrothermal gasification of sewage sludge and model compounds for renewable hydrogen production: A review," *Renew. Sustain. Energy Rev.*, vol. 39, pp. 1127–1142, 2014.

[30] N. Akiya and P. E. Savage, "Roles of water for chemical reactions in high-temperature water," *Chem. Rev.*, vol. 102, no. 8, pp. 2725–2750, 2002.

[31] O. Yakaboylu, J. Harinck, K. G. Gerton Smit, and W. De Jong, "Supercritical water gasification of manure: A thermodynamic equilibrium modeling approach," *Biomass and Bioenergy*, vol. XXX, pp. I–II, 2013.

[32] A. A. Peterson, F. Vogel, R. P. Lachance, M. Fröling, M. J. Antal, and J. W. Tester, "Thermochemical biofuel production in hydrothermal media: A review of sub- and supercritical water technologies," *Energy Environ. Sci.*, vol. 1, no. 1, pp. 32–65, 2008.

[33] J. Xu, J. Kou, L. Guo, H. Jin, Z. Peng, and C. Ren, "Experimental study on oil-containing wastewater gasification in supercritical water in a continuous system," *Int. J. Hydrogen Energy*, 2018.

[34] R. Lan, H. Jin, L. Guo, Z. Ge, S. Guo, and X. Zhang, "Hydrogen production by catalytic gasification of coal in supercritical water," *Energy and Fuels*, vol. 28, no. 11, pp. 6911–6917, 2014.

[35] S. Li, C. Zhu, S. Guo, and L. Guo, "A dispersed rutile-TiO2-supported Ni nanoparticle for enhanced gas production from catalytic hydrothermal gasification of glucose," *RSC Adv.*, vol. 5, no. 100, pp. 81905–81914, 2015.

[36] N. Boukis, U. Galla, H. Müller, and E. Dinjus, "Biomass gasification in supercritical water. Experimental progress achieved with the Verena pilot plant.," in *15th European Biomass Conference & Exhibition, 7-11 May 2007, Berlin, Germany*, 2007, no. May, pp. 1013–1016.

[37] P. de Jesús, N. Boukis, B. Kraushaar-Czarnetzki, and E. Dinjus, "Influence of process variables on gasification of corn silage in supercritical water," *Ind. Eng. Chem. Res.*, vol.

45, no. 5, pp. 1622–1630, 2006.

[38] C. Promdej and Y. Matsumura, "Temperature Effect on Hydrothermal Decomposition of Glucose in Sub- And Supercritical Water," *Ind. Eng. Chem. Res.*, no. 50, pp. 8492–8497, 2011.

[39] A. Kruse and E. Dinjus, "Hot compressed water as reaction medium and reactant. Properties and synthesis reactions," *J. Supercrit. Fluids*, vol. 39, no. 3, pp. 362–380, 2007.

[40] X. H. Hao, L. J. Guo, X. Mao, X. M. Zhang, and X. J. Chen, "Hydrogen production from glucose used as a model compound of biomass gasified in supercritical water," *Int. J. Hydrogen Energy*, vol. 28, no. 1, pp. 55–64, 2003.

[41] Y. Matsumura, X. X, and M. A. Jr, "Gasification characteristics of an activated carbon in supercritical water," *Carbon N. Y.*, vol. 35, no. 6, pp. 819–824, 1997.

[42] A. Kruse, D. Meier, P. Rimbrecht, and M. Schacht, "Gasification of pyrocatechol in supercritical water in the presence of potassium hydroxide," *Ind. Eng. Chem. Res.*, vol. 39, no. 12, pp. 4842–4848, 2000.

[43] W. Bühler, E. Dinjus, H. J. Ederer, A. Kruse, and C. Mas, "Ionic reactions and pyrolysis of glycerol as competing reaction pathways in near- and supercritical water," *J. Supercrit. Fluids*, vol. 22, pp. 437–53, 2001.

[44] A. Demirbas, "Biohydrogen generation from organic waste," *Energy Sources, Part A Recover. Util. Environ. Eff.*, vol. 30, no. 5, pp. 475–482, 2008.

[45] National Research Council (U.S.), *The Hydrogen Economy: Opportunities, Costs, Barriers, and R&D Needs*. 2101 Constitution Avenue, N.W. Box 285 Washington, DC 20055: National Acaedemy of Sciences, 2004.

[46] P. Azadi and R. Farnood, "Review of heterogeneous catalysts for sub- and supercritical water gasification of biomass and wastes," *Int. J. Hydrogen Energy*, vol. 36, no. 16, pp. 9529–9541, 2011.

[47] E. Afif, P. Azadi, and R. Farnood, "Catalytic hydrothermal gasification of activated sludge," *Appl. Catal. B Environ.*, vol. 105, no. 1–2, pp. 136–143, 2011.

[48] D. Yu, M. Aihara, and M. J. Antal, "Hydrogen Production by Steam Reforming Glucose in Supercritical Water," *Energy and Fuels*, vol. 7, no. 5, pp. 574–577, 1993.

[49] A. Kruse, T. Henningsen, A. Sinag, and J. Pfeiffer, "Biomass gasification in supercritical water: Influence of the dry matter content and the formation of phenols," *Ind. Eng. Chem. Res.*, vol. 42, pp. 3711–3717, 2003.

[50] Y. Matsumura *et al*., "Biomass gasification in near- and super-critical water: Status and prospects," *Biomass and Bioenergy*, vol. 29, no. 4, pp. 269–292, 2005.

[51] M. H. Waldner and F. Vogel, "Renewable production of methane from woody biomass by catalytic hydrothermal gasification," *Ind. Eng. Chem. Res.*, vol. 44, no. 13, pp. 4543–4551, 2005.

[52] Y. Lu, L. Guo, X. Zhang, and Q. Yan, "Thermodynamic modeling and analysis of biomass gasification for hydrogen production in supercritical water," *Chem. Eng. J.*, vol. 131, no. 1–3, pp. 233–244, 2006.

[53] L. J. Guo, Y. J. Lu, X. M. Zhang, C. M. Ji, Y. Guan, and A. X. Pei, "Hydrogen production by biomass gasification in supercritical water: A systematic experimental and analytical study," *Catal. Today*, vol. 129, no. 3–4, pp. 275–286, 2007.

[54] H. Tang and K. Kitagawa, "Supercritical water gasification of biomass: Thermodynamic analysis with direct Gibbs free energy minimization," *Chem. Eng. J.*, vol. 106, no. 3, pp. 261–267, 2005.

[55] I. G. Lee, M. S. Kim, and S. K. Ihm, "Gasification of glucose in supercritical water," *Ind. Eng. Chem. Res.*, vol. 41, no. 5, pp. 1182–1188, 2002.

[56] S. N. Reddy, S. Nanda, A. K. Dalai, and J. A. Kozinski, "Review of supercritical water gasification of biomass for hydrogen production," *Hydrog. Energy*, vol. 39, pp. 6912–6926, 2014.

[57] J. R. A. S. Andrea Kruse, "Influence of the Heating Rate and the Type of Catalyst on the Formation of Key Intermediates and on the Generation of Gases During Hydropyrolysis of Glucose in Supercritical Water in a Batch Reactor," *Ind. Eng. Chem. Res.*, vol. 43, no. 2, pp. 502–508, 2004.

[58] L. K. Mudge, S. L. Weber, D. H. Mitchell, L. J. Sealock, and R. J. Robertus, "Investigations on Catalyzed Steam Gasification of Biomass," 5285 Port Royal Road Springfield, Birginia 22151, 1981.

[59] L. J. Sealock, D. C. Elliott, E. G. Baker, A. G. Fassbender, and L. J. Silva, "Chemical processing in high-pressure aqueous environments. 5. New processing concepts," *Ind. Eng. Chem. Res.*, vol. 35, no. 11, pp. 4111–4118, 1996.

[60] M. P. Aznar, J. Corella, J. Delgado, and J. Lahoz, "Improved Steam Gasification of Lignocellulosic Residues in a Fluidized Bed with Commercial Steam Reforming Catalysts," *Ind. Eng. Chem. Res.*, vol. 32, no. 1, pp. 1–10, 1993.

[61] S. C. Gebhard, D. Wang, R. P. Overend, and M. A. Paisley, "Catalytic conditioning of

synthesis gas produced by biomass gasification," *Biomass and Bioenergy*, vol. 7, no. 1–6, pp. 307–313, 1994.

[62] D. N. Bangala, N. Abatzoglou, and E. Chornet, "Steam Reforming of Naphthalene on Ni-Cr/Al2O3 Catalysts Doped with MgO, TiO2, and La2O3," *AIChE J.*, vol. 44, no. 4, pp. 927–936, 1998.

[63] J. R. Rostrup-Nielsen and J. H. Bak Hansen, "Carbon dioxide reforming of methane over transition metals," *J. Catal.*, vol. 144, pp. 38–49, 1993.

[64] D. C. Elliott, T. R. Hart, and G. G. Neuenschwander, "Chemical processing in high-pressure aqueous environments. 8. Improved catalysts for hydrothermal gasification," *Ind. Eng. Chem. Res.*, vol. 45, no. 11, pp. 3776–3781, 2006.

[65] M. Osada, N. Hiyoshi, O. Sato, K. Arai, and M. Shirai, "Reaction pathway for catalytic gasification of lignin in presence of sulfur in supercritical water," *Energy and Fuels*, vol. 21, no. 4, pp. 1854–1858, 2007.

[66] M. Osada, A. Yamaguchi, N. Hiyoshi, O. Sato, and M. Shirai, "Regeneration of catalyst poisoned by sulfur in subcritical water.," *Energy and Fuels*, vol. 4, no. 22, pp. 845–849, 2008.

[67] P. T. Williams and J. Onwudili, "Composition of products from the supercritical water gasification of glucose: A model biomass compound," *Ind. Eng. Chem. Res.*, vol. 44, no. 23, pp. 8739–8749, 2005.

[68] O. Levenspiel, *Chemical reaction engineering*, 3rd ed. 605 Third Avenue, New York, NY: John Wiley & Sons, Inc., 1999.

[69] Christie J. Geankoplis, *Transport Processes and Unit Operations*, 3rd ed. Englewood Cliffs, New Jersey 07632: Prentice-Hall International, Inc., 1993.

[70] M. Peters and K. Timmerhaus, *Plant Design and Economics for Chemical Engineers*, Fourth Edi. McGraw-Hill, Inc., 1991.

[71] D. W. Green and R. H. Perry, *Perry's Chemical Engineers' Handbook*, 8th editio. United States of America: McGraw-Hill Companies, Inc., 2008.

[72] J. M. Smith, H. C. Van Ness, and M. M. Abbott, *Introduction to Chemical Engineering Thermodynamics*, 7th Editio. McGraw-Hill Companies, Inc.

[73] "Steadily Increasing the Production of Biodiesel Fuel from Waste Cooking Oil / Asia Biomass Energy Cooperation Promotion Office - Asia Biomass Office." [Online]. Available: https://www.asiabiomass.jp/english/topics/1107_02.html. [Accessed: 26-Dec-2018].

[74] A. B. Chhetri, K. C. Watts, and M. R. Islam, "Waste Cooking Oil as an Alternate Feedstock for Biodiesel Production," *Energies*, vol. 1, no. 1, pp. 3–18, 2008.

[75] S. Afandizadeh and E. A. Foumeny, "Design of packed bed reactors: Guides to catalyst shape, size, and loading selection," *Appl. Therm. Eng.*, vol. 21, no. 6, pp. 669–682, 2001.

[76] Castle Pumps, "Positive Displacement vs Centrifugal Pumps Guide – When to use which? | Castle Pumps." [Online]. Available: https://www.castlepumps.com/info-hub/positive-displacement-vs-centrifugal-pumps. [Accessed: 20-Jan-2019].

[77] Hydraulic Institute, "Positive Displacement pumps." [Online]. Available: http://pumps.org/Pump_Fundamentals/PD.aspx. [Accessed: 20-Jan-2019].

[78] V. Guarrasi, M. R. Mangione, V. Sanfratello, V. Martorana, and D. Bulone, "Quantification of underivatized fatty acids from vegetable oils by HPLC with UV detection," *J. Chromatogr. Sci.*, vol. 48, no. 8, pp. 663–668, 2010.

[79] S. Brunauer, P. H. Emmett, and E. Teller, "Adsorption of Gases in Multimolecular Layers," *J. Am. Chem. Soc.*, vol. 60, no. 2, pp. 309–319, 1938.

[80] "NOVAe Series® High-speed surface area and pore size analyzers."

[81] R. Mungroo, N. C. Pradhan, V. V. Goud, and A. K. Dalai, "Epoxidation of canola oil with hydrogen peroxide catalyzed by acidic ion exchange resin," *JAOCS, J. Am. Oil Chem. Soc.*, vol. 85, no. 9, pp. 887–896, 2008.

[82] D.W. de Leeuw, "Supercritical water gasification of sewage sludge, decomposition of lipids," 2015.

ANNEX

Summary of Experimental Results

Table A1. Tabulated data for gas yields and efficiencies.

Experiment Run	Parameter	Gasification Time (min)					
		30	60	120	180	240	300
SCWG 0.02	Gas Yield	123.6	110.7	100.8	92.5	86.4	87.4
	HGE	167.1	149.3	133.5	123.4	110.8	113.2
	CGE	80.8	72.3	63.8	56.9	49.2	52.4
SCWG 0.03	Gas Yield	81.5	78.6	75.0	74.1	81.8	77.0
	HGE	99.2	86.4	78.9	75.3	81.0	74.5
	CGE	64.3	58.5	55.6	53.3	57.0	52.4
SCWG 0.04	Gas Yield	60.6	63.5	57.8	56.2	35.9	35.0
	HGE	55.0	69.0	59.9	56.1	34.9	33.4
	CGE	33	46.5	42.0	39.6	24.4	23.3
SCWG 0.05	Gas Yield	40.9	19.4	25.7	29.6	30.6	27.0
	HGE	59.0	58.8	27.6	37.2	38.9	29.4
	CGE	34.0	33.9	20.9	23.1	22.9	20.5

* *Gas Yield (mol/kg oil), HGE and CGE (%)*

Table A2. Tabulated results for gas yields and efficiencies of SCWG 0.02.

Parameter	Component	Gasification Time (min)					
		30	60	120	180	240	300
Gas yield [mol/kg oil]	CO_2	31.0	27.8	25.9	22.7	20.0	22.2
	CH_4	19.7	17.3	13.8	12.3	10.1	9.8
	CO	1.4	1.6	0.0	0.0	1.6	1.9
	H_2	57.0	51.7	49.5	46.7	43.7	45.9
	unknown	14.5	12.4	11.6	10.9	11.0	7.8
HGE [%]		167.1	149.3	133.5	123.4	110.8	113.2
CGE [%]		80.8	72.3	63.8	56.9	49.2	52.4

Table A3. Tabulated results for gas yields and efficiencies of SCWG 0.03.

Parameter	Component	Gasification Time (min)					
		30	60	120	180	240	300
Gas yield [mol/kg oil]	CO_2	10.6	17.4	16.6	16.1	10.2	10.0
	CH_4	9.6	12.0	9.6	8.6	5.1	4.6
	CO	1.2	0.7	0.0	0.0	0.4	0.5
	H_2	12.4	15.9	15.4	15.3	10.0	10.1
	unknown	26.9	17.6	16.2	16.2	10.1	10.2
HGE [%]		55.0	69.0	59.9	56.1	34.9	33.4
CGE [%]		33.0	46.5	42.0	39.6	24.4	23.3

Table A4. Tabulated results for gas yields and efficiencies of SCWG 0.04.

Parameter	Component	Gasification Time (min)					
		30	60	120	180	240	300
Gas yield [mol/kg oil]	CO_2	23.1	22.3	22.4	22.2	24.3	22.9
	CH_4	17.7	14.5	12.2	11.1	11.3	9.8
	CO	0.6	0.9	0.0	0.0	1.1	1.1
	H_2	21.8	20.8	21.0	21.3	24.1	23.4
	unknown	18.2	20.1	19.3	19.6	21.0	20.3
HGE [%]		99.2	86.4	78.9	75.3	81.0	74.5
CGE [%]		64.3	58.5	55.6	53.3	57.0	52.4

Table A5. Tabulated results for gas yields and efficiencies of SCWG 0.05.

Parameter	Component	Gasification Time (min)					
		30	60	120	180	240	300
Gas yield [mol/kg oil]	CO_2	11.7	5.1	7.7	8.6	8.6	7.9
	CH_4	9.9	3.2	5.3	5.8	5.7	4.9
	CO	0.2	0.2	0.0	0.0	0.5	0.5
	H_2	14.1	0.5	5.3	9.8	11.1	7.2
	unknown	4.9	10.4	7.4	5.4	4.7	6.2
HGE [%]		59.0	58.8	27.6	37.2	38.9	29.4
CGE [%]		34.0	33.9	20.9	23.1	22.9	20.5

Table A6. Pore size distribution work table (Unspent catalyst).

1	2	3	4	5	6	7	8	9	10	11	12	13
P/P_o	Vgas STP $(cm^3\ g^{-1})$	Vliq $(cm^3\ g^{-1})$	Vliq $(cm^3\ mol^{-1})$	r_k x 10^8 (cm)	r_k (Å)	t (Å)	r_p (Å)	d_p (Å)	ΔVgas STP $(cm^3\ g^{-1})$	ΔVliq x 10^3 $(cm^3\ g^{-1})$	Δd_p (A)	$\Delta V_{liq}/\Delta d_p$ x 10^3
0.99	30.5	0.0472	1.32	364	36.4	19.1	55.5	111	1.75	2.71	78.7	0.034
0.89	28.8	0.0445	1.25	30.7	3.07	13.0	16.1	32.2	1	1.55	8.98	0.172
0.79	27.8	0.0429	1.20	1.43	1.43	10.1	11.6	23.2	1.25	1.93	4.41	0.439
0.69	26.5	0.0410	1.15	8.69	0.869	8.52	9.39	18.8	1.25	1.93	2.91	0.665
0.60	25.3	0.0391	1.09	5.85	0.585	7.35	7.94	15.9	1	1.55	2.15	0.719
0.50	24.3	0.0375	1.05	4.17	0.417	6.45	6.86	13.7	5.75	8.89	1.86	4.79
0.40	18.5	0.0286	0.80	2.42	0.242	5.69	5.93	11.9	1.75	2.71	1.48	1.83
0.30	16.8	0.0259	0.72	1.68	0.168	5.03	5.19	10.4	1.75	2.71	1.43	1.90
0.20	15.0	0.0232	0.65	1.12	0.112	4.37	4.48	8.96	1.875	2.90	1.44	2.02
0.10	13.1	0.0203	0.57	0.69	0.069	3.69	3.76	7.52				

Table A7. Pore size distribution work table (Blank catalyst).

1	2	3	4	5	6	7	8	9	10	11	12	13
P/Po	Vgas STP $(cm^3\ g^{-1})$	Vliq $(cm^3\ g^{-1})$	Vliq $(cm^3\ mol^{-1})$	r_k x 10^8 (cm)	r_k (Å)	t (Å)	r_p (Å)	d_p (Å)	ΔV_{gas} STP $(cm^3\ g^{-1})$	V_{liq} x 10^3 $(cm^3\ g^{-1})$	Δd_p (Å)	$\Delta V_{liq}/\Delta d_p$ x 10^3
0.98	50.8	0.0786	2.20	377	37.7	18.5	56.2	112	15.64	24.19	79.5	0.30
0.89	35.2	0.0544	1.52	36.2	3.62	12.9	16.5	32.9	6.68	10.33	9.68	1.07
0.79	28.5	0.0441	1.23	14.6	1.46	10.2	11.6	23.3	4.92	7.61	4.68	1.63
0.69	23.6	0.0364	1.02	7.73	0.773	8.52	9.29	18.6	3.56	5.51	3.05	1.81
0.59	20.0	0.0309	0.87	4.57	0.457	7.31	7.77	15.5	3.24	5.01	1.97	2.55
0.50	16.8	0.0259	0.73	2.93	0.293	6.50	6.79	13.6	4.36	6.74	1.99	3.39
0.39	12.4	0.0192	0.54	1.59	0.159	5.63	5.79	11.6	2.8	4.33	1.37	3.16
0.30	9.6	0.0148	0.42	9.55	0.096	5.01	5.11	10.2	3.8	5.88	1.50	3.93
0.19	5.8	0.0090	0.25	0.42	0.042	4.32	4.36	8.72	3.4	5.26	1.40	3.76
0.10	2.4	0.0037	0.10	0.12	0.012	3.65	3.66	7.32				

Table A8. Pore size distribution work table (SCWG 0.02_300min catalyst).

1	2	3	4	5	6	7	8	9	10	11	12	13
P/Po	Vgas STP $(cm^3\ g^{-1})$	Vliq $(cm^3\ g^{-1})$	Vliq $(cm^3\ mol^{-1})$	r_k x 10^8 (cm)	r_k (Å)	t (Å)	r_p (Å)	d_p (Å)	ΔV_{gas} STP $(cm^3\ g^{-1})$	V_{liq} x 10^3 $(cm^3\ g^{-1})$	Δd_p (Å)	$\Delta V_{liq}/\Delta d_p$ x 10^3
0.98	24.2	0.0374	1.049	165	16.5	18.3	34.9	69.7	10.25	16.0	41.3	0.38
0.89	14.0	0.0216	0.605	14.1	1.42	12.8	14.2	28.4	3.76	5.8	7.48	0.78
0.78	10.2	0.0158	0.442	4.98	0.498	9.98	10.5	21.0	1.5	2.3	3.51	0.66
0.69	8.7	0.0135	0.377	2.79	0.279	8.45	8.73	17.5	1.1	1.7	2.44	0.70
0.59	7.6	0.0118	0.329	1.75	0.175	7.33	7.50	15.0	1.2	1.9	1.95	0.95
0.49	6.4	0.0099	0.277	1.09	0.109	6.42	6.53	13.1	1.5	2.3	1.58	1.47
0.40	4.9	0.0076	0.212	0.64	0.064	5.67	5.74	11.5	0.9	1.4	1.52	0.91
0.29	4.0	0.0062	0.173	0.39	0.039	4.94	4.98	10.0	0.9	1.4	1.20	1.16
0.20	3.1	0.0048	0.134	0.23	0.023	4.35	4.38	8.8	0.9	1.4	1.34	1.04
0.10	2.2	0.0034	0.095	0.12	0.012	3.69	3.71	7.4				

Table A9. Pore size distribution work table (SCWG 0.03).

1	2	3	4	5	6	7	8	9	10	11	12	13
$P/_{Po}$	Vgas STP $(cm^3\ g^{-1})$	Vliq $(cm^3\ g^{-1})$	Vliq $(cm^3\ mol^{-1})$	r_k x 10^8 (cm)	r_k (Å)	t (Å)	r_p (Å)	d_p (Å)	ΔV_{gas} STP $(cm^3\ g^{-1})$	V_{liq} x 10^3 $(cm^3\ g^{-1})$	Δd_p (Å)	$\Delta V_{liq}/\Delta d_p$ x 10^3
0.98	20.6	0.0318	0.892	129	12.93	18.2	31.1	62.2	6.83	10.6	32.0	0.33
0.91	13.8	0.0213	0.596	16.6	1.664	13.5	15.1	30.3	4.08	6.31	7.39	0.85
0.82	9.68	0.0150	0.419	5.94	0.594	10.9	11.4	22.9	1.20	1.86	3.39	0.55
0.75	8.48	0.0131	0.367	3.55	0.355	9.40	9.75	19.5	0.72	1.11	2.59	0.43
0.67	7.76	0.0120	0.336	2.34	0.234	8.22	8.46	16.9	0.32	0.50	2.06	0.24
0.60	7.44	0.0115	0.322	1.67	0.167	7.26	7.43	14.9	0.40	0.62	1.92	0.32
0.59	7.04	0.0109	0.305	1.17	0.117	6.35	6.47	12.9	0.48	0.74	0.02	0.47
0.49	6.56	0.0101	0.284	1.09	0.109	6.35	6.46	12.9	1.20	1.86	1.46	1.27
0.40	5.36	0.0083	0.232	0.69	0.069	5.66	5.73	11.5	0.64	0.99	1.47	0.67
0.29	4.72	0.0073	0.205	0.46	0.046	4.95	5.00	9.99	0.69	1.06	1.29	0.82
0.19	4.03	0.0062	0.175	0.29	0.029	4.32	4.35	8.70				

Table A10. Pore size distribution work table (SCWG 0.04).

1	2	3	4	5	6	7	8	9	10	11	12	13
$P/_{Po}$	Vgas STP $(cm^3\ g^{-1})$	Vliq $(cm^3\ g^{-1})$	Vliq $(cm^3\ mol^{-1})$	r_k x 10^8 (cm)	r_k (Å)	t (Å)	r_p (Å)	d_p (Å)	ΔV_{gas} STP $(cm^3\ g^{-1})$	V_{liq} x 10^3 $(cm^3\ g^{-1})$	Δd_p (Å)	$\Delta V_{liq}/\Delta d_p$ x 10^3
0.99	17.4	0.0269	0.755	163	16.33	18.8	35.138	70.3	5.99	9.27	40.0	0.23
0.91	11.4	0.0177	0.495	14.7	1.465	13.7	15.162	30.3	4.86	7.51	7.31	1.03
0.83	6.57	0.0102	0.285	4.28	0.428	11.1	11.509	23.0	1.43	2.21	3.63	0.61
0.76	5.14	0.0080	0.223	2.20	0.220	9.48	9.695	19.4	0.74	1.15	2.65	0.43
0.67	4.40	0.0068	0.191	1.33	0.133	8.23	8.368	16.7	0.60	0.93	1.87	0.50
0.60	3.80	0.0059	0.165	8.77	0.088	7.34	7.432	14.9	0.66	1.02	1.92	0.53
0.49	3.14	0.0049	0.136	0.54	0.054	6.42	6.472	12.9	0.57	0.88	1.54	0.57
0.40	2.57	0.0040	0.111	0.33	0.033	5.67	5.702	11.4	0.69	1.06	1.40	0.76
0.30	1.89	0.0029	0.082	0.19	0.019	4.98	4.999	10.0	0.53	0.82	1.24	0.66
0.20	1.36	0.0021	0.059	0.10	0.010	4.37	4.379	8.76	0.57	0.88	1.46	0.61
0.10	0.79	0.0012	0.034	0.04	0.004	3.64	3.648	7.30				

Table A11. Pore size distribution work table (SCWG 0.05).

1	2	3	4	5	6	7	8	9	10	11	12	13
$P/_{Po}$	Vgas STP $(cm^3\ g^{-1})$	Vliq $(cm^3\ g^{-1})$	Vliq $(cm^3\ mol^{-1})$	r_k x 10^8 (cm)	r_k (Å)	t (Å)	r_p (Å)	d_p (Å)	ΔV_{gas} STP $(cm^3\ g^{-1})$	V_{liq} x 10^3 $(cm^3\ g^{-1})$	Δd_p (Å)	$\Delta V_{liq}/\Delta d_p$ x 10^3
0.99	31.1	0.0481	1.347	291	29.1	18.8	48.0	95.9	10.2	15.8	63.2	0.25
0.91	20.9	0.0323	0.905	26.8	2.68	13.7	16.4	32.8	7.01	10.8	8.78	1.23
0.83	13.9	0.0215	0.602	9.04	0.904	11.1	12.0	24.0	2.79	4.32	4.07	1.06
0.76	11.1	0.0172	0.481	4.74	0.474	9.48	9.95	19.9	2.06	3.19	2.88	1.11
0.67	9.03	0.0140	0.391	2.73	0.273	8.23	8.51	17.0	1.26	1.95	1.97	0.99
0.60	7.77	0.0120	0.337	1.79	0.179	7.34	7.52	15.0	1.64	2.53	2.00	1.26
0.49	6.14	0.0095	0.266	1.05	0.105	6.42	6.52	13.0	2.40	3.71	1.61	2.30
0.40	3.74	0.0058	0.162	0.49	0.048	5.67	5.72	11.4	1.14	1.76	1.42	1.24
0.30	2.61	0.0040	0.113	0.26	0.026	4.98	5.01	10.0	1.19	1.84	1.25	1.46
0.20	1.42	0.0022	0.062	0.11	0.011	4.37	4.38	8.76				

Table A12. Pore size distribution work table (SCWG 0.02_60min).

1	2	3	4	5	6	7	8	9	10	11	12	13
P/P_o	Vgas STP $(cm^3\ g^{-1})$	Vliq $(cm^3\ g^{-1})$	Vliq $(cm^3\ mol^{-1})$	r_k x 10^8 (cm)	r_k (Å)	t (Å)	r_p (Å)	d_p (Å)	ΔV_{gas} STP $(cm^3\ g^{-1})$	V_{liq} x 10^3 $(cm^3\ g^{-1})$	Δd_p (Å)	$\Delta V_{liq}/\Delta d_p$ x 10^3
0.99	20.3	0.0315	0.8813	214	21.44	19.0	40.4	80.8	6.30	9.74	50.4	0.19
0.91	14.0	0.0217	0.6085	17.0	1.699	13.5	15.2	30.4	5.18	8.02	7.76	1.03
0.82	8.86	0.0137	0.3840	5.31	0.531	10.8	11.3	22.6	1.44	2.22	3.31	0.67
0.75	7.43	0.0115	0.3218	3.05	0.305	9.33	9.64	19.3	1.13	1.75	2.53	0.69
0.67	6.30	0.0097	0.2728	1.87	0.187	8.19	8.37	16.7	0.73	1.12	1.86	0.61
0.59	5.57	0.0086	0.2413	1.27	0.127	7.32	7.44	14.9	0.73	1.12	1.96	0.57
0.49	4.84	0.0075	0.2098	0.82	0.081	6.38	6.47	12.9	0.97	1.50	1.56	0.96
0.39	3.87	0.0060	0.1679	0.50	0.050	5.64	5.69	11.4	0.73	0.11	1.41	0.80
0.29	3.15	0.0049	0.1364	0.31	0.031	4.95	4.98	9.96	0.57	0.87	1.25	0.70
0.20	2.58	0.0040	0.1119	0.19	0.019	4.34	4.36	8.72	0.65	9.99	1.49	0.67
0.09	1.94	0.0030	0.0839	0.10	0.010	3.60	3.61	7.23				

Table A13. Pore size distribution work table (SCWG 0.02_180min)

1	2	3	4	5	6	7	8	9	10	11	12	13
P/P_o	Vgas STP $(cm^3\ g^{-1})$	Vliq $(cm^3\ g^{-1})$	Vliq $(cm^3\ mol^{-1})$	r_k x 10^8 (cm)	r_k (Å)	t (Å)	r_p (Å)	d_p (Å)	ΔV_{gas} STP $(cm^3\ g^{-1})$	V_{liq} x 10^3 $(cm^3\ g^{-1})$	Δd_p (Å)	$\Delta V_{liq}/\Delta d_p$ x 10^3
0.98	29.6	0.0457	1.2804	233	23.27	18.6	41.8	83.7	13.2	20.4	53.2	0.38
0.90	16.4	0.0253	0.7085	19.0	1.897	13.3	15.2	30.4	5.49	8.49	7.05	1.20
0.83	10.9	0.0168	0.4706	6.93	0.693	11.0	11.7	23.4	2.22	3.43	4.01	0.86
0.75	8.64	0.0134	0.3745	3.55	0.355	9.33	9.69	19.4	0.93	1.45	1.48	0.98
0.71	7.71	0.0119	0.3340	2.65	0.265	8.69	8.95	17.9	0.70	1.08	2.70	0.40
0.60	7.01	0.0108	0.3036	1.66	0.166	7.43	7.60	15.2	0.23	0.36	0.19	1.87
0.60	6.77	0.0105	0.2935	1.57	0.157	7.35	7.50	15.0	0.93	1.45	2.11	0.69
0.49	5.84	0.0090	0.2530	0.97	0.097	6.35	6.45	12.9	1.40	2.17	1.64	1.32
0.38	4.44	0.0069	0.1923	0.56	0.055	5.57	5.63	11.3	0.82	1.26	1.34	0.95
0.29	3.62	0.0056	0.1569	0.35	0.035	4.93	4.96	9.92	0.82	1.26	1.29	0.98
0.19	2.80	0.0043	0.1214	0.20	0.020	4.30	4.32	8.63	0.82	1.26	1.40	0.90
0.09	1.99	0.0031	0.0860	0.01	0.010	3.60	3.61	7.23				